SEISMIC PERFORMANCE QUANTIFICATION OF REINFORCED CONCRETE SHEAR WALLS WITH DIFFERENT END CONFIGURATIONS: EXPERIMENTAL ASSESSMENT AND DATA-DRIVEN PERFORMANCE MODELS

SEISMIC PERFORMANCE QUANTIFICATION OF REINFORCED CONCRETE SHEAR WALLS WITH DIFFERENT END CONFIGURATIONS: EXPERIMENTAL ASSESSMENT AND DATA-DRIVEN PERFORMANCE MODELS

By
Omar Ali El-Azizy
P. Eng.,

A Thesis Submitted to the School of Graduate Studies in Partial Fulfillment of the Requirements for the Degree Doctor of Philosophy

McMaster University
© Copyright by Omar El-Azizy

December 2022

Doctor of Philosophy (2022) (Civil Engineering)	McMaster University Hamilton, Ontario
TITLE:	Seismic performance quantification of reinforced concrete shear walls with different end configurations: experimental assessment and data-driven performance models
AUTHOR:	Omar El-Azizy B. Eng. (McMaster University), P. Eng.
SUPERVISOR:	Dr. Mohamed Ezzeldin
NUMBER OF PAGES:	xvi, 201

Abstract

Well-detailed reinforced concrete *(RC)* shear walls did not achieve the expected seismic performance in the 2011 Christchurch earthquake as per the Canterbury earthquake royal commission report. Similarly, *RC* shear walls showed low seismic performance in the 2010 Maule earthquake. The two major seismic events intrigued this research dissertation, where six half-scaled *RC* shear walls were constructed and tested. The six walls were split into two phases, each phase had different end configurations (i.e., rectangular, flanged, and boundary elements). *Phase II RC* walls had *2.4* times the vertical reinforcement ratio of *Phase I* walls. The walls were detailed as per CSA A23.3-19, and they were tested laterally under a quasi-static cyclic fully-reversed loading while maintaining a constant axial load through the full test of the walls.

The overall seismic performance of the six walls is evaluated in Chapters 2 and 3 in terms of their load-displacement relationships, crack patterns, displacement ductility capacities, stiffness degradation trends, curvature profiles, end strains, energy dissipation capabilities, and equivalent viscous damping ratios. In addition, damage states are specified according to the Federal Emergency Management Assessment (FEMA P58) guidelines. The results came in agreement with the Canterbury earthquake royal commission report, where the test walls with low vertical reinforcement ratios showed lower-than-expected seismic performance due to the concentration of their plastic hinges at the primary crack locations. Moreover, the results validated the Christchurch (2011) and Maule (2010) earthquake findings as concentrating the rebars at the end zones and providing adequate confinement enhanced the seismic performance of the test walls, which was the case for *Phase II* flanged and boundary element walls.

The displacement ductility variations of the test walls inspired the work of Chapter 4, where the objective is to develop a data-driven expression for *RC* shear walls to better quantify their displacement ductility capacities. In this respect, an analytical model is developed and experimentally validated using several *RC* walls. The analytical model is then used to generate a dataset of *RC* walls with a wide range of geometrical configurations and design parameters, including cross-sectional properties, aspect ratios, axial loads, vertical reinforcement ratio, and concrete compressive strengths. This dataset is utilized to develop two data-driven prediction expressions for the displacement ductility of *RC* walls with rectangular and flanged/boundary element end configurations. The developed data-driven expressions accurately predicted the displacement ductility of such walls and they should be adopted by relevant building codes and design standards, instead of assigning a single ductility-related modification factor for all ductile *RC* shear walls, as per the 2020 National Building Code of Canada.

Several researchers tested well-detailed Reinforced Masonry (*RM*) shear walls and the results concluded that *RM* shear walls showed high seismic performance similar to that of *RC* shear walls. This intrigued the research efforts presented in Chapter 5, where a comparative analysis is performed between the six *RC* walls tested in this dissertation and three *RM* walls tested in a previous experimental program. The analysis focuses on comparing the seismic performance of both wall systems in terms of their crack patterns, load-displacement envelopes, curvature profiles, displacement ductility, normalized periods, and equivalent viscous damping ratios. In addition, an economic assessment is

performed to compare such *RC* and *RM* shear walls using their total rebar weights and the total construction costs. Overall, *RM* shear walls achieved an acceptable seismic performance coupled with low rebar weights and low construction costs when compared to their *RC* counterparts.

DEDICATIONS

To
Ali & Ragia,
Sara & Zein,
and
The loving memory of my grandmother

ACKNOWLEDGMENTS

I would like to sincerely thank my supervisor Dr. Mohamed Ezzeldin and my former supervisor Dr. Wael El-Dakhakhni. It was a great pleasure working with you, your help is greatly appreciated. I would also like to thank Dr. Marwan Shedid, for his support and help in Chapter 2. In addition, I would like to thank my current supervisory committee members, Dr. Wael El-Dakhakhni, Dr. Sumanth Shankar, and Dr. Peijun Guo, for all the support and help in my doctoral dissertation.

The experimental work would not be possible without the help of Mostafa El-Sayed, Mustafa Siyam, Ahmed Ashour, Mark Hayman, Bennett Banting, and Yasser Khalifa. The experimental program was completed because of their great help. Sincere thanks to the great Applied Dynamics Laboratory technicians, Kent Wheeler and Paul Heerema. Their ideas and laboratory experience were of great help in the experimental work done.

I would like to acknowledge my research funding support National Science and Engineering Research Council (NSERC) of Canada and the McMaster Centre for Effective Design of Structures (CEDS) funded through the Ontario Research and Development Challenge Fund (ORDCF) of the Ministry of Research and Innovations.

Finally, no words can describe the support of my family, I would like to sincerely, thank my Parents, Ali and Ragia for all the support that was provided over the years. I would like to thank my wife, Sara, for her patience, and support and for taking care of our newborn son, Zein. Moreover, I would like to thank my siblings, Mohamed and Rana, for their support and encouragement to finish my doctorate. Finally, I would like to dedicate the doctorate dissertation to the loving memory of my grandmother who really encouraged me to get my doctorate and really wished to see me finish it.

Co-Authorship

This thesis has been prepared in accordance with the regulations for a sandwich thesis format or as a compilation of research papers stipulated by the Faculty of Graduate Studies at McMaster University. This thesis presents research and analytical work carried out solely by Omar El-Azizy. Advice and guidance were provided for the whole thesis by the academic supervisor Dr. Mohamed Ezzeldin. Dr. Marwan Shedid and my former academic supervisors, Dr. Wael El-Dakhakhni and Dr. Robert Drysdale, provided comments and edits as indicated by the co-authorship of the chapters below. Information presented from outside sources, which has been used for analysis or discussion, has been cited where appropriate; all other materials are the sole work of the author. This thesis consists of the following manuscripts in the following chapters:

Chapter 2

El-Azizy, O. A., Shedid, M. T., El-Dakhakhni, W. W., & Drysdale, R. G. (2015). Experimental evaluation of the seismic performance of reinforced concrete structural walls with different end configurations. *Engineering Structures*, *101*, 246-263.

Chapter 3

El-Azizy, O. A., Ezzeldin M., & El-Dakhakhni, W. (2022). Analysis of reinforced concrete Shear walls with different configurations for seismic design. *J. Struct. Eng.,* (Accepted)

Chapter 4

El-Azizy, O. A., Ezzeldin M., & El-Dakhakhni, W. (2022). Data-driven displacement ductility expressions for reinforced concrete shear walls with different configurations. *J. Struct. Eng.,* (Submitted—STENG-12057)

Chapter 5

El-Azizy, O. A., Ezzeldin M., & El-Dakhakhni, W. (2022). Comparative analysis of reinforced masonry and reinforced concrete shear walls with different end configurations: seismic performance and economic assessment. *J. Struct. Eng.,* (Submitted—STENG-12256)

Table of Content

List of Tables

List of Figures

CHAPTER 1
INTRODUCTION

1.1 BACKGROUND AND MOTIVATION

In 2011, the Christchurch earthquake resulted in major damage to reinforced concrete (*RC*) buildings. The Canterbury earthquake royal commission report (2011), observed that well-detailed *RC* shear walls did not show the expected seismic performance. Although such walls were designed according to the New Zealand Standards NZS 3101-06 (NZS 2006), they did not achieve the expected ductility capabilities. The report demonstrated that this poor performance of the walls was mainly due to the concentration of the plastic hinges at the initial primary cracks. Such cracks increased in size as the lateral displacement of the walls increased, resulting in a concentration of inelastic strains and then premature failures at much lower displacement ductility levels than originally designed. The primary cracks and plastic strain concentrations also limited the energy dissipation capacity of the walls. The Canterbury earthquake royal commission report (2011) concluded that the low ductile capability of the walls was mainly due to their insufficient vertical reinforcement ratios. The report recommended also increasing the vertical reinforcement ratio and concentrating the vertical reinforcement at the wall end regions. This is expected to initiate secondary cracks, distribute the plastic strains over multiple cracks, and increase the plastic hinge length, thus resulting in reduced curvature ductility demands at the primary crack locations. With such recommendations, *RC* walls can show better seismic performance in terms of higher ultimate displacements, high ductile levels, and enhanced energy dissipation capabilities.

In another seismic event, the 2010 Maule Chile Earthquake, several *RC* shear walls showed low seismic performance due to their: i) high axial loads and high out-of-plane slenderness ratios (Jünemann et al. 2012); and ii) poor detailing and confinement requirements (Carpenter et al. 2010; Wallace et al. 2012). The strength of such *RC* shear walls degraded dramatically at low displacement levels due to concrete crushing followed by a buckling of the vertical reinforcement. Most of the damaged walls were also too thin to be adequately confined at their end zones.

The two seismic events intrigued this research project, where the CSA A23.3-19 (CSA 2019) has similar detailing requirements as the NZS 3101-06 (NZS 2006). Therefore, the dissertation focuses on presenting the experimental results of six half-scale *RC* walls detailed as ductile shear walls following the requirements of CSA A23.3-19 (CSA 2019). All the walls are tested under a quasi-static cyclic fully-reversed loading to represent seismic loading demands. Since the royal commission report of the Canterbury earthquake (2011) recommended increasing the vertical reinforcement ratios, a comparative analysis between two sets of walls (*Phase I* & *Phase II*) with different vertical reinforcement ratios is presented in Chapters 2 and 3. In addition, due to the findings of the Maule earthquake (2010) and the Canterbury commission report (2011), the concentration of rebars at the end zones is considered through different configurations (flanged and boundary elements) to facilitate direct comparison with their respective rectangular walls.

The National Building Code of Canada (NBCC 2020) provides a single ductility-related modification factor, R_d, which is 3.5. This single value is to be used in the design of all ductile *RC* shear walls regardless of the various design parameters. Therefore, there

was a need for a simple methodology that accurately predicts the seismic performance of *RC* shear walls based on their geometrical configurations and design parameters (i.e., cross-sectional properties, aspect ratios, reinforcement ratios, axial loads, and concrete compressive strengths). In this respect, the dissertation in Chapter 4 proposes data-driven expressions to accurately evaluate the displacement ductility of *RC* shear walls based on the various configurations and parameters. The data-driven expressions are verified against experimentally tested walls by other researchers (Oesterle et al. 1979; Esaki 1994; Tran and Wallace 2012) using their reported displacement ductility values.

Many researchers (e.g., Zhang et al. 2000; Massone and Wallace, 2004; Thomsen and Wallace 2004; Adebar et al. 2007; Ghorbanirenani et al. 2012; Luu et al. 2014; Christidis and Trezos 2017; Rong et al. 2020; Gondia et al. 2020; Akl and Ezzeldin 2023) have conducted studies on *RC* shear walls to evaluate their seismic performance by analyzing the crack patterns, plastic hinge lengths, curvatures, strains, energy dissipation capacities, equivalent viscous damping ratios, stiffness degradation trends, and ductility levels. These studies considered a wide range of walls with different design parameters. The results demonstrated that the seismic performance of *RC* shear walls is heavily dependent on several key design parameters (e.g., vertical reinforcement ratio, axial load, thickness). Similarly, several researchers (Eikanas 2003; Shedid et al. 2008; Shedid et al. 2010; Haach et al. 2010; Banting et al. 2012; Ahmadi et al. 2014; El Ezz et al. 2015; Siyam et al. 2016; Ezzeldin et al. 2017) have performed tests on reinforced masonry (*RM*) to investigate their seismic performance through a wide range of design parameters. The results showed that *RM* shear walls can show an adequate seismic performance if the walls

are well-detailed including the use of confinement at their ends. Therefore, Chapter 5 of the dissertation presents a comparative analysis between *RC* and *RM* shear walls, where the *RC* walls presented in Chapters 2, 3, and 4 have identical dimensions and axial loads as the *RM* walls tested by Shedid et al. (2010). Specifically, *Phase I RC* shear walls are designed to have similar lateral strengths as their respective *RM* shear walls, while *Phase II RC* shear walls have similar ultimate curvature values as their *RM* counterparts at the wall-foundation interface to allow for direct comparison between the walls. Chapter 5 includes also an economic assessment to compare *RC* and *RM* walls in terms of their total rebar weights and total construction costs (Abouyoussef and Ezzeldin 2023; Barbachyn et al. 2017).

1.2 RESEARCH OBJECTIVES

The main objective of this dissertation is to enhance the design of *RC* shear walls against major seismic events. Therefore, the following sub-objectives were defined to achieve the objective of the dissertation:

1. Validate experimentally the key design parameters behind the low seismic performance *RC* shear walls observed in the two major earthquake events of Christchurch (2011) and Maule (2010).
2. Quantify the seismic performance of *RC* walls with a wide range of design parameters, including the vertical reinforcement ratios and the end configurations (i.e., rectangular, flanged, and boundary element walls).

3. Create an analytical model to develop data-driven expressions that can accurately predict the displacement ductility values of rectangular and flanged/boundary element *RC* shear walls.
4. Perform a detailed comparative analysis of the seismic performance of *RC* shear walls compared to *RM* shear walls.

1.3 ORGANIZATION OF THE DISSERTATION

This dissertation consists of six chapters:

- **Chapter 1** presents the motivation and objectives of the dissertation as well as background information about the research program.
- **Chapter 2** focuses on presenting the experimental program details including the wall configurations, test setup, loading protocol, and instrumentations. The crack patterns, failure modes, load-displacement envelopes, and stiffness degradation trends of the six walls are presented. Wall damage quantification is also presented according to the Federal Emergency Management Agency (FEMA P58) methodology that relates the damage state to the residual story drifts. Finally, displacement ductility values are computed and presented.
- **Chapter 3** performs a comparative analysis between the tested *RC* shear walls to present several performance-based design parameters. The end-strains (compressive and tensile), yield and ultimate curvatures, curvature profiles, extents of plasticity, reinforcement strains, energy dissipation capabilities, and equivalent viscous damping ratios of all the walls are quantified and presented.

- **Chapter 4** develops and validates an analytical model using Response 2000 software (Bentz and Collins 2000) to capture the nonlinear behavior of *RC* shear walls. The model is then used to generate a dataset for *RC* shear walls with different displacement ductility values using a wide range of design parameters. The training dataset is then combined via Design Expert statistical software V13 (2020), through an inverse linear regression technique, in order to introduce and validate two data-driven expressions (for rectangular and flanged/boundary element walls). Afterward, the interpretability of the data-driven expressions is assessed by comparing their predictions relative to the known mechanics of *RC* shear walls.
- **Chapter 5** compares the seismic performance between the six *RC* walls and the three *RM* shear walls tested by Shedid et al. (2010). The comparison between the walls is presented in terms of the crack patterns, load-displacement envelopes, curvature profiles, ductility capacities, normalized periods, and equivalent viscous damping ratios. Afterward, an economic assessment is performed to compare the walls using their total rebar weights and total construction costs.
- **Chapter 6** presents the dissertation summary, main conclusions, and recommendations for future research studies.

It is worth noting that although each chapter presents a standalone journal manuscript, Chapters 2, 3, 4, and 5 collectively describe a cohesive research program as outlined in this chapter of the dissertation. Nonetheless, for completeness of the individual standalone chapters/manuscripts, some overlap might exist including the geometrical configurations and design parameters of the walls.

1.4 REFERENCES

Abouyoussef, M., & Ezzeldin, M. (2023) Fragility and Economic Evaluations of High-Strength Reinforced Concrete Shear Walls in Nuclear Power Plants. *Journal of Structural Engineering*, https://doi.org/10.1061/JSENDH/STENG-11397.

Adebar, P., Ibrahim, A. M., & Bryson, M. (2007). Test of high-rise core wall: effective stiffness for seismic analysis. *ACI Structural Journal*, *104*(5), 549.

Ahmadi, F., Hernandez, J., Sherman, J., Kapoi, C., Klingner, R. E., & McLean, D. I. (2014). Seismic performance of cantilever-reinforced concrete masonry shear walls. *Journal of Structural Engineering*, *140*(9), 04014051.

Akl, A., & Ezzeldin, M. (2023). Seismic collapse risk assessment of low-aspect-ratio reinforced concrete shear walls using the FEMA P695 methodology. *Journal of Structural Engineering*, http://10.1061/(ASCE)ST.1943-541X.0003505.

Banting, B. R., & El-Dakhakhni, W. W. (2012). Force-and displacement-based seismic performance parameters for reinforced masonry structural walls with boundary elements. *Journal of Structural Engineering*, *138*(12), 1477-1491.

Barbachyn, S. M., Devine, R. D., Thrall, A. P., & Kurama, Y. C. (2017). Economic evaluation of high-strength materials in stocky reinforced concrete shear walls. *Journal of Construction Engineering and Management*, *143*(10), 04017074.

Bentz, E. C., & Collins, P. (2000). Response 2000, Reinforced Concrete Section Analysis using the Modified Compression Theory. *Toronto, University of Toronto*.

Canadian Standards Association (CSA). (2019). *Design of concrete structures*. CSA A23.3-19, CSA, Mississauga, Canada.

Canterbury Earthquake Royal Commission report. (2011). *Seismic performance Christchurch building under the Canterbury Earthquake.* Retrieved Nov. 19th, 2019, http://canterbury.royalcommission.govt.nz/Final-Report-Volume-One-Contents

Carpenter, L. D., Naeim, F., Lew, M., Youssef, N. F., Rojas, F., Saragoni, G. R., & Adaros, M. S. (2011). Performance of tall buildings in Viña del Mar in the 27 February 2010 offshore Maule, Chile earthquake. *The Structural Design of Tall and Special Buildings*, *20*(1), 17-36.

Christidis, K. I., & Trezos, K. G. (2017). Experimental investigation of existing non-conforming RC shear walls. *Engineering Structures*, *140*, 26-38.

Eikanas, I. K. (2003). Behavior of concrete masonry shear walls with varying aspect ratio and flexural reinforcement MS Thesis, Department of Civil and Environmental Engineering. *Pullman, WA: Washington State University*.

El Ezz, A. A., Seif Eldin, H. M., & Galal, K. (2015). Influence of confinement reinforcement on the compression stress–strain of grouted reinforced concrete block masonry boundary elements. *Structures*, 2, 32-43, Elsevier.

Ezzeldin, M., El-Dakhakhni, W., & Wiebe, L. (2017). Experimental assessment of the system-level seismic performance of an asymmetrical reinforced concrete block–wall building with boundary elements. *Journal of Structural Engineering*, 143(8), 04017063.

Federal Emergency Management Agency (FEMA P58) (2012). *Seismic Performance Assessment of Buildings: Damage states for residual story drifts.* Federal Emergency Management Agency (FEMA) 356, Washington D.C., USA.

Ghorbanirenani, I., Tremblay, R., Léger, P., & Leclerc, M. (2012). Shake table testing of slender RC shear walls subjected to eastern North America seismic ground motions. *Journal of Structural Engineering*, *138*(12), 1515-1529.

Gondia, A., Ezzeldin, M., & El-Dakhakhni, W. (2020). Mechanics-guided genetic programming expression for shear-strength prediction of squat reinforced concrete walls with boundary elements. *Journal of Structural Engineering*, *146*(11), 04020223.

Haach, V. G., Vasconcelos, G., & Lourenço, P. B. (2010). Experimental analysis of reinforced concrete block masonry walls subjected to in-plane cyclic loading.

Jünemann, R., Hube, M., De La Llera, J. C., & Kausel, E. (2012, September). Characteristics of reinforced concrete shear wall buildings damaged during 2010 Chile earthquake. In *Proceedings of the 15th World Conference of Earthquake Engineering*.

Luu, H., Léger, P., & Tremblay, R. (2014). Seismic demand of moderately ductile reinforced concrete shear walls subjected to high-frequency ground motions. *Canadian journal of civil engineering*, *41*(2), 125-135.

Massone, L. M., & Wallace, J. W. (2004). Load-deformation responses of slender reinforced concrete walls. *Structural Journal*, *101*(1), 103-113.

NBCC (2020): National Research Council of Canada (2020). *National Building Code of Canada.*

Oesterle, R. G., Aristizabal-Ochoa, J. D., Fiorato, A. E., Russell, H. G., & Corley, W. G. (1979). Earthquake resistant structural walls-tests of isolated walls-phase II. *Construction Technology Laboratories*, Portland Cement Association.

Rong, X. L., Zheng, S. S., Zhang, Y. X., Zhang, X. Y., & Dong, L. G. (2020). Experimental study on the seismic behavior of RC shear walls after freeze-thaw damage. *Engineering Structures*, *206*, 110101.

State-Ease. *Design Expert Software Version 13 User Guide.* Stat-Ease, Inc., Minneapolis, USA, 2020.

Shedid, M. T., Drysdale, R. G., & El-Dakhakhni, W. W. (2008). Behavior of fully grouted reinforced concrete masonry shear walls failing in flexure: Experimental results. *Journal of structural engineering*, *134*(11), 1754-1767.

Shedid, M. T., El-Dakhakhni, W. W., & Drysdale, R. G. (2010). Alternative strategies to enhance the seismic performance of reinforced concrete-block shear wall systems. *Journal of structural engineering*, *136*(6), 676-689

Siyam, M. A., El-Dakhakhni, W. W., Shedid, M. T., & Drysdale, R. G. (2016). Seismic response evaluation of ductile reinforced concrete block structural walls. I: Experimental results and force-based design parameters. *Journal of Performance of Constructed Facilities*, *30*(4), 04015066.

Standards New Zealand (NZS). (2006). *Concrete Structures Standard.* NZS 3101, NZS, Wellington, New Zealand.

Thomsen IV, J. H., & Wallace, J. W. (1995). *Displacement-based design of RC structural walls: experimental studies of walls with rectangular and T-shaped cross sections* (Vol. 6). Report No. CU/CEE-95.

Thomsen IV, J. H., & Wallace, J. W. (2004). Displacement-based design of slender reinforced concrete structural walls—experimental verification. *Journal of structural engineering*, *130*(4), 618-630.

Tran, T. A., & Wallace, J. W. (2012). Experimental Study of the Lateral Load Response of Moderate Aspect Ratio Reinforced Concrete Structural Walls. *Report No. UCLA-SGEL 2012*, *12*.

Wallace, J. W., Massone, L. M., Bonelli, P., Dragovich, J., Lagos, R., Lüders, C., & Moehle, J. (2012). Damage and implications for seismic design of RC structural wall buildings. *Earthquake Spectra*, *28*(1_suppl1), 281-299.

Zhang, Y., & Wang, Z. (2000). Seismic behavior of reinforced concrete shear walls subjected to high axial loading. *Structural Journal*, 97(5), 739-750.

CHAPTER 2
EXPERIMENTAL EVALUATION OF THE SEISMIC PERFORMANCE OF REINFORCED CONCRETE STRUCTURAL WALLS WITH DIFFERENT END CONFIGURATIONS

2.1 ABSTRACT

The Canterbury Earthquake Royal Commission report (2011) showed that cantilever reinforced concrete (*RC*) walls failed at a lower ductility capacity than expected due to a plasticity concentration region within a very limited height near the location of the primary cracks at the base of the walls. The New Zealand Standards *(NZS 3101)* (2006) and the Canadian design standards *(CSA A23.3-14)* (2014), adopt the same capacity design approaches for *RC* walls design, with both standards specifying a minimum vertical reinforcement ratio $(\rho_v\%)$ of *0.25%* for *RC* walls. Subsequently, the current study was conducted to study the seismic performance of reinforced concrete walls with different vertical reinforcement ratios and cross-sectional configurations. In this paper, six half-scaled reinforced concrete structural walls were constructed and tested under quasi-static displacement controlled cyclic loading. The walls had three different cross-sectional configurations (i.e., rectangular, flanged, and boundary elements) and they were tested with specific design characteristics that were selected to evaluate and compare the wall ductility capabilities. In this respect, wall ductility can be defined as the ability of the walls to undergo inelastic deformations with no/low strength degradation, which is essential in Seismic Force Resisting Systems *(SFRS)* as it is not feasible to design structures to behave elastically against seismic loadings. So the ductility quantification of the structural walls used was the ductility ratio between the intended displacements with the yield

displacement. Based on the test results, the ultimate drift at *20%* ultimate strength degradation varied between *0.9* to *1.6%* and the ultimate level displacement ductility ($\mu_{\Delta 0.8u}$), ranged approximately between *4.0* and *6.0*. Although the flanged walls and the walls with boundary elements were designed to develop almost the same capacity as that of the rectangular walls, the seismic performance of the former wall type was found to be superior to that of their rectangular counterparts with respect to both the ultimate displacement capacity and ductility level. Moreover, using the flanges and the boundary elements walls resulted in approximately *30%* reduction of the vertical reinforcement compared to that of the rectangular walls when designed to resist the same lateral loads while carrying identical gravity loads. In addition to gaining insights on the response of walls with boundary elements, the results indicated that structural walls with low vertical reinforcement ratios can experience reduced ductility as indicated in the Canterbury Commission Report.

2.2 INTRODUCTION

The Canterbury Earthquake Royal Commission report (2011) revealed that some reinforced concrete walls that are designed according to the New Zealand Standards (NZS 3101) (2006) and detailed to comprise the seismic force-resisting system of buildings, did not achieve their expected ductile capability. The report indicated that the reason was the formation of a primary flexural crack at the expected plastic hinge areas. Such crack would then keep increasing in size as the wall top displacements increase and consequently concentrating the steel plastic strain over a relatively very short height resulting in a

premature wall failure at a much lower ductility level compared to what is expected. Such cracking patterns would result in strain concentration of the plastic hinge at a limited zone as well as limiting the generated energy dissipation during seismic events. The report showed that such less-than-expected ductile behavior was associated with insufficient vertical reinforcement that would have resulted in secondary cracks and higher energy dissipation. Consequently yielding of the reinforcement was limited to the immediate vicinity of that single primary crack (Canterbury Commission Report, 2011). Subsequently, the report concluded with a recommendation to concentrate the vertical reinforcement ratio ρ_v, at the wall end regions to allow for the formation of secondary cracks and to enhance the energy dissipation capabilities by spreading the inelastic straining over a larger length of the outermost wall bars. Such detailing would then increase the wall plastic hinge height and hence, reduce the curvature ductility demands corresponding to different displacement ductility levels.

In addition, observations following the Maule earthquake in Chile (2010), indicated that structural walls showed deficient performance attributed to a combination of high axial loads and high out-of-plane slenderness ratios (small thickness) of the walls (Jünemann et al. 2012). While Wallace et al. (2012), concluded that the unexpected seismic performance in Maule Earthquake was due to the poor web boundary detailing where the strength degraded dramatically because of the buckling of the vertical reinforced after concrete crushing. Similarly, Carpenter et al. (2010) concluded that the reason for the low ductile capacities of the structural walls in the Maule Earthquake was poor detailing and confinement. Most of the damaged walls were too thin to be confined which was

considered another reason for the poor seismic performance of the structural walls in the Maule Earthquake. Within the context of the current study, it might be argued that the small thickness of the walls reported herein was the common parameter between them and those that experienced low seismic performance during the Maule earthquake in Chile (2010).

Thomsen and Wallace (1995) tested rectangular and t-shaped structural walls to examine the importance of confinement and transverse reinforcement spacing on the seismic performance of walls. It was concluded that the small spacing of the transverse hoops could enhance the ductility of the structural walls. While Thomsen and Wallace (2004) used the tested walls to analytically predict the strain profiles where the assumption of the plastic hinge $0.33l_w$ and $0.5l_w$ had a significant impact on the predicted results. Massone and Wallace (2004) used the tested walls to assess the wall flexure and shear displacement contributions to the inelastic displacement. The study found that diagonally placed displacement transducers overestimate shear by up to *30%* and that there is a strong coupling between inelastic flexural and inelastic shear deformations. Zhang et al. (2000) evaluated the seismic behavior of rectangular walls under high axial loading and then concluded the negative effect of high axial loading on the ductility of the walls. Adebar et al. (2007) tested one *RC* core wall with a high axial load and low vertical reinforcement ratio, in order to investigate the effect of cracking on the walls' effective stiffness. Concluded that although there was a large flexure and shear diagonal cracking in the wall, the effective stiffness of the cracked wall was similar to the uncracked wall due to the axial load. Sittipunt et al. (2001) tested a series of *RC* walls to investigate the effect of diagonal web reinforcement on the hysteretic curves. They concluded that the diagonal web

reinforcement enhanced the walls' energy dissipation and minimized the pinching effect on the hysteretic curves. White (2004) developed procedures to estimate the inelastic rotational demand of concrete walls, coupling beam chord rotation, and the walls' performance with axial yielding. They concluded that for higher period walls the axial demand of coupled walls decreased and walls allowed to yield in axial tension showed lower coupling beam rotations and energy dissipation capacities.

Beyer et al. (2008), tested two U-Shaped structural walls in order to evaluate their flexural behavior in different directions. They concluded that the diagonal direction was the most critical direction where the displacement capacity was the smallest. Preti and Giuriani (2011), tested a full-scale *RC* wall reinforced with unusual large rebar diameters, uniformly distributed along the wall length. The wall showed high ductility capacity, ensuring a uniform crack pattern and eliminating any localization of cracks in the web region. Liao et al. (2012), investigated the effect of reinforcing boundary element walls with a structural steel section in the confined region, where the lateral load capacity increased but failure mode could only change from shear to a mixed flexure-shear mode when the aspect ratio (height/width) was three or more. Oh et al. (2002) studied the effect of confinement and end-configurations of Reinforced Concrete structural walls, where they tested three rectangular walls and one barbell-shaped wall. They concluded that the barbell and the well-confined rectangular wall showed similar ductility and energy dissipation.

Orakcal and Wallace (2004) proposed a Multiple Vertical Line Element Model *(MVLEM)* to predict the flexural response of *RC* structural walls under cyclic loading. The model was designed to successfully capture the cyclic response of *RC* walls including

stiffness degradation, strength deterioration, and hysteretic shape. Orakcal and Wallace (2006) compared the *MVLEM* results with the experimental results and the model was capable of predicting the capacities, average rotations over the region of inelastic deformations, and neutral axis position. However, the *MVLEM* underestimated the compressive strains and was not accurate in predicting the non-linear tensile strain distributions in the flanges of t-shaped walls. Kolozvari et al. (2015a) proposed a model to accurately capture the nonlinear flexural/shear interaction of the cyclic response of reinforced concrete structural walls. The model successfully captures the hysteretic loops of the overall load-displacement relationship. Kolozvari et al. (2015b) experimentally calibrated and validated the analytical model proposed with five moderately slender reinforced concrete walls experiencing extensive levels of shear-flexure interaction. Concluded that the Shear Flexure Interaction *(SFI) MVLEM* was effective in predicting the contribution of the flexural and shear of the lateral deformation along the height of the *RC* structural walls.

Other researchers (Paulay and Uzumeri 2015; Paulay 2001; Mitchell et al. 2003) discussed the provisions of the seismic code by quantifying the plastic hinge length, the methodology behind proposed ductility-related modification factors, and shifting to performance-based design. Mitchell et al. (2010) and Adebar et al. (2004), carried out studies to compare the different versions of the Canadian seismic code provisions, corresponding to shear wall design, over the last few decades.

The shake table testing reported by Ghorbanirenani et al. (2012) showed that the peak base shear force developed prior to any significant inelastic wall rotations and that

walls experienced limited inelastic flexural deformations at their bases. In addition, the maximum inelastic rotation did not occur simultaneously with the maximum roof displacement. The study also reported inelastic flexure response due to higher modes effects. Subsequently, the study recommended consideration of inelastic flexure response further away from the wall base, due to higher modes effects, in future design provisions. Lu et al. (2014) concluded that the current provisions of the National Building Code of Canada *(NBCC)* (2010) and CSA A23.3-14 (2014) underestimated the wall base shear force demands by *15%* to *70%*. In addition, they indicated that future design provisions should consider amplifying the design bending moments above the plastic hinge region in order to constrain the plastic deformation to the plastic hinge region at the base of the wall.

The objective of the current study is to investigate how the level and distribution of vertical reinforcement can influence the wall failure mechanism as discussed in the Canterbury earthquake report. As it is usually expected that walls with low vertical reinforcement ratios would possess higher ductility capacities than walls with higher vertical reinforcement ratios; which was not the case during the Canterbury earthquake.

2.3 EXPERIMENTAL PROGRAM

The experimental program was conducted to quantify the influence of configuration and vertical reinforcement ratio on the ductile capabilities of reinforced concrete (*RC*) structural walls. A fully reversed cyclic displacement-controlled load was applied quasi-static to the top of the walls as shown in Figure 2.1 while the wall was subjected to a constant axial load throughout the test. The testing of each wall was terminated when the

maximum capacity degraded to *50%*. All the walls were detailed as ductile structural walls according to CSA A23.3-14 (2014). The following sections highlight the material properties, design, construction, test setup, and instrumentation. This is followed by a discussion of the failure modes, load-displacement relationships, displacement ductility, and strength and stiffness degradations.

2.3.1 Test Matrix and Wall Design Criteria

Phase I walls (*W1*, *W2*, *W3*) were designed to have approximately the same strength while having the same overall dimensions and being subjected to the same axial load, in order to facilitate direct comparison between their displacements and ductility capabilities. The same comparison can be conducted to the *Phase II* walls (*W4*, *W5*, *W6*) as they were also designed to have approximately the same strength, yet different reinforcement ratios from those tested in *Phase I*.

The six half-scaled *RC* walls (two rectangular, two flanged, and two with boundary elements) were constructed with the same overall dimensions but different cross-sections as shown in Figure 2.2. *Phase I* walls vertical reinforcement ratios (ρ_v) of the rectangular Wall *W1,* the Flanged Wall *W2,* and the Wall with boundary element *W3* were *1.17%*, *0.66%,* and *0.69%*, respectively. For the other three (*Phase II*) walls, as listed in Table 2.1, the vertical reinforcement ratios were *2.80%*, *1.58%*, and *1.63%* for the rectangular Wall *W4,* the flanged Wall *W5,* and the boundary element wall *W6*, respectively. All wall characteristics are listed in Table 2.1. All the walls were reinforced with two layers of

vertical reinforcements, which limited out-of-plane displacement and increased stability when the walls were under inelastic strains (Paulay and Priestley 1992).

All walls were horizontally reinforced to resist the lateral shear load according to the CSA A23.3-14 (2014) provisions. As such, *Phase I* rectangular wall horizontal reinforcement ratio *(ρ_h)* was *0.63%*, whereas the corresponding horizontal reinforcement ratio for *Phase I* flanged and boundary elements walls was *0.55%.* With the expected higher capacities of *Phase II* walls (due to the increased flexural reinforcement ratios), ρ_h was *1.28%* for the rectangular wall and *1.05%* for the flanged and boundary elements walls. Confinement ties were detailed and spaced according to the CSA A23.3-14 (2014) standards for buckling prevention. Where the confinement reinforcement spacing (at half-scale) was *55mm* for the boundary elements Wall *W6* and *45mm* for the remaining walls. In the heavily reinforced region, each vertical reinforcement was laterally supported by the corner of the tie or an inclined angle of not more than *135°* as specified by the CSA A23.3-14 (2014) as shown in Figure 2.2.

It is worth noting that the addition of flanges and boundary elements to the walls and the concentration of part of the reinforcement at the wall end resulted in approximately *30%* reduction of the vertical reinforcement as opposed to their rectangular counterpart.

2.3.2 Material Characteristics

The concrete of the walls was poured in two stages. The maximum aggregate size was *10mm* for the six half-scale walls. Twelve concrete cylinders with a diameter of *150mm* and a height of *300mm* were prepared and tested under compression from each pour

(ASTM C39M 2010). The cylinders were tested at the ages of *7* days, *14* days, *28* days, and just before the wall test. The average concrete compressive strengths for all the walls are listed in Table 2.2(a). The use of the same concrete for all three walls was intended to facilitate the comparison between rectangular, flanged, and boundary elements walls.

The half-scaled versions of *M10*, *M15*, and *M20* (*100mm*^{2}, *200mm*^{2}, and *300mm*^{2}, respectively) bars used to reinforce the test walls were, respectively, *D4*, *D7*, and *D11* bars having cross-sectional areas of *26mm*^{2}, *45mm*^{2}, and *71mm*^{2}, respectively. as shown in Table 2.2(b). The *D4* bars were used as the horizontal reinforcements for all the walls and were used as the distributed vertical reinforcements for Walls *W2* and *W3*. The *D7* bars were used as vertical reinforcement in the outer parts of *W2* and *W3* throughout the entire cross-section of *W1* and on the inner parts of *W5* and *W6*. Finally, the *D11* bars were used as the vertical reinforcements of Wall *W4* throughout the section and on the outer parts of the heavily reinforced areas of Walls *W5* and *W6* as shown in Figure 2.2(e and f).

Three *600mm* test coupons of each bar size were tested under tension following ASTM A615-09 (2009). The average yield strength of the *D4* and *D7* bars were *510MPa (c.o.v. = 3.5%)* and *480MPa (c.o.v.= 2.8%)*, respectively, with elongation of *8.0%*, and *10.7%*, respectively. The *D11* bars had an average yield strength of *420MPa (c.o.v.= 6.9%)* and *9.4%* elongation. The average ultimate strength of *D4*, *D7,* and *D11* bars were *556MPa (c.o.v.= 3.4%)*, *526MPa (c.o.v.= 2.1%)*, and *511MPa (c.o.v.= 4.2%)*, respectively.

2.3.3 Construction, Test Setup, and Instrumentation

All the walls consisted of three-story with the same overall height and width *(3,990 mm × 1,802 mm)*. The height of each story was *1,230mm* in addition to *100mm* slab thickness extending *150mm* in both out-of-plane sides as shown in Figure 2.1. The vertical reinforcement of the wall was extended and bent into the foundation extending *250mm* from each side of the wall. The *RC* foundation had a width of *2,300mm*, a height of *400mm,* and a depth of *500mm*. The concentrated reinforcement regions at each end had one rectangular tie for Walls *W1* and *W4* while two rectangular ties were used for Walls *W2* and *W5*. Regarding Walls *W3* and *W6* two ties (rectangular and hexagonal) were used on each end as shown in Figure 2.2.

Each wall was placed on the reusable slab in the test setup as shown in Fig. 2.1(a). A built-up steel U-shaped loading beam was connected and coincided with the hydraulic actuator to uniformly transfer the simulated earthquake loading on the entire length of the wall as opposed to a concentrated load at the wall corner. The lateral cyclic loading of the wall was applied using a displacement-controlled hydraulic actuator with a maximum stroke of *± 250mm* and a maximum capacity of *± 500kN*. Six out-of-plane steel sections were connected to the wall for lateral stability as shown in Figure 2.1(b). The out-of-plane members were designed and installed to prevent out-of-plane movement while allowing lateral movements and rotations in the in-plane directions.

The axial load was incorporated in the test via two force-controlled hydraulic actuators, which were connected to four threaded rods (two from each side of the box

section) as shown in Fig. 2.1. The applied load on each rod was maintained at *40kN* resulting in a total constant axial load on the wall of *160kN*.

Thirty-eight displacement potentiometers were used to measure and record the sliding, vertical, and lateral displacements at various points on the wall. Fourteen electrical strain gauges were attached to the four outermost vertical reinforcement bars. The strain gauges locations for the first two bars were placed *200mm* below the interface between the wall and the foundation, at the interface, at *100mm* above the interface, at a height of *900 mm* corresponding to half of the length of the wall *($l_w/2$)* and at a height of *1,800 mm (l_w)*. The second two bars had one strain gauge *50mm* above the interface and at a location equal to the length of the wall *1,800mm (l_w)*.

The strain gauges located below the interface and in the foundation were used to determine the extent of plasticity in the foundation which could significantly affect wall top displacement as discussed by Priestley et al. (2007) and Shedid and El-Dakhakhni (2014).

A target wall resistance equal to *20%* of the theoretical yield load F_y was considered in the first loading cycle and was followed by target resistance of *40%*F_y, *60%*F_y, and *80%*F_y. The loading was then continued until the experimental yield load Q_y and corresponding top wall displacement Δ_y were determined. After reaching the yield strength, displacement-controlled loading, based on multiples of the experimentally determined yield displacement was followed until the wall resistance degraded to approximately *50%* of its maximum values, at which point the test was terminated.

2.4 TEST RESULTS

The walls' lateral load capacities, load-displacement relationships, crack patterns, failure modes, load-displacement envelopes, and stiffness degradation are presented and discussed in the following sections. In addition, the displacement ductility values for each wall were computed and compared.

2.4.1 Lateral Load Capacities

The theoretical and experimental yield strength, Q_y, and ultimate flexural strength, Q_u, for all walls were listed in Table 2.3. Using mechanics, the strength predictions, ignoring material or strength reduction factors, were determined according to the CSA A23.3-14 (2014) by limiting the extreme fiber compressive strain for concrete to *0.0035*. The predicted yield loads for *Phase I* walls were slightly conservative while *Phase II* predicted yield loads were more in agreement with the experimental results. On the other hand, the predicted ultimate strengths of all the specimens were similar to the experimental results except in Wall *W1* where a construction error occurred at the East Toe as explained earlier. While the difference in the push direction can be due to the strain hardening of the vertical reinforcements *D7* bars.

2.4.2 Wall Load-displacement Relationships and Failure Modes

The load-displacement hysteresis relationships of all the test walls are plotted in Figure 2.3. The yield load Q_y and ultimate load Q_u are shown in the push and pull directions on each hysteresis loop graph. A table is inserted in each graph to show the yield load Q_y, the

maximum load Q_u, and the load at 20% strength degradation $Q_{0.8u}$, along with their corresponding displacements. The bottom right table in each graph shows the wall key features including the wall length, l_w, height, h_w, vertical, ρ_v, horizontal, ρ_h, reinforcement ratios as well as the axial load, P, applied on the wall. The top right quadrant shows the load-displacement relationships in the push direction where the East toe was under tension and the west toe was under compression and vice-versa as seen for the bottom left quadrant. Prior to yielding, the slope of the hysteresis loops indicated higher stiffness of the wall compared to loading beyond yield where the slopes of the loading portion of the hysteresis loops of each cycle showed gradual stiffness degradation for all walls. The hysteresis loops after yield started widening which would increase energy dissipation capabilities for walls. In general, all walls failed in a flexural manner characterized by the crushing of the concrete at the toes followed by the buckling of the vertical bars, and finally, the outermost vertical reinforcements fractured and the wall strength degraded significantly.

2.4.2.1 Wall W1

The hysteresis loops for Wall *W1* are shown in Figure 2.3(a). The first yield at the outermost bars was recorded at *152kN* and *123kN* in the push and pull directions, respectively corresponding to displacements of *7.4mm* and *9.2mm* in the push and pull directions, respectively. The average yield displacement taken as $\Delta_y = 8.4mm$ (*0.21%* drift) was then selected to determine the target displacement levels as multiple of yield displacement.

The recorded ultimate load Q_u was *230kN* in the push and *172kN* in the pull loading direction corresponding to a top displacement of *22.7mm* (*0.57%*) and *17.1mm* (*0.43%*),

respectively. The wall reached its ultimate load at $3\Delta_y$ during the push cycle, while in the pull loading direction the wall reached its ultimate strength during the $2\Delta_y$ loading cycle. The variability in the strength and displacement could be in part due to an accidental problem during the concrete pouring as minor voids were discovered at the East toe of the wall and were later repaired using high strength low shrinkage repair mortar as they were necessary prior to testing. At $4\Delta_y$ (*0.84%* top drift), the concrete was crushed during the first loading cycle at both wall toes and during the second loading cycle 3 vertical reinforcement bars fractured in the East end of the wall as listed in Table 4 (where repair mortar was used). At $5\Delta_y$ loading cycle corresponding to *42.0mm* (*1.05 %* drift), 5 outermost West vertical bars fractured. The wall was then loaded even further to $6\Delta_y$ (*1.26 % drift*), where both corners were heavily damaged as shown in Figure 2.4(a) and the test was terminated.

2.4.2.2 Wall W2

The experimental yield Q_y load for wall *W2* was *175kN* and *158kN* in the push and pull directions, respectively, and corresponded to displacements of *8.9mm* (*0.22%* drift) and *8.4mm* (*0.21%* drift), respectively. Due to a minor error in identifying the actual yield displacement Δ_y while testing, the wall was pushed in multiples of *10 mm*. At $2.3\Delta_y$ (*0.50%* drift) the wall reached its maximum capacity of *187kN* in the push and *183kN* in the pull directions as shown in Figure 2.3(c). At $4.6\Delta_y$ (*1.00%* drift) displacement level, concrete was crushed at the flanges, the vertical bars buckled, and the first bar fractured. The ultimate level displacement $\Delta_{0.8u}$ was reached in the push and pull directions at *0.70%* and *0.95%* top drifts, respectively. When the wall was loaded to $5.8\Delta_y$ (*1.25%* drift), all the bars

in the flanges fractured, in addition to the 8 outermost bars in the East and the 10 outermost bars in the webs on the west side. At this point, the wall strength degraded by more than *50%* of the maximum capacity, and the test was terminated.

This wall did not show the expected ductility due to a localized failure at the interface between the wall and the foundation. The interface crack started opening up and the tensile steel strain and plastic deformations were concentrated at the bottom of the wall as evident from the cracking pattern in Figure 2.4(b).

2.4.2.3 Wall W3

The experimental yield strength of wall *W3* occurred at a load of *160kN* with a displacement Δ_y equal to *8.5mm* (*0.21%* top drift) and *8.1mm* (*0.20%* top drift) in the push and pull directions, respectively. The maximum recorded strength of the wall was *176kN* and *177kN* in the push and pull directions, respectively, and was reached corresponding to $2\Delta_y$ (*0.42%* drift) displacement level, as shown in Figure 2.3(e). At $4\Delta_y$ (*0.84%* drift) displacement level, the concrete around the boundary elements was crushed, and the bars buckled as listed in Table 2.4. In the second cycle of $4\Delta_y$ (*0.84%* drift), loading two bars were fractured in the pull direction. The ultimate level displacements of the wall were *1.00%* and *0.90%* (top drift) in the push and pull directions, respectively. When the wall was pushed to a displacement level of $5\Delta_y$ (*1.05%* drift) two bars fractured in each direction as shown in Figure 2.4(c). The wall was further pushed to $6\Delta_y$ (*1.26%* drift) and all the bars in the boundary elements fractured in both directions and the strength degraded to less than *50%* of the maximum capacity so the test was terminated.

The wall showed moderate ductility compared to what was expected. However, due to a lift-up in the interface after concrete crushing in the boundary elements, the outermost reinforcement strained plastically at the interface crack. The unexpected moderate ductility stated earlier as the enhancement in the ductility of boundary elements wall *W3* compared to rectangular wall *W1* was lower than the enhancement of boundary elements wall *W6* when compared to rectangular wall *W4*.

2.4.2.4 Wall W4

The hysteresis loops for wall *W4* are shown in Figure 2.3(b). The first crack in the wall occurred at *60%* of the theoretical yield strength, F_y. The wall experimental yield loads were *222kN* in the push and *195kN* in the pull corresponding to top displacements of *12.6mm* (*0.32%* top drift) and *9.2mm* (*0.23%* top drift), respectively. The maximum strength of the wall was recorded at $3\Delta_y$ (*0.84%* drift) displacement level, and was equal to *336kN* in the push and *355kN* in the pull. At the second cycle of $3\Delta_y$ (*0.84%* drift) chunks of concrete spalled at both ends as listed in Table 2.4. As the wall was approaching $4\Delta_y$ (*1.13%* drift) displacement level, concrete crushing occurred on the compression side, and 2 of the outermost vertical bars were fractured on the tension side as shown in Figure 2.4(d). The strength of the wall then degraded rapidly to *191kN* and *248kN* in the push and pull cycles, respectively. At the second cycle of $4\Delta_y$ (*1.13%* drift) displacement level, the strength degraded to less than 50% of the maximum capacity, and the test was terminated.

2.4.2.5 Wall W5

This wall failed in a flexural ductile manner, but unfortunately, the strength when the wall was pushed to the west was degraded as seen in Figure 2.3(d), as there were significant

cracks in the foundations located in the East corner occurred at $2.6\Delta_y$ displacement level inducing a bar bond slip. Bracing was performed and the wall was successfully tested. However, the damage caused is explained later.

There was a minor error to determine the real yield displacement Δ_y due to the bond slip. The actual experimental yield displacement was later identified from the analysis of the experimental results and was used to quantify the corresponding actual displacement levels experienced by the wall. The wall experimental yield loads were *220kN* in the push and *270kN* in the pull, corresponding to lateral top displacements equal to *7.3mm* (*0.18%* top drift) and *9.2mm* (*0.23%* top drift) for the push and pull directions, respectively. At $2.6\Delta_y$ (*0.84%* drift) displacement level, the maximum capacity of the wall reached values of *332kN* and *313kN* in the push and pull directions, respectively. At $3.7\Delta_y$ (*0.85%* drift) displacement level, the West corner flanged toe crushed and the bars buckled. During the loading to $5.1\Delta_y$ (*1.15%* drift) displacement level, 4 bars fractured in the flanged region located in the West toe as indicated in Table 2.4. The wall reached its ultimate level displacement at *52mm* (*1.30%* drift), while at $6.4\Delta_y$ (*1.45%* drift) displacement level, all the bars in the flanged area fractured in addition to 4 bars in the webs as shown in Figure 2.4(e). At $8.0\Delta_y$ (*1.80%* drift) displacement level, the strength degraded to less than *50%* of the maximum capacity, and the test was terminated.

2.4.2.6 Wall W6

The wall showed a yielding stage at *227kN* and *209kN* in the push and pull directions, respectively. The average Δ_y was taken equal to *10.5mm* (*0.26%* top drift). The hysteresis loops continued to widen and energy dissipation increased after yielding as

shown in Figure 2.3(f). The maximum load Q_u was recorded at $3\Delta_y$ (0.79% drift) displacement level and was equal to *334kN* in the push direction and *313kN* in the pull direction. At $4\Delta_y$ (*1.05%* drift) displacement level, uplift of the tension side was observed and minor concrete spalling was visible in the compression zone. At $5\Delta_y$ (*1.32%* drift) displacement level, toe crushing occurred at both ends of the wall, and 7 reinforcement bars were buckled in the East boundary element while 4 bars buckled in the West boundary element as shown in Figure 2.4(f). At $6\Delta_y$ (*1.58%* drift) displacement level, 4 vertical reinforcement bars fractured in the East end and 2 others in the West end, and the ultimate level displacement $\Delta_{0.8u}$ was reached as listed in Table 2.4. At $8\Delta_y$ (*2.1%* drift) displacement level, all the vertical reinforcement bars in the confined regions fractured in addition to the outer four vertical bars on the East side and two on the West sides of the wall web. Furthermore, the wall strength degraded to *50%* of the maximum capacity, and the test was terminated.

In *Phase II*, flanged $(\rho_v = 1.58\%)$ and boundary elements $(\rho_v = 1.63\%)$ hysteretic curves showed higher energy dissipation when compared to their rectangular counterpart and when compared to *Phase I* flanged and boundary elements walls. Due to localized failure at the interface, *Phase I* flanged $(\rho_v = 0.66\ \%)$ and boundary elements $(\rho_v = 0.69\%)$ walls did not show high-energy dissipation. Regarding the rectangular walls, *Phase I* Wall *W1* $(\rho_v = 1.17\%)$ the hysteretic loops showed higher energy dissipation than wall *W4* $(\rho_v = 2.80\%)$. The walls with boundary elements and flanges did not only experience increased energy dissipation capacities, but also, due to their lesser/controlled damage in their

respective compression zones, showed lesser pinching, than their rectangular wall counterparts.

Pinching in all the walls was very minimal up to their respective maximum capacities. Beyond the drift corresponding to their maximum capacities, *Phase I* flanged and boundary elements walls showed higher pinching levels when compared to their *Phase II* counterparts due to the concentration of the primary crack located at the wall/base interface. This can be observed in the load-displacement relationships of the walls presented in Figures 2.3(c), (d), (e), and (f). Minimal pinching occurred for all the walls after the crushing of the concrete at the toes. Regarding the rectangular walls, minimal pinching occurred after at $4\Delta_y$ displacement level for both walls. While *Phase II* flanged Wall *W5*, Pinching was visible in Figure 2.3(d) during the loading to $5.1\Delta_y$ (*1.15%* drift) displacement level. The hysteretic curves of the boundary element Wall *W6* showed minimal pinching at $5\Delta_y$ (*1.32%* drift) displacement level. Regarding *Phase I* flanged and boundary elements walls, pinching occurred at $4.6\Delta_y$ (*1.00%* drift) and $4\Delta_y$ (*0.84%* drift) displacement levels, respectively. With increasing pinching, the observed damage to the walls increased and the confined region reinforcement bars buckled for all walls. Moreover, it increased relatively at higher displacement levels after the bars buckled up to the wall's failure. Overall, pinching was minimized due to the high contribution of flexure when compared to shear in the formation of the hysteretic curves as agreed with Kolozvari et al. (2015b).

The flanged and boundary elements walls in *Phase I* did not show the expected ductility when compared to their rectangular counterpart. That was due to the difference in

failure when compared to *Phase II* walls as a primary flexural crack was observed at the interface located at the tensile portion of the wall. High tensile strain demand was required in the tensile portion of the wall, thus the primary crack at the interface occurred. As the wall toe region experiences compression, the compression is resisted mainly by the boundary element and the flange of Walls *W3* and *W2* Walls, respectively, as a result of their webs instability. In other words, for these walls, the neutral axis remained within the boundary element or the flange, resisting higher compressive stresses, and thus strains, to maintain equilibrium. At higher ductility levels, the compressive toe experiences higher levels of stress, which resulted in concrete spalling of the boundary element, and then only the inner confined area resists compression. After that, reinforcement bars typically buckled and the strength degraded rapidly. Subsequently, the walls failed without reaching their expected high inelastic displacement levels. In addition, as the walls developed primary flexural cracks, the plastic straining of the reinforcement was typically localized in the vicinity of the crack. At higher displacement levels, the reinforcements experienced increased concentrated plastic deformation until fracture, which also limited the plastic hinge length, resulting in unexpected low performance. This is consistent with the results of Gilbert and Smith (2006), concluding that although the member is ductile in the critical cross-section, a non-ductile response due to the localization of the plastic deformation of the reinforcement bar was observed.

2.4.3 Cracks pattern

The first crack was observed at around *60%* and *80%* of the theoretical yield load of each wall. Up to the yield load, most of the cracks were flexural cracks for *Phase I* walls, and at further loading, inclined shear cracks started to form. For *Phase I* walls, few flexural cracks were observed at the bottom half of the second story and minimal hairline diagonal shear cracks were observed within the second and third stories. *Phase II* walls shown in Figures 2.4(d, e, f) had extensive flexural and diagonal shear cracks compared to the *Phase I* walls shown in Figure 2.4(a, b, c). For *Phase II* walls, flexural cracks were visible over the entire first story and the bottom half of the second story at $80\%F_{y,}$ and diagonal shear cracks were observed over the first and the second stories before yielding. After the first yield, more inclined shear cracks were observed over the first story, relatively less in the second story, and very few occurred over the third story. For all the specimens, once the concrete toe was crushed few new cracks formed, and existing cracks started to extend both in width and length. At such a loading stage, the hysteresis loops would typically get wider as a result of the high energy dissipation due to crushing at the toes and buckling in the outermost vertical bars in addition to the widening of the existing cracks.

2.5 Analysis of Experimental Results

2.5.1 Walls Damage Quantification

According to the Federal Emergency Management Agency *(FEMA P58)* (2012), damage states are related to the residual story drift and are classified into four levels. The first damage state *(DS1)*, is reached when non-structural repairs are needed and occurs when

the story residual drift reaches *0.2%* the height of the story, whereas, the second damage state *(DS2),* is specified corresponds to story drift equal to *0.5%* and when structural realignment and repairs are needed to limit degradation of the structure stability. The third damage state *(DS3)*, is defined as when a major structural realignment is required to restore the safety margin for lateral stability. At such a point the structure might be a total economic loss and expected to occur at *1%* story drift. At *DS3* the cost of repairs for the existing building exceeds the construction of a new one so it is more economical to build a new building. Finally, the fourth damage state *(DS4)*, is reached when the residual drift is larger than *1 %* to the extent that the structure is in danger of collapse from seismic aftershocks. *DS4* indicates that the building is on the verge of collapsing and structural repairs are not an option, therefore a new building is inevitable.

Table 2.4 shows the occurrence of each damage state while the specimen was tested. The displacement level cycles written on the right side of the table indicate that the selected specimen reached the specified damage state at the mentioned displacement cycle.

The first *(DS1)* and second *(DS2)* damage states, occurred at the same displacement ductility levels for all walls except for the rectangular walls where *DS1* was reached at $2\Delta_y$ for Wall *W1* and $3\Delta_y$ for Wall *W4*. As seen in Table 4.4, *DS3* for Wall *W4* was not reached as the wall reached its *DS2* after the first $4\Delta_y$ displacement level cycle, however, due to bar snapping, the wall was on the verge of collapsing *DS4* after performing the second $4\Delta_y$ cycle. *Phase II* flanged and boundary elements walls showed higher displacement ductility levels for higher damage states when compared to their *Phase I* counterparts. This reflects the enhanced seismic performance of both the flanged Wall *W5* with a higher reinforcement

ratio *(ρ_v%= 1.58)* and the boundary elements Wall *W6 (ρ_v%= 1.63)*. On the other hand, for the rectangular walls, higher ductility levels corresponding to the *DS3* and *DS4* levels were achieved by Wall *W1 (ρ_v%= 1.17)* when compared to those of Wall *W4 (ρ_v%= 2.80)*. Moreover, a relatively higher reinforcement ratio and well-distributed web reinforcement of flanged and boundary elements walls would reach the damage state levels at higher ductility levels.

2.5.2 Load-Displacement Envelopes

Load-displacement relationships for each specimen were constructed and compared in Figure 2.5. The cross-sectional configuration of the flanged and the boundary elements Walls (*W2* and *W3*) having less vertical reinforcement ratio compared to rectangular Wall *W1*, were expected to show higher ductile capability but due to the localized cracking between the wall and the foundation, which concentrated the steel plastic strain at the interface, these walls did not show the intended seismic performance. As shown in Figure 2.5(b), the rectangular Wall *W4* had a lower ductile capability and lower ultimate drift when compared to the flanged Wall *W5* and the wall with boundary elements *W6*. The increase in the drift ratios of Walls *W5* and *W6* was due to the configuration and the confinement of the horizontal hoops at the heavily reinforced regions. It can be inferred that flanges and boundary elements enhance the structural wall performance allowing the wall to reach higher drifts with a slower strength degradation rate. As shown in Figures 2.5(b) and 6(b), the load-displacement envelope of *W5* in the push direction was not added

in the comparison due to foundation cracks as mentioned earlier in the load-displacement relationships section.

To facilitate comparison between the walls, the load was normalized for each specimen, as *Phase II* wall strengths were higher than those in *Phase I.* As shown in Figure 2.6 *Phase II* walls had higher displacement (top drifts) compared to *Phase I* walls at both maximum and ultimate load capacities. The reasons for such higher displacements were related to the effect of the primary cracks leading to a concentration of the steel plasticity at those locations and consequently localizing the plastic curvature and the plastic hinge length over a relatively small height above the foundation level. While for *Phase II* higher vertical reinforcement forced the walls to initiate a larger number of horizontal flexural cracks as well as diagonal shear cracks in addition to secondary flexural cracks. These secondary cracks distributed the high tensile in the outermost vertical reinforcement over a larger length, which resulted in spreading the high curvatures at the base of the wall over a larger zone and extending the plastic hinge length. Such a phenomenon resulted in turn in increased top displacements corresponding to maximum and ultimate capacities for walls with higher reinforcement ratios as opposed to those with lower ratios. The discussed results agree with the Canterbury Commission Report (2011).

Table 4.5 showed the yield displacement Δ_y, displacement at the maximum load Δ_u and ultimate displacement at *20%* strength degradation $\Delta_{0.8u}$ as well as the corresponding percentage drifts. The yield displacement for all the walls varied between *8.3mm-10.9mm* (*0.21%-0.27%* drift). The maximum loads were reached for *Phase I* walls at top drifts varying between *0.42%-0.69%*, while *Phase II* wall maximum loads were achieved at top

drifts that varied between *0.72%-0.85%*. Drifts corresponding to ultimate displacement (at *20%* strength degradation) for *Phase I* varied between *0.70%-0.98%* while varied between *1.15%-1.58%* for *Phase II* specimens. As discussed it was clear that *Phase II* had higher top displacements at maximum load and *20%* strength degradation when compared to *Phase I* walls.

2.5.3 Displacement Ductility

The seismic performance could better be quantified by evaluating the displacement ductility values, as high ultimate displacement values do not necessarily imply high ductility capacities. The experimental displacement ductility values in this section were computed by dividing the displacement at the target displacement level (Δ) by the yield displacement (Δ_y). The yield displacement (Δ_y) was the lateral displacement when the first outermost vertical reinforcement started yielding. The displacement ductility values for all the walls at the maximum load μ_Δ and *20%* strength degradation (ultimate displacement) $\mu_{\Delta 0.8u}$ are presented in Figure 2.7. The displacement ductility covers fully the kinetic energy dissipated from the structural wall.

The displacement ductility values calculated at the maximum load μ_Δ varied between *2.0-2.7* in *Phase I* walls, and between *2.6-3.7* for walls in *Phase II* as indicated in Table 4.5. The displacement ductility values at ultimate displacements $\mu_{\Delta 0.8u}$ for *Phase I* walls ranged between *3.2* and *4.7*, whereas for *Phase II* walls, $\mu_{\Delta 0.8u}$ varied between *4.2* and *6.0*. As such, it is clear in *Phase II* that the displacement ductility values attained by the flanged and boundary elements walls were, respectively *33%* and *40%* higher than that

attained by their rectangular counterpart. The reason for the higher ductile capacity was the confinement and the configuration of the flanges and the boundary elements, which confined the concrete from crushing at earlier stages and enabled sustaining the lateral load capacity at high drift levels. On the other hand, the similar ductility values for *Phase I* could be justified based on the generation of the primary cracks at the interface for walls *W2* and *W3* that controlled the failure and limited the ductility due to high plastic strains concentrated in a relatively smaller length and the relatively low number of bars, acting as dowels between the foundation and the base of the wall, controlling the sliding after generation of the primary crack extending over the entire length of these walls.

2.5.4 Idealized Displacement Ductility

The idealized displacement ductility values μ_{Δ}^{id} were determined based on bilinear idealization (elastic-perfectly plastic system) performed by Priestley et al. (2007) It offers a conservative yield displacement value, which is the intersection of the yield stiffness K_y line with a horizontal line from the maximum capacity Q_u. The maximum capacity idealized displacement ductility $\mu_{\Delta u}^{id}$ was determined by dividing the lateral displacement at the maximum by the idealized yield displacement. While the ultimate idealized displacement ductility $\mu_{\Delta 0.8u}^{id}$ was the lateral displacement at *20%* strength degradation by the idealized yield displacement.

The idealized displacement ductility at the maximum capacity $\mu_{\Delta u}^{id}$ varied between *1.5- 2.2* and *1.7-3.2* for *Phase I* and *Phase II*, respectively as listed in Table 4.5. *Phase I* flanged Wall *W2* achieved a higher $\mu_{\Delta u}^{id}$ by *24%* when compared to rectangular Wall *W1*.

While the boundary elements Wall *W3* showed a similar $\mu_{\Delta u}^{id}$ in the push direction and showed *1.26* times the rectangular $\mu_{\Delta u}^{id}$ value in the pull direction. In *Phase II*, the flanged and the walls with boundary elements average higher than their rectangular counterpart by *1.8* and *1.2* times, respectively. Regarding the idealized displacement ductility value at *20%* strength degradation $\mu_{\Delta 0.8u}^{id}$, *Phase I* walls varied between *2.9* and *4.3* while *Phase II* walls ranged from *2.4-4.9* as listed in Table 4.5. *Phase I* boundary element Wall *W3* average $\mu_{\Delta 0.8u}^{id}$ was *1.4* times the rectangular Wall *W1* idealized displacement ductility. While the flanged wall resulted in *1.3* times, the rectangular value in one direction and the same $\mu_{\Delta 0.8u}^{id}$ value in the other. *Phase II* flanged and boundary elements walls achieved a higher average $\mu_{\Delta 0.8u}^{id}$ when compared to their rectangular counterpart by *90%* and *60%*, respectively.

Phase II showed higher average idealized displacement values at maximum capacity compared to *Phase I* walls. While the average idealized displacement ultimate level $\mu_{\Delta 0.8u}^{id}$of *Phase II* were, higher than *Phase I* walls for the flanged walls by *44%*, similar to the boundary elements walls, and slightly lower by *10%* than the rectangular walls.

Flanged and boundary elements walls in *Phase II* showed an enhanced seismic performance when compared to their rectangular counterpart. That was due to the well-detailed flange and boundary element for walls *W5* and *W6* respectively. A larger confined area was able to resist the increasing compressive stress delaying buckling of the confined region due to adequate transverse reinforcement and hoop detailing. Moreover, due to the higher concentration of the reinforcement at the confined region of the boundary elements

and the flanged walls, the wall was more able to resist higher tensile strain demands when compared to the rectangular wall *W4*. Hence, *Phase II* flanged and boundary elements walls experienced enhanced seismic performance. Furthermore, it is essential to reinforce the web region adequately to expect higher seismic performance, as Walls *W2* and *W3* did not show the expected ductility capacity when compared to their rectangular counterpart Wall *W1* due to a localized flexural primary crack, where the plastic straining of the reinforcements was localized at the primary crack locations.

2.5.5 Stiffness Degradation

Figure 2.8 shows the stiffness degradation from yield to failure of each wall versus displacement levels Δ/Δ_y. At yield K_y, ranged between *14.3-30.1kN/mm,* while at the ultimate loads K_u varied between *9.3-11.8kN/mm* for all the specimens shown as red points in Figure 2.8. The stiffness at *20%* strength degradation $K_{0.8u}$ for all the walls was between *2.0-7.6kN/mm*. It was observed that both rectangular walls had higher $K_{0.8u}$ when compared to the flanged and the boundary elements walls for both Phases. This implies that the flanged and boundary elements walls would attract less base shear at higher displacement levels when compared to the rectangular walls. Figure 2.8 shows that *Phase II* walls have higher stiffness values at the ultimate level $K_{0.8u}$ when compared to their *Phase I* counterparts. All the specimens resulted in similar stiffness values at the maximum load K_u. As shown in Figure 2.8, the stiffness degrades at a higher rate for *Phase I* walls when compared to their *Phase II* counterparts, which is due to the difference in the intensity of failure between *Phase I* and *Phase II* walls. *Phase II* walls had extensive cracks and

crushing of the concrete, which lowered the stiffness degradation rate when compared to *Phase I* walls in which walls primary cracks at the interface accelerated the stiffness degradation. When comparing the stiffness degradation for the walls on each phase, similar stiffness degrading slopes were observed, as shown in Figure 2.8, which illustrates that the design base shear should be similar for all the walls at each phase. Due to the foundation cracks mentioned earlier for flanged wall *W5*, the stiffness degradation values in the push direction were not considered.

2.6 CONCLUSIONS

Strength prediction for the walls using the Canadian code CSA A23.3-14 (2014) showed an excellent agreement with the experimental strengths. At the primary crack location between the base and the wall, the strain in the steel kept increasing till the steel fractured and the concrete crushed over a small height.

The ductile capability for *Phase II* walls was better than *Phase I* walls when comparing the normalized load-displacement envelopes which is consistent with the Canterbury earthquake observations for walls with higher reinforcement ratios.

The displacement ductility values at *20%* strength degradation $\mu_{\Delta 0.8u}$ of the rectangular, flanged wall and wall with boundary elements with low reinforcement ratios were almost similar, however for walls in *Phase II* with higher reinforcement ratios, the attained displacement ductility values by the flanged and boundary elements walls were *50%* and *33%* higher than their counterparts in *Phase I*.

The displacement ductility values of the flanged wall *W5* and boundary element wall *W6* were respectively *33%* and *40%* higher than the rectangular counterpart *W4*. While, the average idealized displacement ductility values of the flanged and boundary elements walls were higher than their rectangular counterparts by *40%* and *30%* for *Phase I* walls and *90%* and *60%* for *Phase II* walls, respectively. Such findings are in line with those reported in the Canterbury Earthquake Royal Commission report (2011), which recommended concentrating the vertical reinforcements in the outer regions. Generally, wall end configurations have major effects on seismic performance; boundary elements and flanged walls tend to have higher seismic performance. This is due to the larger confined area when compared to rectangular walls. In effect, larger confined areas can resist the increasing compressive forces when the cantilever wall is loaded in-plane to higher displacement levels. Moreover, due to the higher concentration of the vertical reinforcement at the confined region, the walls could resist higher tensile strains so that the walls could achieve higher ductility capacities. The end configurations tend to delay the strength degradation at higher displacement levels, which, in turn, enhances the seismic performance of the walls.

By increasing the vertical reinforcement ratio in *Phase II* compared to what in *Phase I*, secondary cracks were observed, and the steel strain was more uniformly distributed at higher lengths, which increased the ductile capability of the seismic force-resisting structural walls. These results are also in agreement with the Canterbury Commission report (2011) recommendations of the need to increase the vertical reinforcement ratio ρ_v% to initiate secondary cracks to extend the plastic hinge length and

therefore better seismic performance can be achieved. It is essential to adequately reinforce the web region of the wall to prevent any bond-slip of the webs and to extend the plastic straining on multiple flexural cracks instead of strain localization in the vicinity of the primary flexural crack. As such, the provisions for minimum web reinforcement of seismically-detailed *RC* walls might need to be revisited.

Future editions of seismic codes might need to consider assigning different values for the ductility-related modification factor R_d for ductile walls with different configurations and related to different vertical reinforcement ratios. However, due to the limited number of specimens tested within the current study, further research is necessary to develop recommendations for code revision.

Appendix 2A. Theoretical yield load calculations

Compression in Concrete

$$Cc = Triangular\ Area\ \times\ \varepsilon_c \times E_c = \left(\frac{1}{2} b.c\right).\varepsilon_c.E_c$$

Where concrete compressive strain

$$\varepsilon_c = \frac{c\ (\varepsilon_y)}{(a_1 - c)}$$

Concrete Young's Modulus

$$E_c = 4500\sqrt{f_c'}$$

Moment of concrete,

$$M_{yconc} = C_c(\frac{l_w}{2} - \frac{c}{3})$$

Tensile force in the reinforcement at point n,

$$F_{sn} = A_{sn}.\varepsilon_{sn}.E_s$$

Sum of moments of the vertical reinforcements around the centroid (M_{steel})

$$M_{steel} = \sum_{a_n \geq \frac{l_w}{2}}^{n=1,2,3,..} (F_{sn})(a_n - \frac{l_w}{2}) + \sum_{a_n \geq \frac{l_w}{2}}^{n=1,2,3,..} (F_{sn})(\frac{l_w}{2} - a_n)$$

So the theoretical yield strength

$$Q_{yth} = \frac{M_{steel} + M_{conc}}{h}$$

Appendix 2B. Theoretical maximum capacity calculations

Compression in Concrete

$$Cc = \alpha_1 f_c' \beta_1 c\ b$$

Where,

$\alpha_1 = 0.85 - (0.0015\ f_c')$ *[CSA A23.3-14]*

$\beta_1 = 0.97 - (0.0025 f_c')$ *[CSA A23.3-14]*

Moment of concrete,

$$M_{conc} = C_c(\frac{l_w}{2} - \frac{\beta_1 c}{2})$$

Tensile force in the reinforcement at a point n,

$$\{for\ \varepsilon_{sn} \geq\ \varepsilon_y, then\ use\ \varepsilon_y\}$$
$$\{for\ -\varepsilon_y < \varepsilon_{sn} < \varepsilon_y, then\ use\ \varepsilon_{sn}\}$$
$$\{for\ \varepsilon_{sn} \leq -\varepsilon_y, then\ use\ -\varepsilon_y\}$$

$$F_{sn} = A_{sn}.\varepsilon_{sn}.E_s$$

Sum of Moment of the reinforcements around the centroid (M_{steel})

$$(M_{steel}) = \sum_{a_n \geq \frac{l_w}{2}} (F_{sn})(a_n - \frac{l_w}{2}) + \sum_{a_n < \frac{l_w}{2}} (F_{sn})(\frac{l_w}{2} - a_n)$$

So the theoretical maximum capacity (Q_{uth})

$$Q_{uth} = \frac{M_{steel} + M_{conc}}{h}$$

a_1= Distance from the outermost tensile vertical reinforcements to the end of the compression toe (mm)

a_n= Distance from the vertical reinforcement at point n to the end of the compression toe (mm)

A_{sn}= Vertical reinforcement cross-sectional area at point n (mm^2)

b = Width of the section (mm)

c = Distance from the compression toe to the neutral axis (mm)

C_c = Compressive force due to concrete (mm)

E_c= Concrete modulus of elasticity (MPa)

E_s= Reinforcement steel modulus of elasticity (MPa)

f_c'= Concrete compressive strength (MPa)

F_{sn}= Tensile or Compressive force of the reinforcements located at point n (kN)

h= Height of the wall (mm)

l_w= Length of the wall (mm)

M_{conc}= Compressive concrete moment around the centroid (kN.mm)

M_{steel} = Sum of moments of the vertical reinforcements around the centroid (kN.mm)

M_{yconc}= Compressive concrete moment around the centroid at yield (kN.mm)

n = Numbering of reinforcement locations, where n=1 is referring the outermost vertical reinforcement, n= 2 refers to the second outermost vertical reinforcement, etc.

Q_{yth}= Theoretical yield strength (kN)

Q_{uth}= Theoretical maximum capacity (kN)

α_1= Ratio of average stress in rectangular compression block to the specified concrete strength

β_1= Ratio of depth of rectangular compression block to depth to the neutral axis

ε_c= Concrete compressive strain

ε_{sy} = Reinforcement yield strain

2.7 REFERENCES

Adebar, P., Mutrie, J., & DeVall, R. (2005). Ductility of concrete walls: the Canadian seismic design provisions 1984 to 2004. *Canadian Journal of Civil Engineering*, *32*(6), 1124-1137.

Adebar, P., Ibrahim, A. M., & Bryson, M. (2007). Test of high-rise core wall: effective stiffness for seismic analysis. *ACI Structural Journal*, *104*(5), 549.

American Society for Testing and Materials (ASTM) (2009). *Standard specification for deformed and plain carbon-steel bars for concrete reinforcement.* A615/A615M-09b, ASTM International, West Conshohocken, PA, United States of America.

American Society for Testing and Materials (ASTM) (2010). *Standard test method for compressive strength of cylindrical concrete specimens.* C39/C39M-10, ASTM International, West Conshohocken, PA, United States of America.

Beyer, K., Dazio, A., & Priestley, M. J. N. (2008). Quasi-static cyclic tests of two U-shaped reinforced concrete walls. *Journal of earthquake engineering*, *12*(7), 1023-1053.

Canadian Standards Association (CSA). (2014). *Design of concrete structures*. CSA A23.3-14, CSA, Mississauga, Canada.

Canterbury Earthquake Royal Commission report. (2011). *Seismic performance Christchurch building under the Canterbury Earthquake.* Retrieved Nov. 19th, 2013, http://canterbury.royalcommission.govt.nz/Final-Report-Volume-One-Contents

Carpenter, L. D., Naeim, F., Lew, M., Youssef, N. F., Rojas, F., Saragoni, G. R., & Adaros, M. S. (2011). Performance of tall buildings in Viña del Mar in the 27 February 2010 offshore Maule, Chile earthquake. *The Structural Design of Tall and Special Buildings*, *20*(1), 17-36.

Federal Emergency Management Agency (FEMA P58) (2012). *Seismic Performance Assessment of Buildings: Damage states for residual story drifts.* Federal Emergency Management Agency (FEMA) 356, Washington D.C., USA.

Ghorbanirenani, I., Tremblay, R., Léger, P., & Leclerc, M. (2012). Shake table testing of slender RC shear walls subjected to eastern North America seismic ground motions. *Journal of Structural Engineering*, *138*(12), 1515-1529.

Gilbert, R. I., & Smith, S. T. (2006). Strain localization and its impact on the ductility of reinforced concrete slabs containing welded wire reinforcement. *Advances in Structural Engineering*, *9*(1), 117-127.

Jünemann, R., Hube, M., De La Llera, J. C., & Kausel, E. (2012, September). Characteristics of reinforced concrete shear wall buildings damaged during 2010 Chile earthquake. In *Proceedings of the 15th World Conference of Earthquake Engineering*.

Kolozvari, K., Orakcal, K., & Wallace, J. W. (2015). Modeling of cyclic shear-flexure interaction in reinforced concrete structural walls. I: Theory. *Journal of Structural Engineering*, *141*(5), 04014135.

Kolozvari, K., Tran, T. A., Orakcal, K., & Wallace, J. W. (2015). Modeling of cyclic shear-flexure interaction in reinforced concrete structural walls. II: Experimental validation. *Journal of Structural Engineering*, *141*(5), 04014136.

Liao, F. Y., Han, L. H., & Tao, Z. (2012). Performance of reinforced concrete shear walls with steel reinforced concrete boundary columns. *Engineering structures*, *44*, 186-209.

Luu, H., Léger, P., & Tremblay, R. (2014). Seismic demand of moderately ductile reinforced concrete shear walls subjected to high-frequency ground motions. *Canadian journal of civil engineering*, *41*(2), 125-135.

Massone, L. M., & Wallace, J. W. (2004). Load-deformation responses of slender reinforced concrete walls. *Structural Journal*, *101*(1), 103-113.

Mitchell, D., Tremblay, R., Karacabeyli, E., Paultre, P., Saatcioglu, M., & Anderson, D. L. (2003). Seismic force modification factors for the proposed 2005 edition of the National Building Code of Canada. *Canadian Journal of Civil Engineering*, *30*(2), 308-327.

Mitchell, D., Paultre, P., Tinawi, R., Saatcioglu, M., Tremblay, R., Elwood, K., ... & DeVall, R. (2010). Evolution of seismic design provisions in the National building code of Canada. *Canadian Journal of Civil Engineering*, *37*(9), 1157-1170.

NBCC (2015): National Research Council of Canada (2015). *National Building Code of Canada.*

Oh, Y. H., Han, S. W., & Lee, L. H. (2002). Effect of boundary element details on the seismic deformation capacity of structural walls. *Earthquake engineering &*

structural dynamics, *31*(8), 1583-1602.

Orakcal, K., Wallace, J. W., & Conte, J. P. (2004). Flexural modeling of reinforced concrete walls-model attributes. *Structural Journal*, *101*(5), 688-698.

Orakcal, K., & Wallace, J. W. (2006). Flexural modeling of reinforced concrete walls-experimental verification. *ACI Materials Journal*, *103*(2), 196.

Paulay, T., & Uzumeri, S. M. (1975). A critical review of the seismic design provisions for ductile shear walls of the Canadian code and commentary. *Canadian Journal of Civil Engineering*, *2*(4), 592-601.

Paulay, T., & Priestley, M. N. (1992). *Seismic design of reinforced concrete and masonry buildings* (Vol. 768). New York: Wiley.

Paulay, T. (2001). Seismic response of structural walls: recent developments. *Canadian Journal of Civil Engineering*, *28*(6), 922-937.

Preti, M., & Giuriani, E. (2011). Ductility of a structural wall with spread rebars tested in full scale. *Journal of Earthquake Engineering*, *15*(8), 1238-1259.

Priestley, M. J. N., Calvi, G.M., & Kowalsky, M. J., (2007). *Displacement-based seismic design of structures.* Pavia, Italy: IUSS Press, Pavia, Italy.

Shedid, M. T., & El-Dakhakhni, W. W. (2014). Plastic hinge model and displacement-based seismic design parameter quantifications for reinforced concrete block structural walls. *Journal of Structural Engineering*, *140*(4), 04013090.

Standards New Zealand (NZS 3101).(2006). *Concrete Structures Standard*. NZS 3101-06, Wellington, New Zealand.

Sittipunt, C., Wood, S. L., Lukkunaprasit, P., & Pattararattanakul, P. (2001). Cyclic

behavior of reinforced concrete structural walls with diagonal web reinforcement. *Structural Journal*, *98*(4), 554-562.

Thomsen IV, J. H., & Wallace, J. W. (1995). *Displacement-based design of RC structural walls: experimental studies of walls with rectangular and T-shaped cross sections* (Vol. 6). Report No. CU/CEE-95.

Thomsen IV, J. H., & Wallace, J. W. (2004). Displacement-based design of slender reinforced concrete structural walls—experimental verification. *Journal of structural engineering*, *130*(4), 618-630.

Wallace, J. W., Massone, L. M., Bonelli, P., Dragovich, J., Lagos, R., Lüders, C., & Moehle, J. (2012). Damage and implications for seismic design of RC structural wall buildings. *Earthquake Spectra*, *28*(1_suppl1), 281-299.

White, T. W. (2004). *Seismic demand in high-rise concrete walls* (Doctoral dissertation, University of British Columbia).

Zhang, Y., & Wang, Z. (2000). Seismic behavior of reinforced concrete shear walls subjected to high axial loading. *Structural Journal*, *97*(5), 739-750.

2.8 TABLES

Table 2.1: Test matrix

Specimen	Configuration	Wall Dimensions	Vertical Reinforcements		Horizontal Reinforcements		Axial stress (MPa)	Axial ($\% f_c'$)
			Number of bars and bar sizes	ρ_v (%)	D4 at spacing (mm)	ρ_h (%)		
W1	Rectangular	1,802mm × 3,990mm length×height	42 D7	1.17	2 at 90	0.64	1.09	3.85
W2	Flanged		16 D7 & 22 D4	0.66	2 at 110	0.53	0.89	3.15
W3	Boundary Elements		20 D7 & 18 D4	0.69	2 at 110	0.53	0.89	3.15
W4	Rectangular		64 D11	2.80	2 at 45	1.28	1.09	2.66
W5	Flanged		16 D11 & 44 D7	1.58	2 at 55	1.05	0.89	2.17
W6	Boundary Elements		20 D11 & 40 D7	1.63	2 at 55	1.05	0.89	2.17

Table 2.2: Materials (a) Concrete strengths (b) Reinforcements

Concrete	Compressive Strength (MPa)	*C.O.V. (%)*	Standard
Walls ***W1*** and ***W2***	28.3	*5.5%*	Cylinder Test ASTM C39-10
Wall ***W3***	36.4	*3.4%*	Cylinder Test ASTM C39-10
Phase II Walls	41.0	*7.3%*	Cylinder Test ASTM C39-10

(a)

Reinforcement	Area (mm^2)	Yield Strength (MPa)	*C.O.V. (%)*	Elongation (%)	Standard
D4	26	510	*3.5*	8.0	ASTM A615-09
D7	45	480	*2.8*	10.7	ASTM A615-09
D11	71	420	*6.9*	9.4	ASTM A615-09

(b)

Table 2.3: Summary of predicted and measured strengths

Specimen	Configuration		Yield Strength Q_y					Maximum Capacity Q_u				
			Predicted (kN)	Measured (kN)		Difference (%)		Predicted (kN)	Measured (kN)		Difference (%)	
				Push (+ve)	Pull (-ve)	Push (+ve)	Pull (-ve)		Push (+ve)	Pull (-ve)	Push (+ve)	Pull (-ve)
W1	Rectangular	*Phase I*	136	152	123	11	11	193	230	172	16	12
W2	Flanged		136	175	158	22	14	177	187	183	5	3
W3	Boundary Elements		135	161	160	16	16	178	176	177	1	1
W4	Rectangular	*Phase II*	233	222	195	5	19	351	336	355	4	1
W5	Flanged		218	220	270	1	19	330	322	313	2	5
W6	Boundary Elements		213	227	209	6	2	332	334	313	1	6

Table 2.4: Summary of experimental damage levels and the occurrence of the damage states after the stated loading cycle

Walls	Configuration		Experimental Damage Levels Determined at the stated displacement level cycle* and %drift						Damage States according to the Applied Technological Council (ATC P58, 2012) determined after the stated displacement level cycle			
			Concrete Spalling		Concrete Crushing		Reinforcement Fracture Started		*DS1*	*DS2*	*DS3*	*DS4*
			Loading Cycle	*Drift (%)*	Loading Cycle	*Drift (%)*	Loading Cycle	*Drift (%)*				
W1	Rectangular	***Phase I***	*$3\Delta_y$*	*0.57*	*$4\Delta_y$*	0.84	*$4\Delta_y$ (2^{nd} Cycle)*	*0.84*	*$2\Delta_y$*	*$4\Delta_y$*	*$5\Delta_y$*	*$6\Delta_y$*
W2	Flanged		*$3.5\ \Delta_y$*	*0.75*	*$4.6\Delta_y$*	*1.00*	*$4.6\Delta_y$*	*1.00*	*$2.3\Delta_y$*	*$3.5\Delta_y$*	*$4.6\Delta_y$*	*$5.8\Delta_y$*
W3	Boundary Elements		*$3\Delta_y$*	*0.63*	*$4\Delta_y$*	*0.84*	*$4\Delta_y$ (2^{nd} Cycle)*	*0.84*	*$3\Delta_y$*	*$4\Delta_y$*	*$5\Delta_y$*	*$6\Delta_y$*
W4	Rectangular	***Phase II***	*$3\Delta_y$ (2^{nd} Cycle)*	*0.84*	*$4\Delta_y$*	*1.13*	*$4\Delta_y$ (2^{nd} Cycle)*	*1.13*	*$3\Delta_y$*	*$4\Delta_y$*		*$4\Delta_y$ (2^{nd} Cycle)*
W5	Flanged		*$2.6\Delta_y$*	*0.84*	*$3.7\Delta_y$*	*0.85*	*$5.1\Delta_y$*	*1.30*	*$2.6\Delta_y$*	*$3.7\Delta_y$*	*$6.4\Delta_y$*	*$8\Delta_y$*
W6	Boundary Elements		*$4\Delta_y$*	*1.05*	*$5\Delta_y$*	*1.32*	*$6\Delta_y$*	*1.58*	*$3\Delta_y$*	*$4\Delta_y$*	*$6\Delta_y$*	*$7\Delta_y$*

*****Damage occurred at the first displacement level cycle unless noted*

Table 2.5: Yield displacement, ultimate displacement, displacement ductility, and idealized displacement ductility

				At first yield		At Maximum Load				At 20% strength degradation			
Wall	Configuration		Direction	Δ_y (mm)	*% Drift*	Δ_u (mm)	μ_Δ	*% Drift*	$\mu_{\Delta u}^{id}$	$\Delta_{0.8u}$ (mm)	$\mu_{\Delta 0.8u}$	*% Drift*	$\mu_{\Delta 0.8u}^{id}$
W1	Rectangular	***Phase I***	+(ve)	8.3	0.21	22.7	2.7	0.57	1.8	36.6	4.4	0.92	2.9
			-(ve)			17.1	2.1	0.43	1.5	34.5	4.2	0.86	3.0
W2	Flanged		+(ve)	8.7	0.22	20.3	2.4	0.51	2.2	27.8	3.2	0.70	3.0
			-(ve)			19.1	2.2	0.48	1.9	37.8	4.4	0.95	3.8
W3	Boundary Elements		+(ve)	8.3	0.21	16.8	2.0	0.42	1.8	39.3	4.7	0.98	4.3
			-(ve)			17.1	2.1	0.43	1.9	35.2	4.2	0.88	3.8
W4	Rectangular	***Phase II***	+(ve)	10.9	0.27	28.6	2.6	0.72	1.7	45.9	4.2	1.15	2.8
			-(ve)			34.4	3.2	0.86	1.8	48.4	4.4	1.21	2.4
W5	Flanged		+(ve)	9.1	0.23	-	-	-	-	-	-	-	-
			-(ve)			33.8	3.7	0.85	3.2	52	5.7	1.30	4.9
W6	Boundary Elements		+(ve)	10.5	0.26	31.5	3.0	0.79	2.0	63.0	6.0	1.58	4.1
			-(ve)			31.5	3.0	0.79	2.0	62.7	6.0	1.57	4.0

2.9 FIGURES

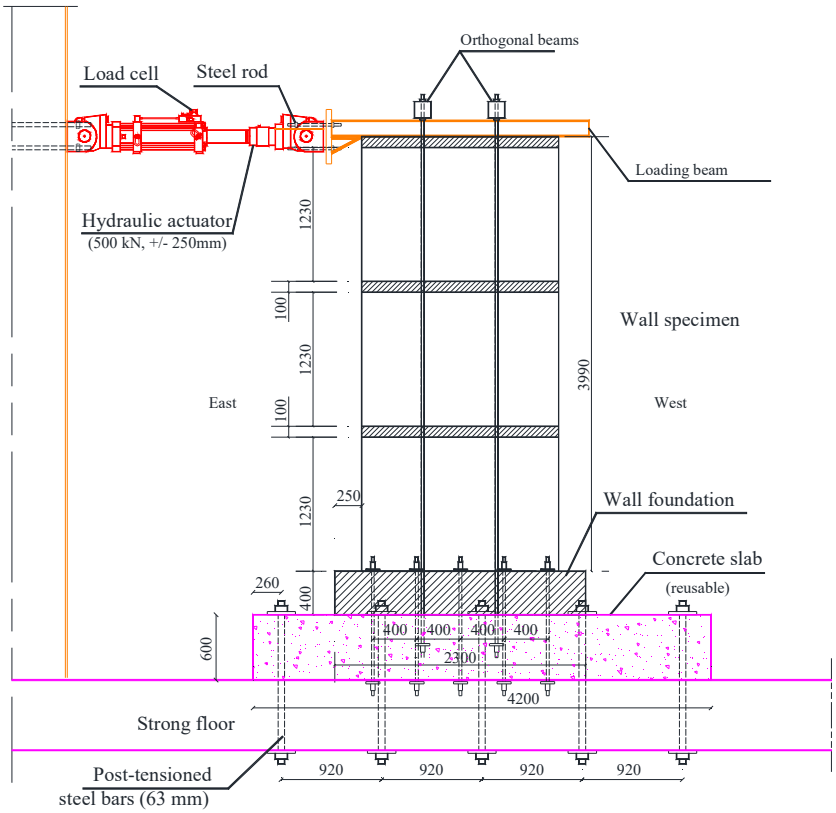

(a)

(b)

Figure 2.1: (a) Test setup: face view; (b) Test setup: side view

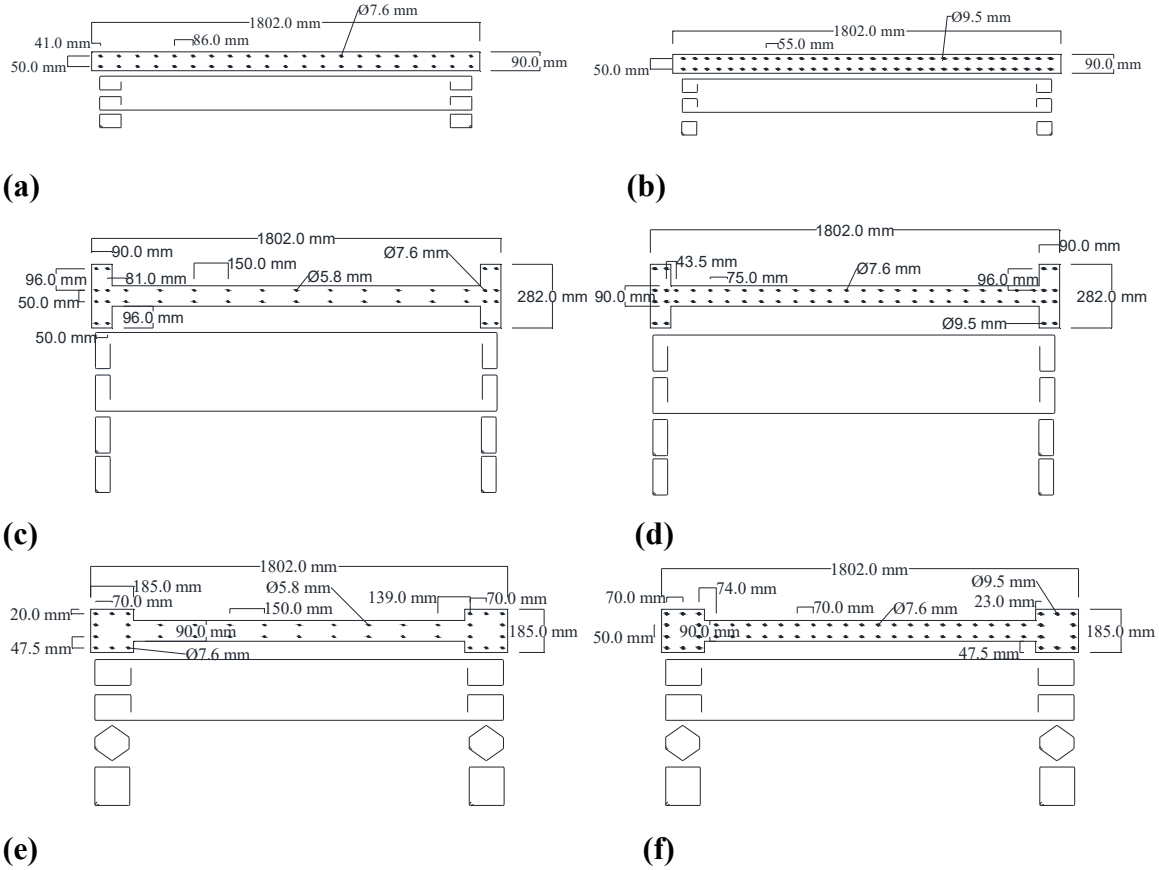

Figure 2.2: Specimen configurations; Rectangular walls (a) *W1* & (b) *W4*; Flanged walls (c) *W2* & (d) *W5*; Boundary Elements walls (e) *W3* & (f) *W6*

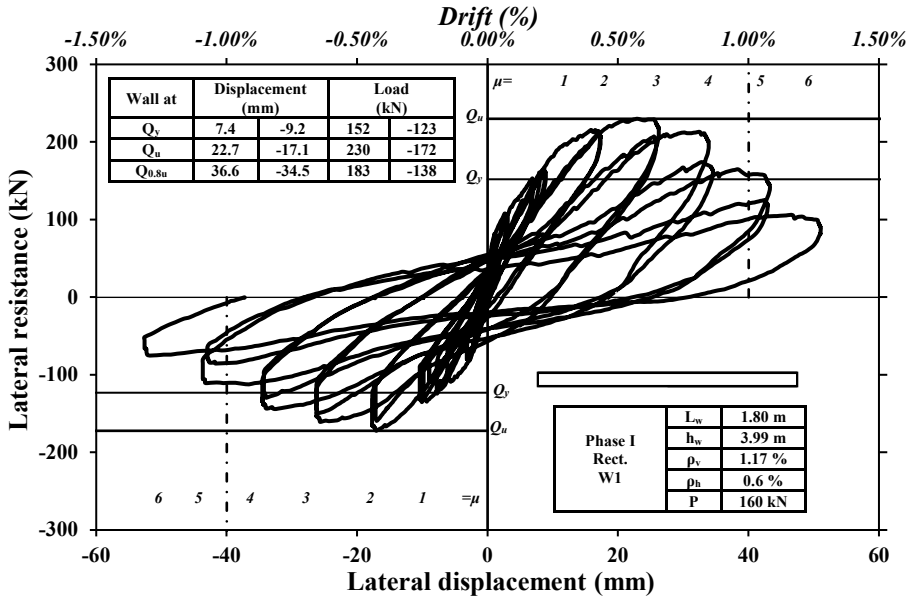
Drift (%)
-1.50%
-1.00%
-0.50%
0.00%
0.50%
1.00%
1.50%
Lateral resistance (kN)
Lateral displacement (mm)
μ= 1 2 3 4 5 6
6 5 4 3 2 1 =μ
Qu
Qy
Wall at | Displacement (mm) | | Load (kN) | |
Qy | 7.4 | -9.2 | 152 | -123
Qu | 22.7 | -17.1 | 230 | -172
Q0.8u | 36.6 | -34.5 | 183 | -138
Phase I Rect. W1
Lw 1.80 m
hw 3.99 m
ρv 1.17 %
ρh 0.6 %
P 160 kN

(a)

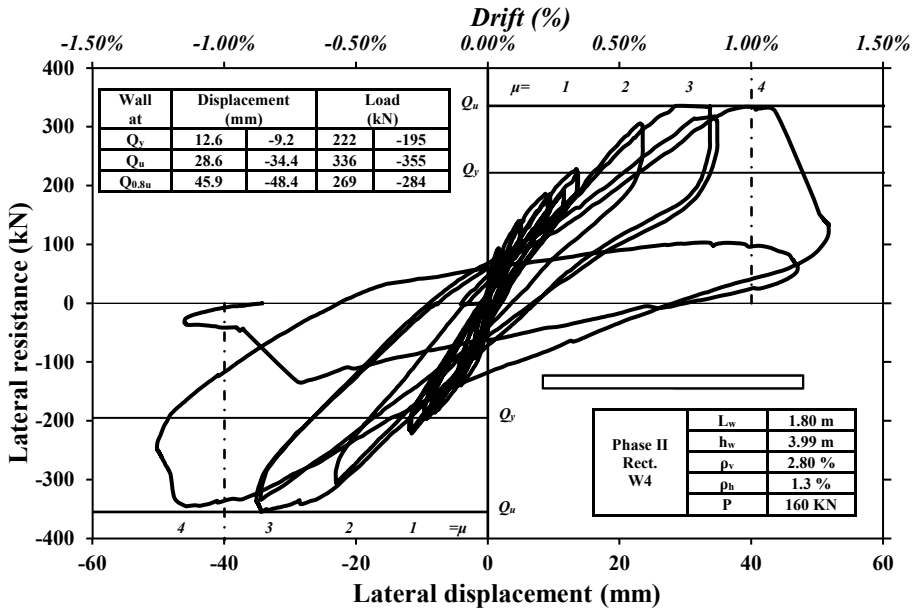
Drift (%)
-1.50%
-1.00%
-0.50%
0.00%
0.50%
1.00%
1.50%
Lateral resistance (kN)
Lateral displacement (mm)
μ= 1 2 3 4
4 3 2 1 =μ
Qu
Qy
Wall at | Displacement (mm) | | Load (kN) | |
Qy | 12.6 | -9.2 | 222 | -195
Qu | 28.6 | -34.4 | 336 | -355
Q0.8u | 45.9 | -48.4 | 269 | -284
Phase II Rect. W4
Lw 1.80 m
hw 3.99 m
ρv 2.80 %
ρh 1.3 %
P 160 KN

(b)

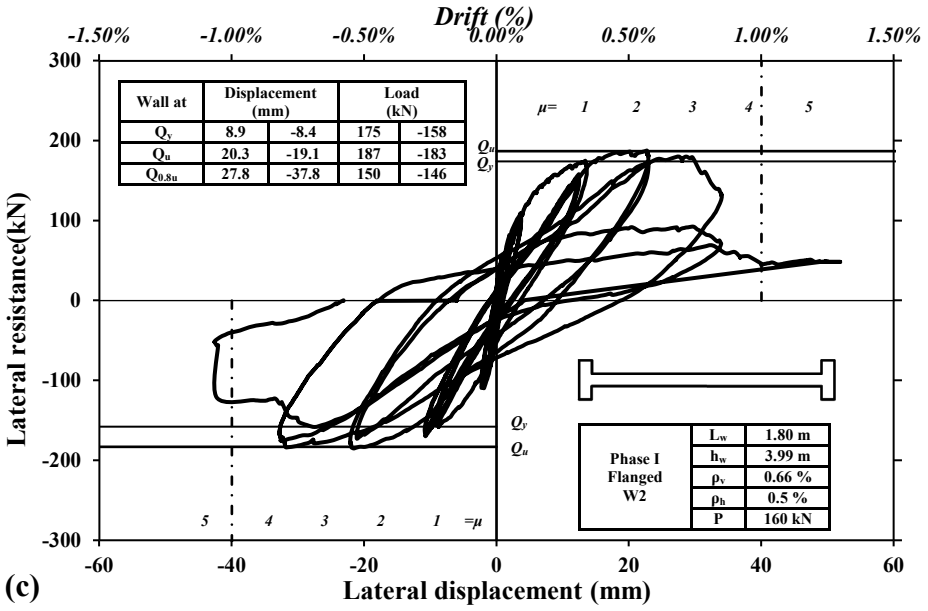
Drift (%)
-1.50% -1.00% -0.50% 0.00% 0.50% 1.00% 1.50%
Lateral resistance(kN)
Lateral displacement (mm)
Wall at | Displacement (mm) | | Load (kN) | |
Qy | 8.9 | -8.4 | 175 | -158
Qu | 20.3 | -19.1 | 187 | -183
Q0.8u | 27.8 | -37.8 | 150 | -146
μ= 1 2 3 4 5
5 4 3 2 1 =μ
Qu
Qy
Phase I Flanged W2
Lw 1.80 m
hw 3.99 m
ρv 0.66 %
ρh 0.5 %
P 160 kN

(c)

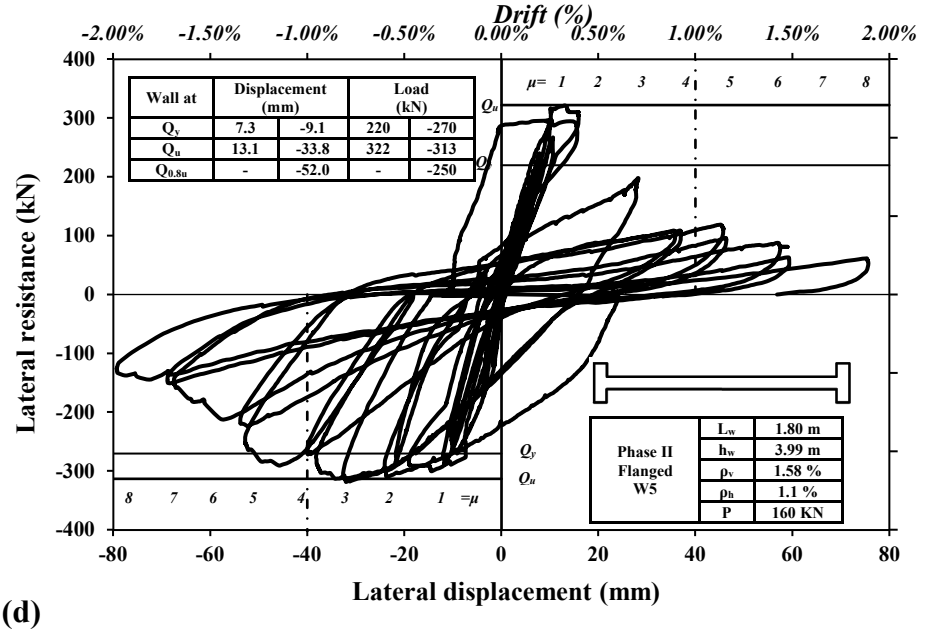
Drift (%)
-2.00% -1.50% -1.00% -0.50% 0.00% 0.50% 1.00% 1.50% 2.00%
Lateral resistance (kN)
Lateral displacement (mm)
Wall at | Displacement (mm) | | Load (kN) | |
Qy | 7.3 | -9.1 | 220 | -270
Qu | 13.1 | -33.8 | 322 | -313
Q0.8u | - | -52.0 | - | -250
μ= 1 2 3 4 5 6 7 8
8 7 6 5 4 3 2 1 =μ
Qu
Qy
Phase II Flanged W5
Lw 1.80 m
hw 3.99 m
ρv 1.58 %
ρh 1.1 %
P 160 KN

(d)

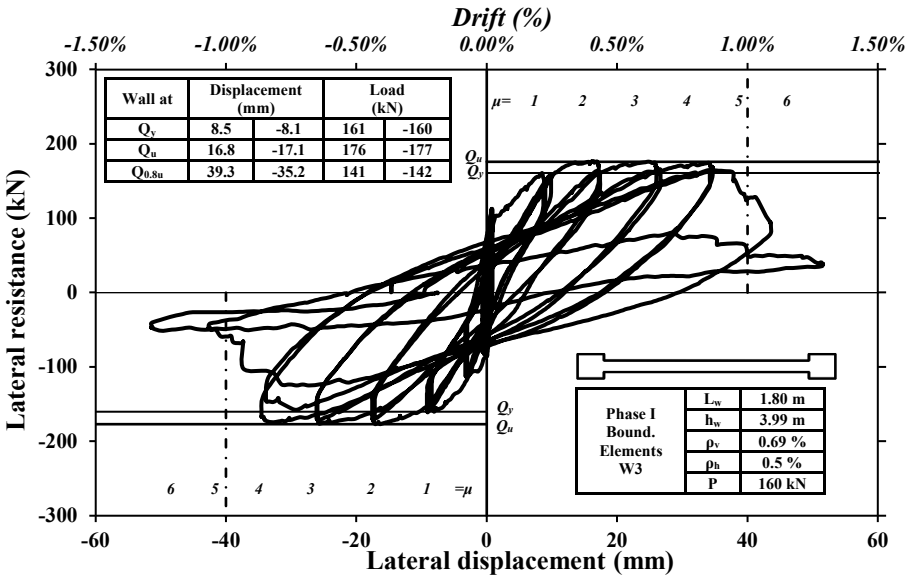

(e)

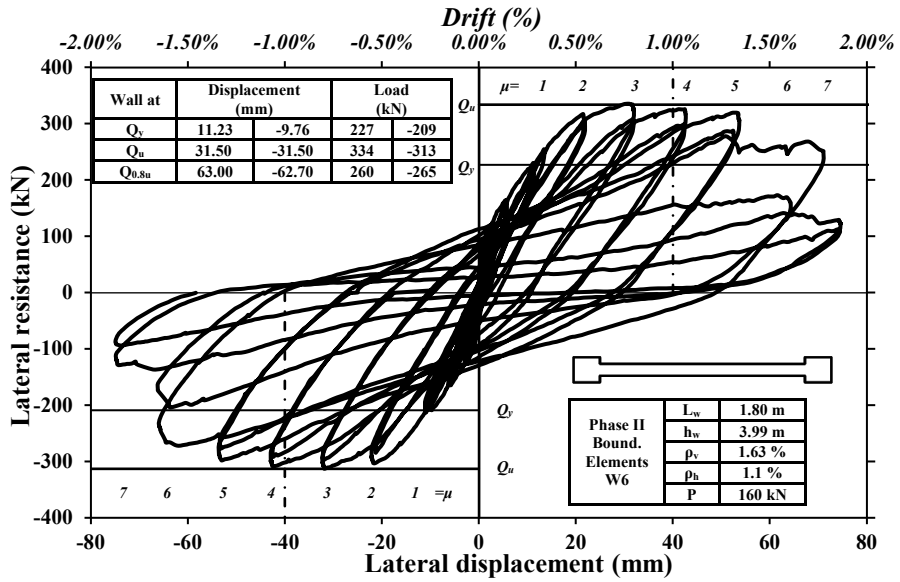

(f)

Figure 2.3: Load-displacement relationships; Rectangular walls (a) *W1* & (b) *W4*; Flanged walls (c) *W2* & (d) *W5*; Boundary Elements walls (e) *W3* & (f) *W6*

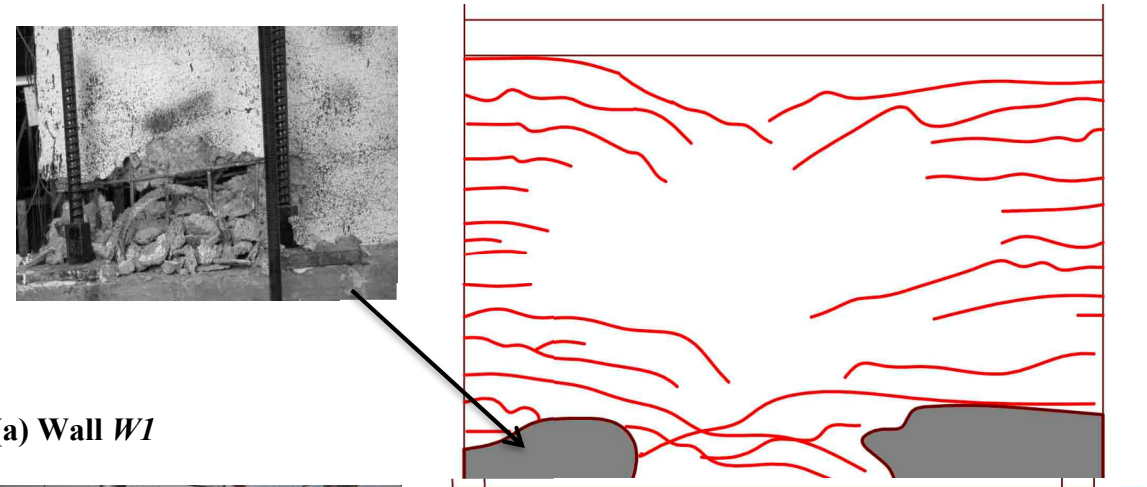

(a) Wall *W1*

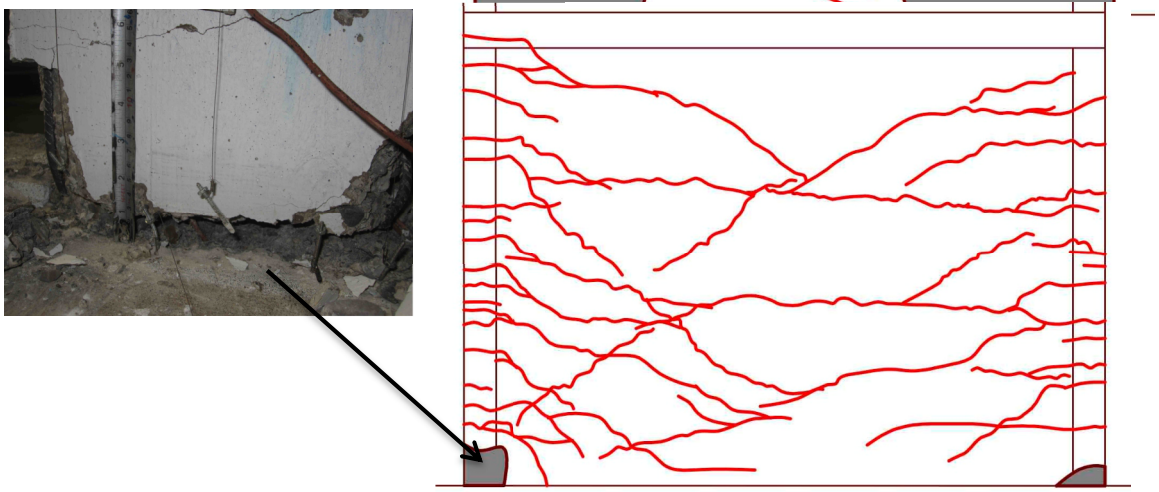

(b) Wall *W2*

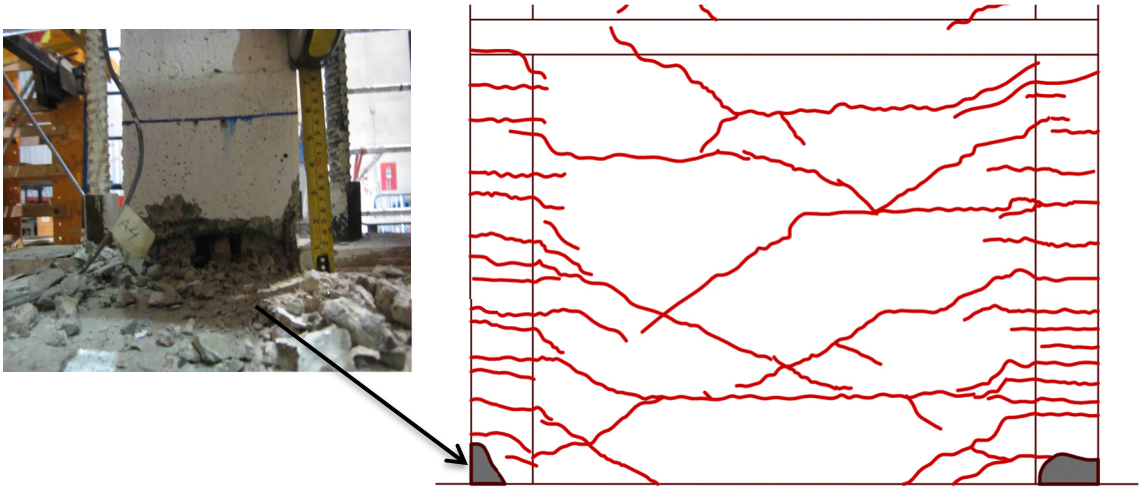

(c) Wall *W3*

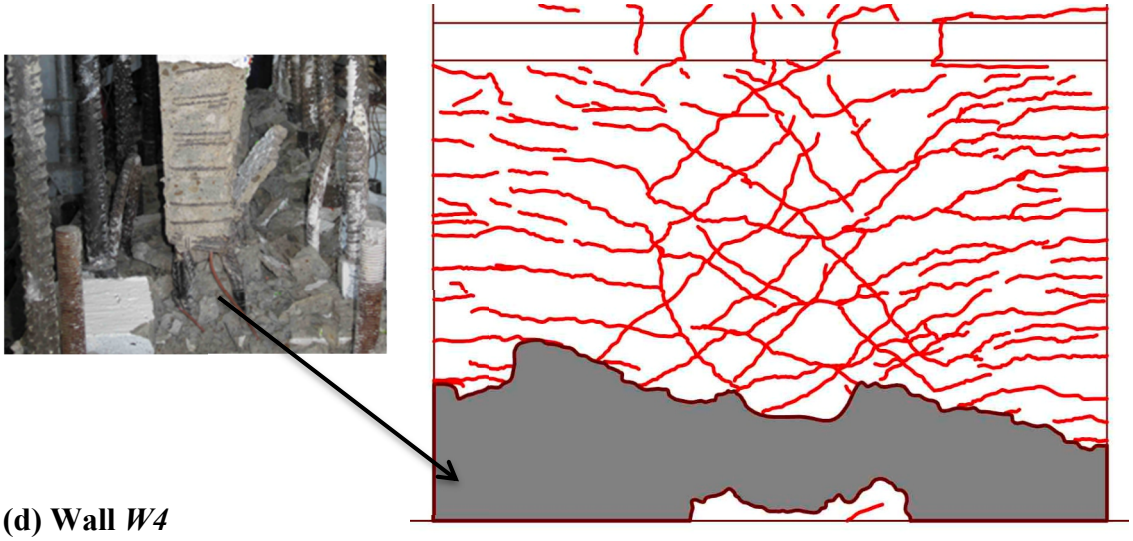

(d) Wall *W4*

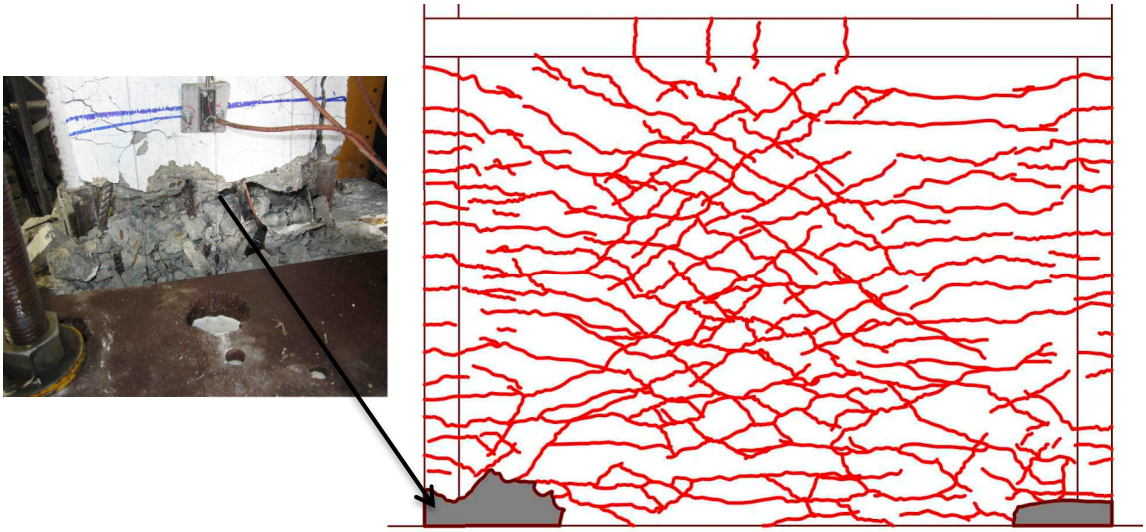

(e) Wall *W5*

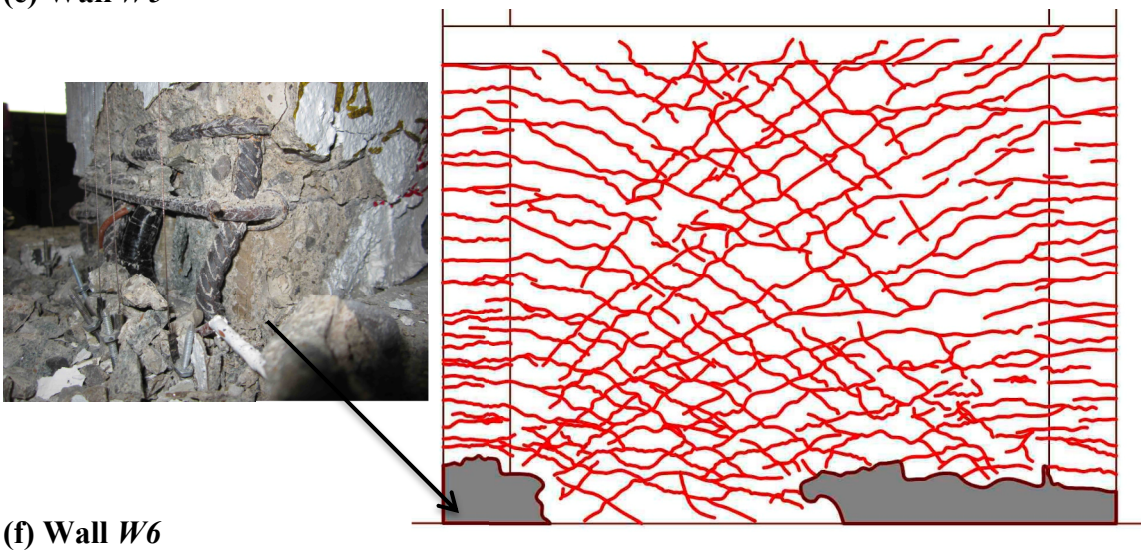

(f) Wall *W6*

Figure 2.4: First story crack patterns and toe damage at failure for each wall; (a) *W1*; (b) *W2*; (c) *W3*; (d) *W4*; (e) *W5*; (f) *W6*

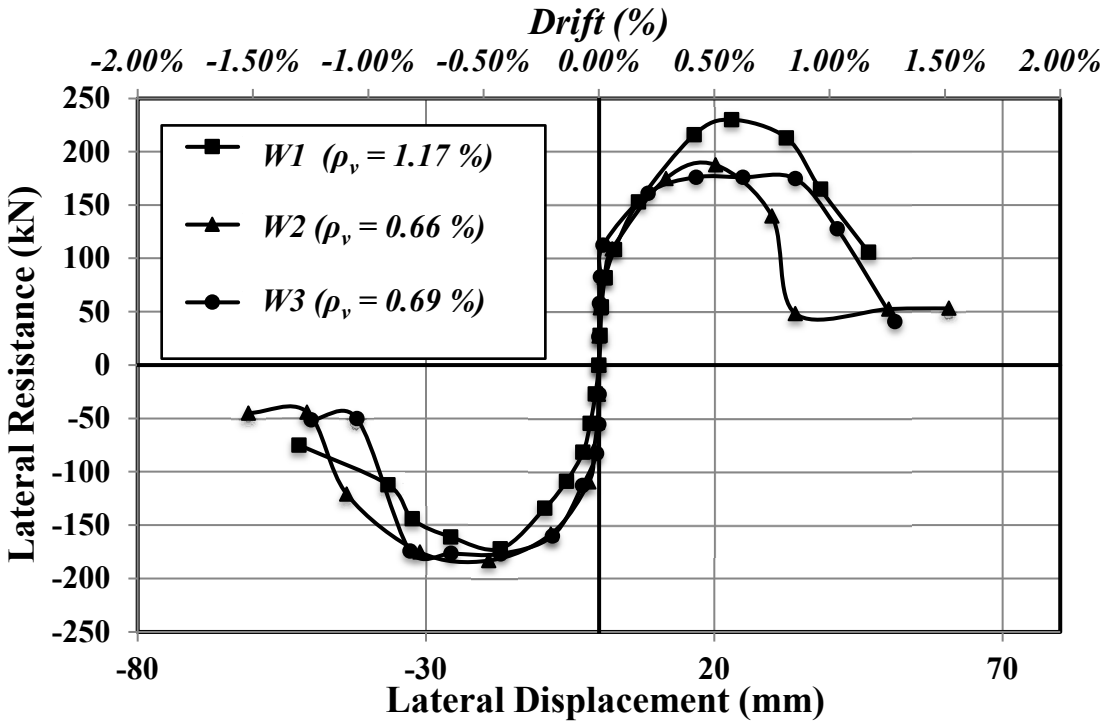

(a)

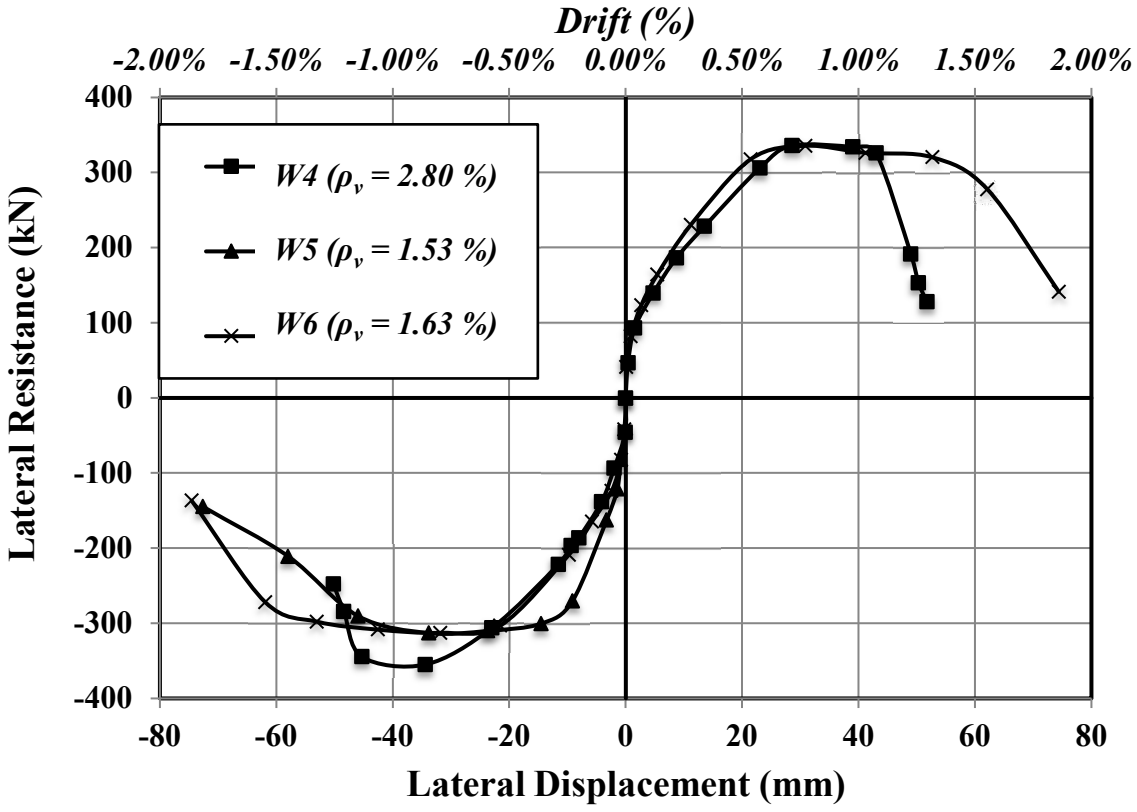

(b)

Figure 2.5: Load-displacement envelopes; (a) *Phase I*; (b) *Phase II*

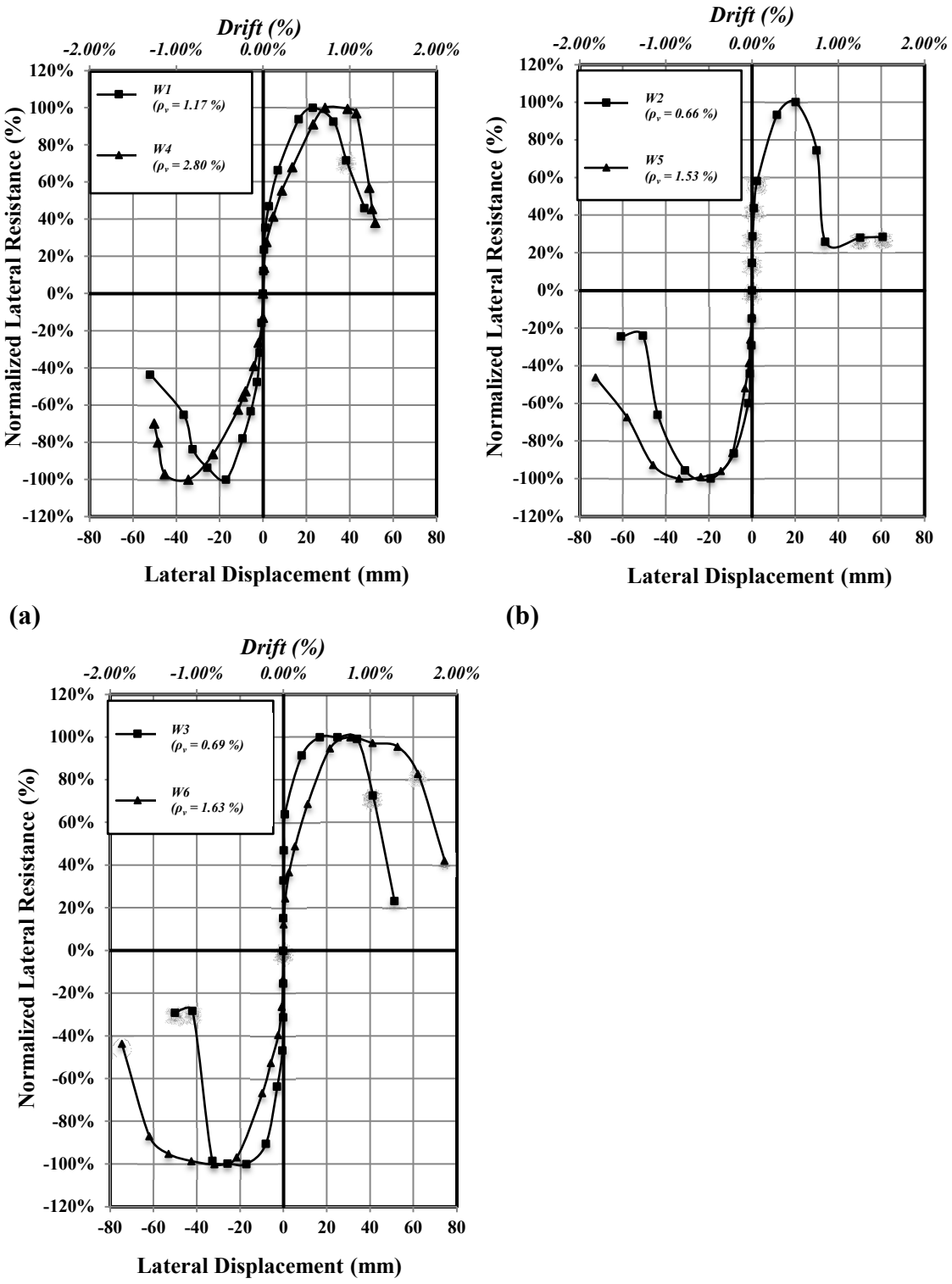

Figure 2.6: Normalized load-displacement relationships; (a) Rectangular walls *W1* & *W4*; (b) Flanged walls *W2* & *W5*; (c) Boundary Elements walls *W3* & *W6*

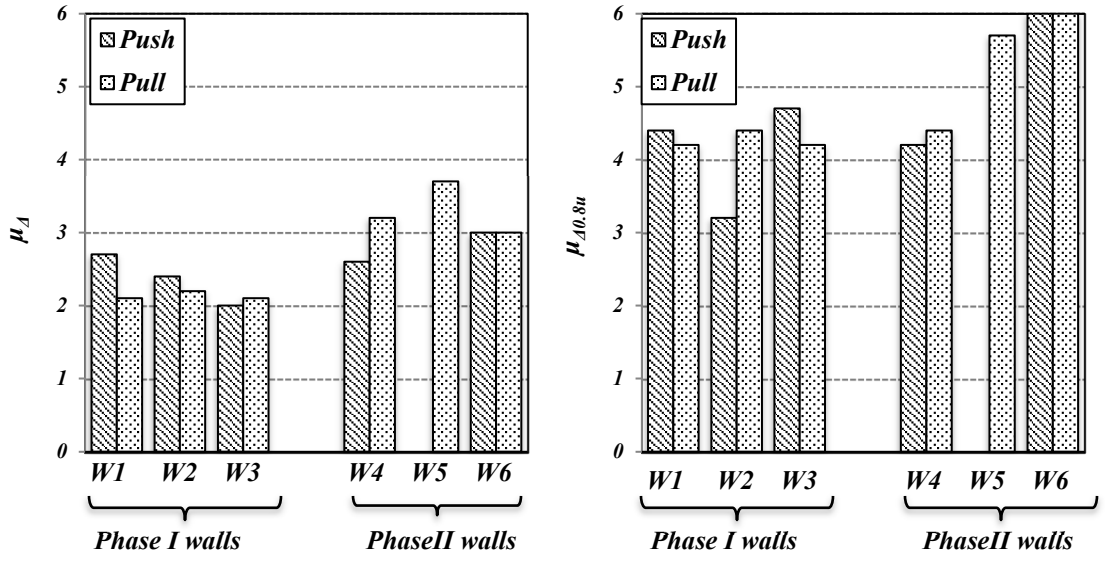

(a) **(b)**

Figure 2.7: Walls displacement ductility values: (a) At maximum capacity; (b) At the ultimate level

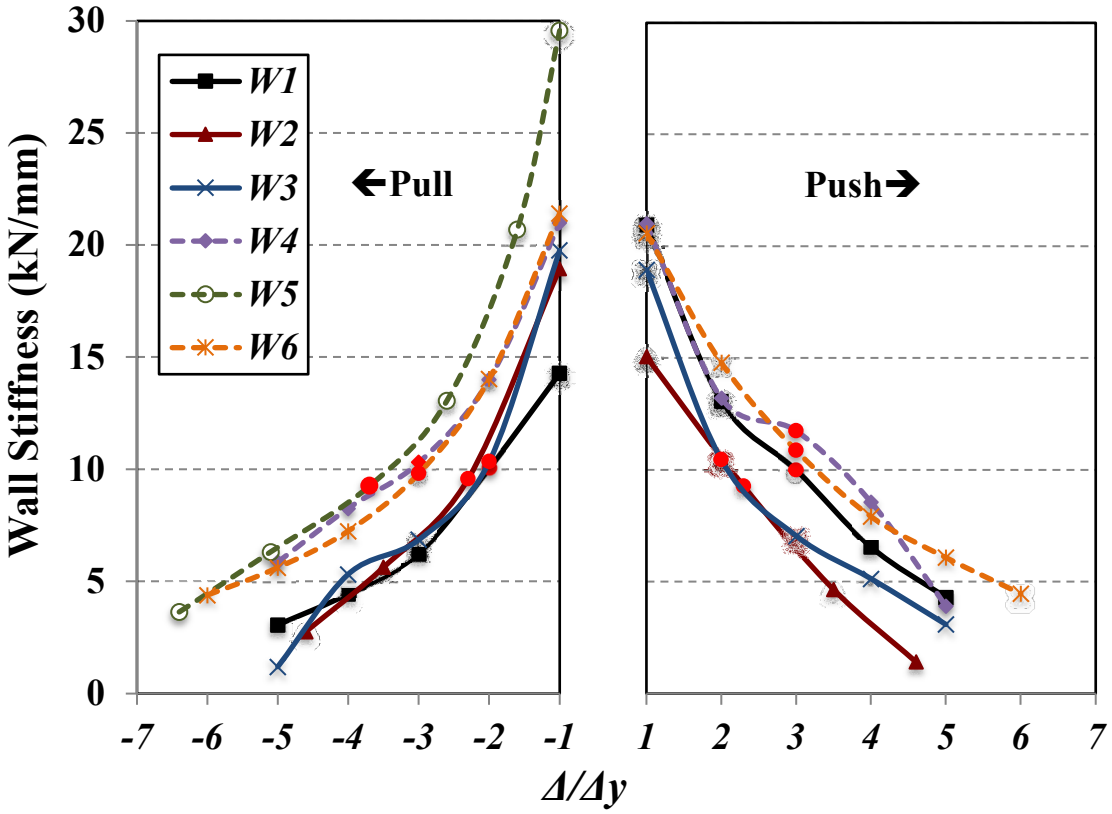

Figure 2.8: Stiffness degradation versus displacement levels Δ/Δ_y

CHAPTER 3
ANALYSIS OF REINFORCED CONCRETE SHEAR WALLS WITH DIFFERENT CONFIGURATIONS FOR SEISMIC DESIGN

3.1 ABSTRACT

The Canterbury earthquake royal commission report highlighted that well-detailed reinforced concrete (*RC*) shear walls did not achieve their anticipated ductility capacities. In response to enhance the performance of such walls during future seismic events, the report recommended the use of concentrated and confined rebars at the wall toes coupled with high reinforcement ratios within the wall to initiate secondary cracks and elongate the inelastic regions, thus minimizing the corresponding seismic demands. In this respect, the current study evaluates the seismic performance of *RC* walls with flanged and boundary element configurations compared to their rectangular counterparts, when different reinforcement ratios are adopted. Specifically, the study presents a detailed analysis of six three-story half-scaled *RC* structural walls tested under quasi-static cyclic loading to represent seismic demands. The six walls were originally tested in two phases, where each phase had three different wall types (i.e., rectangular, flanged, and boundary element configurations). Walls in both phases had the same overall dimension and cross-section area; however, *Phase II* walls had *2.4 times* the vertical reinforcement ratios used in *Phase I* walls. Following a summary of the experimental program and results, the current study presents the analysis results of the walls in terms of their load-strain relationships, curvature profiles, stiffness degradation trends, energy dissipation capacities, and equivalent viscous damping ratios. A comparison between the theoretical and experimental curvatures is also presented for the test walls at different drift levels. The results show that

flanged and boundary element walls had low yield curvatures and high ultimate curvatures which resulted in enhancing their displacement ductility capacities. Flanged and boundary element walls also exhibited higher stiffness degradation rates when compared to their rectangular counterparts, leading to reduced seismic demands. Moreover, Flanged and boundary element walls with high vertical reinforcement ratios (1.58%-1.63%) had also higher energy dissipation capacities than their counterparts with low vertical reinforcement ratios (0.66%-0.69%). However, rectangular walls with low vertical reinforcement ratios (1.17%) showed higher ultimate curvature capacities than rectangular walls with high vertical reinforcement ratios (2.80%). Overall, the results demonstrate that future editions of relevant design standards (e.g., CSA A23.3 and ACI 318) should consider assigning different seismic design parameters (e.g., ultimate compressive strains, equivalent viscous damping ratios, and ductility-related modification factors) for *RC* shear walls based on their end configurations that can significantly alter the performance of such walls under seismic events.

3.2 INTRODUCTION

In high seismic zones, it is not economical to design shear walls to respond elastically, and therefore, inelastic deformations would be anticipated to minimize seismic design demands on such walls. Inelastic deformations are directly related to the displacement ductility capacity of the wall—defined as the ability of the wall to deform beyond yielding with no or minor strength degradation. As such, walls capable of providing high ductility capacities could be assigned higher seismic force reduction factors when the force-based design

approach is adopted. Specifically, due to cracking and damage to the walls forming the lateral load-resisting system, the overall stiffness of the building would decrease, and subsequently, its fundamental period would increase, leading to a potential decrease in the seismic demands based on the characteristics of the design response spectrum. The quantification of the displacement ductility for structural components with an elastic-plastic behavior was well defined (Chopra 2000); however, for reinforced concrete (RC) walls with nonlinear behavior, several approaches were proposed in the literature (e.g., Park and Paulay 1975; Paulay and Priestly 1992; Priestley et al. 1996; Priestley 2000; Tomazevic 1999; Shedid et al. 2008) to develop equivalent elastic-perfectly-plastic systems in an effort to quantify the idealized displacement ductility capacities of *RC* shear walls for seismic design.

For *RC* shear walls with various design parameters (e.g., cross-section properties, aspect ratios, and axial load levels), cracking patterns, ductility and plastic hinging of walls, seismic collapse risk, contributions of flexural and shear deformations to total deflections, shear strength of walls, attained compressive and tensile strains, variations of curvature over wall heights, and decreases of effective wall stiffness, were all investigated by several researchers (e.g., Thomsen and Wallace 1995; Zhang et al. 2000; Massone and Wallace, 2004; Thomsen and Wallace 2004; Adebar 2007; Ghorbanirenani et al. 2012; Luu et al. 2014; Christidis and Trezos 2017; Rong et al. 2020; Gondia et al. 2020; Akl and Ezzeldin 2023). However, according to the Canterbury earthquake royal commission report (Canterbury Commission Report, 2011), well-detailed *RC* shear walls did not show the anticipated ductility due to the initiation of primary flexural cracks at the limited plastic

hinge locations. Such cracks increased in size and led to a concentration of plastic strains at their crack locations, which resulted in poor wall ductility capacities. It was explained that this undesirable performance was mainly due to insufficient vertical reinforcement ratios that were needed to initiate secondary cracks and elongate the plastic regions. Therefore, the report suggested to increase and concentrate the vertical reinforcement at the wall toes in order to increase the number of flexural cracks and better distribute the plastic strains over the height of the outermost bars, thus increasing the energy dissipation and ductility capacities of the walls when subjected to seismic events.

The main objective of the current study is to quantify the improved seismic performance of *RC* walls with flanged and boundary element configurations compared to their rectangular counterparts when different vertical reinforcement ratios are adopted. In this respect, detailed analyses of six half-scale *RC* shear walls are presented to investigate the mechanism discussed in the Canterbury earthquake commission report. Specifically, following a summary of the experimental program and test results, the current study initially evaluates the influence of using different end wall configurations (i.e., rectangular, flanged, boundary elements) and vertical reinforcement ratios (i.e., from 0.66% to 2.80%) on the concrete compressive strains, reinforcement tensile strains, and curvature profiles of the test walls. The experimental yield and ultimate curvatures of the walls along with their plastic hinge lengths are also presented and compared to their corresponding theoretical values. Then, the stiffness degradation trends, energy dissipation capacities, and equivalent viscous damping ratios of the walls are discussed. Finally, conclusions and

recommendations for future studies are presented to further enhance the seismic performance of *RC* shear walls.

3.3 SUMMARY OF THE EXPERIMENTAL PROGRAM AND RESULTS

Six *RC* half-scaled three-story shear walls were constructed and tested by El-Azizy et al. (2015). The walls were constructed in two phases, each phase had rectangular, flanged, and boundary element walls. For each pour, twelve concrete cylinders were prepared and tested under compression at 7, 14, and 28 days as well as on the testing day following ASTM C39-21 (ASTM 2021). The vertical reinforcement ratio, ρ_v, horizontal reinforcement ratio, ρ_h, configuration, axial stress, and the number of bars with their sizes are presented in Table 3.1. As can be seen in the table, all test walls had the same overall dimensions; however, *Phase I* walls (*W1*, *W2*, and *W3*) had lower vertical reinforcement ratios compared to their counterparts tested in *Phase II* (*W4*, *W5*, and *W6*). It is worth noting that the six walls were designed using such vertical reinforcement ratios to facilitate direct comparisons not only between *Phases I* and *II* walls as presented in the current study but also between such RC walls and other well-detailed reinforced concrete block walls tested by Shedid et al. (2010) as presented in El-Azizy et al. (2013). The walls were reinforced with scaled *D4*, *D7,* and *D11* bars with cross-sectional areas of $26mm^2$, $45mm^2$, and $71mm^2$, respectively. Such reduced-scale bars were equivalent to *M10*, *M15*, and *M20* ($100mm^2$, $200mm^2$, and $300mm^2$, respectively) full-scale bars conforming to *CSA G30.18-21* (CSA 2021). For each bar size, tension tests were performed on three 600mm coupons to determine their yield

strengths following ASTM A615-20 (ASTM 2020). Full details of the material properties (i.e., concrete and steel) pertaining to the six walls can be found in El-Azizy et al. (2015).

The six walls are classified as 'Ductile Walls' according to Clauses 21.2 and 21.5 of CSA A23.3-19 (CSA 2019), where: i) the end-regions of the walls were confined with buckling prevention ties; ii) the wall thicknesses exceeded the minimum values at their plastic hinge regions; and iii) the distributed and concentrated reinforcement ratios surpassed the minimum values in addition to anchoring the horizontal reinforcement of the walls. Therefore, all walls were designed considering the same ductility-related force modification factor, R_d, and overstrength-related factor, R_o, of 3.5 and 1.6, respectively, as per NBCC (2020). In addition, all walls were subjected to displacement-controlled fully-reversed cyclic loading protocols function of their respective yield displacements. Out-of-plane bracings were also provided to ensure in-plane loading, as shown in Figure 3.1(a). An axial load, P, of *160kN* was applied to all the walls via hydraulic actuators. As shown in Figure 3.1(b), for each wall, 38 vertical and horizontal displacement potentiometers were used to record the axial and lateral displacements as well as the relative sliding between the wall and the foundation. In addition, 14 strain gauges were attached to the outermost vertical bars of each wall to monitor the reinforcement strains throughout the loading history.

All the test walls failed in a ductile manner by crushing at the wall toes followed by the buckling of their outermost reinforcement bars. After that, such bars snapped and the tests were terminated when the lateral strength of the walls degraded to *50%* of their maximum strength. The results showed that *Phase II* walls had more flexural and shear

cracks relative to *Phase I* walls. In addition, in both phases, walls with flanged and boundary element configurations (*W2*, *W3*, *W5,* and *W6*) showed higher idealized displacement ductility capacities when compared to rectangular walls (*W1* and *W4*). The rectangular wall of *Phase I* (*W1*) showed also a higher idealized displacement ductility when compared to the rectangular wall of *Phase II (W4)*. However, flanged and boundary element walls of *Phase I* (*W2* and *W3*) showed lower ductility capacities when compared to their counterparts tested in *Phase II* (*W5* and *W6*) due to the concentration of plastic strains at the primary flexural cracks of the former walls. Full details about the experimental program including the test results can be found in El-Azizy et al. (2015).

3.4 Analysis of Test Results

This section presents the strains at *150 mm* and *300 mm* above the wall-foundation interface and the curvature profiles along the wall heights. Comparisons between the theoretical and experimental curvatures at different stages of loading (i.e., yield and ultimate) are also discussed. In addition, the outermost vertical reinforcement strains in tension and compression along with the stiffness degradation trends of the walls are presented. The section then shows the energy dissipation capabilities and the equivalent viscous damping ratios of the walls.

3.4.1 Wall End Strains

The vertically mounted displacement potentiometers on the wall were used to calculate the average strains over predetermined segments of the wall height, and subsequently, a strain profile along each side of the wall could be developed. The lateral loads versus the average compressive and tensile strains, calculated from the bottom two potentiometers on each end, are plotted for each wall, as shown in Figure 3.2. The potentiometers were located at *150 mm* and *300 mm* above the wall-foundation interface at all stages of loading till spalling of the wall toes occurred which resulted in the loss of fixation points of the potentiometers, thus their dismounting from the walls.

According to CSA A23.3-19 (CSA 2019), the maximum strain at the extreme concrete compression fibre shall be taken as 3.5×10^{-3}mm/mm. However, based on the analysis results presented in Figure 2, higher compressive strains over the bottom *150 mm* and *300 mm* at the maximum loads are achieved by most of the walls. For instance, such strains are 11.8×10^{-3} *mm/mm* and 5.7×10^{-3} *mm/mm*, respectively, for the rectangular wall *W1* in the push direction. The same strains are 2.0×10^{-3} *mm/mm* and 1.9×10^{-3} *mm/mm* for the flanged wall *W2* and are also 3.6×10^{-3} *mm/mm* and 2.3×10^{-3} *mm/mm* for the boundary element wall *W3*. Walls *W2* and *W3* had significantly lower strains than wall *W1* as the former walls did not show the expected performance due to their low vertical reinforcement ratios that resulted in the concentration of their plastic strains at the vicinity of the primary cracks and subsequently lower-than-expected recorded strain values. Regarding the rectangular wall *W4*, such strains are 12.4×10^{-3} *mm/mm* and 3.9×10^{-3} *mm/mm* at *150 mm* and *300 mm*, respectively, while the same strains are 14.5×10^{-3} *mm/mm* and 8.6×10^{-3}

mm/mm for the flanged wall *W5* and are also 7.4×10^{-3} *mm/mm* and 6.0×10^{-3} *mm/mm*, for the boundary element wall *W6*. It is also worth mentioning that due to a problem within the potentiometer mounted on wall *W6* at *150 mm*, the strain of this wall was lower than wall *W4*. For the wall tensile strains (i.e., calculated based on the potentiometers mounted vertically on both walls sides), the values at the maximum loads are almost similar for all the walls as the strains at *150 mm* and *300 mm* are on average 24.2×10^{-3} *mm/mm* and 13.8×10^{-3} *mm/mm*, respectively.

The maximum compressive concrete strain in *CSA A23.3-19* (CSA 2019) is conservative compared to the average compressive strain values presented in Figure 3.2. It is worth noting that such a difference would have a minimal effect on the design strength of under-reinforced sections but would significantly affect the theoretical curvatures and displacements at the maximum load. This means higher displacement levels due to higher curvatures, with minimal strength degradation, thus enhancing the ductility capacity of the seismic-resisting walls and subsequently increasing the performance-based design limits for *RC* shear walls.

3.4.2 Curvatures Profiles

3.4.2.1 Extent of Plasticity

The strain profiles calculated from the vertically mounted displacement potentiometers were used to compute the average curvatures along the wall height at different stages of loading, as shown in Figure 3.3. The figure shows that the curvatures over the first story height are significantly higher than those over the second and third stories. In the first story,

the curvature is significantly higher at the bottom third of the story when compared to the top two-thirds which shows a concentration of inelastic curvatures close to the base of the wall. It can be observed also that the curvatures in the second and the third stories tend to be in the elastic range and most of the inelastic deformations occur in the first story. Specifically, the plastic hinge length of each wall (i.e., determined when the experimental curvature of the wall exceeds its theoretical yield curvature) is within the first story with the exception of wall *W4*, where the plastic hinge length of this wall reaches the bottom *24%* of the second story height, as shown in Figure 3.3. In general, the figure shows that the plastic hinge lengths of the walls range from *45%* to *92%* of the wall length, L_w, which is slightly lower than the typical range of *50%-100%* L_w that was recommended in several previous related studies (e.g., Paulay and Priestley 1992). As can be seen also in Figure 3.3, the plastic hinge lengths of *Phase II* walls (*W4*, *W5,* and *W6*) are *36%*, *28%*, and *54%* larger than those of their *Phase I* counterparts (*W1*, *W2,* and *W3*), respectively. These results confirm the Canterbury earthquake commission report (Canterbury Report, 2011) as the former walls, with higher vertical reinforcement ratios, showed several secondary cracks during their tests that extended their inelastic deformations over the wall height, and thus, larger plastic hinge lengths relative to the latter walls with lower vertical reinforcement ratios.

3.4.2.2 Experimental Yield and Ultimate Curvatures

Table 3.2 presents the experimental yield and ultimate curvatures over the bottom *150 mm* for all the walls. As can be seen in the table, the experimental yield curvature, ϕ_y, of the walls varies between 1.27×10^{-3} to 2.01×10^{-3} *rad/m.* The ϕ_y values of *Phase II* walls are on

average 21% larger than those values of *Phase I* walls due to the higher vertical reinforcement ratios used in the former walls. In addition, for both phases, the table shows that the flanged and boundary element walls (*W2*, *W3*, *W5*, and *W6*) have lower ϕ_y values when compared to the rectangular walls (*W1* and *W4*) because the use of flanges or boundary elements in the former walls resulted in a reduced depth of the compression zone, which decreased the curvature values at yield, ϕ_y, relative to the latter walls.

As presented in Table 3.2, the experimental ultimate curvature at the maximum load, ϕ_u, of the walls varies between 6.71×10^{-3} to 14.84×10^{-3} *rad/m*. In *Phase II*, walls with flanges and boundary elements (*W5* and *W6*) have larger ϕ_u values than the rectangular wall (*W4*) by 121% and 78%, respectively. These experimental results demonstrate that flanged and boundary element configurations can enhance the ultimate curvature capacity of the wall, following the recommendations provided by the Canterbury earthquake commission report (Canterbury Report, 2011) that concentrating and confining the reinforcement ratios at the wall toes are expected to enhance the curvature capacities. Such enhancement was also attributed to the reduction in the depth of the compression zone (i.e., neutral axis depth), associated with using flanges and boundary elements, which subsequently increased the ultimate curvatures of the latter type of walls relative to their rectangular counterparts. Similar results were expected by *Phase I* walls; however, due to the concentration of primary cracks in the flanged and boundary element walls (*W2* and *W3*) because of their low vertical reinforcement ratios (El-Azizy et al. 2015), the ϕ_u of wall *W1* with a rectangular cross-section is higher by *38%* and *42%*, than walls *W2* and *W3*, respectively, as presented in Table 3.2. This finding supports the observed outcomes by the

Canterbury Report (Canterbury Report, 2011) that well-detailed *RC* shear walls did not show the expected seismic performance due to their low vertical reinforcement ratios.

As also presented in Table 3.2, the ϕ_u value of the rectangular wall in *Phase I* (*W1*) is higher than its counterpart in *Phase II* (*W4*) by *49%* due to the higher vertical reinforcement ratio of wall *W4* (*2.80%*) relative to wall *W1* (*1.17%*). While boundary element and flanged walls in *Phase II* (*W5* and *W6*) have higher ϕ_u values than their counterparts in *Phase I* (*W3* and *W4*) by *104%* and *69%,* respectively. This latter observation was not expected as flanged and boundary element walls in *Phase II* were heavily reinforced compared to those in *Phase I* and should have lower ultimate curvature values. However, these experimental curvature results are due to the concentration of the inelastic strains and deformations around a single large crack that occurred in each of the flanged and boundary element walls in *Phase I* (*W2* and *W3*), as discussed earlier. This was not observed for the rectangular walls (*W1* and *W4*) as the lower amount of reinforcement in wall *W1* tested in *Phase I* is high enough to result in acceptable distribution of cracks close to the base of the wall. Conversely, for walls *W2* and *W3* tested in *Phase I*, the amount of reinforcement is extremely low following the design criterion that the test walls have to reach the same ultimate lateral strength.

3.4.2.3 Comparison with Theoretical Curvatures

The theoretical curvatures are compared to the experimental average curvatures calculated at *150 mm* above the wall-foundation interface, as presented in Table 3.2. For each wall, the curvatures are calculated at both the onset of yielding of the outermost tensile vertical reinforcement bar and the maximum load. Curvature predictions are based on the beam

theory as required by *CSA A23.3-19* (CSA 2019). Specifically, the theoretical yield curvatures, ϕ_{yth}, are determined assuming i) plane sections remain plane after bending; and ii) compressive and tensile strains are in the elastic stage. As such, the linear portion of the concrete compressive stress-strain relationship is used to determine the yield curvature, while the equivalent stress block is used to calculate the theoretical ultimate curvature, ϕ_{uth}, for each wall.

As can be seen in Table 3.2, the ϕ_{yth} values of the rectangular walls in both phases (*W1* and *W4*) are in close agreement with their corresponding ϕ_y values, where the variation between the two curvature values is only 7% and 1% for both walls, respectively. Similarly, the ϕ_y values of the flanged and boundary element walls in *Phase II* (*W5* and *W6*) are closely overestimated by only *5%* and *6%*, respectively. However, the ϕ_{yth} values overestimate the ϕ_y values of *Phase I* walls with flanges and boundary elements (*W2* and *W3*) by *35%* and *22%*, respectively. Overall, the theoretical, ϕ_{yth}, and experimental, ϕ_y, yield curvatures are in good agreement with exception of the flanged and boundary element walls in *Phase I* (*W2* and *W3*) because of their unexpected performance due to their low vertical reinforcement ratios, as discussed earlier.

As also presented in Table 3.2, for wall *W1* and all *Phase II* walls, the experimental ultimate curvature, ϕ_u, is underestimated by the theoretical ultimate curvature, ϕ_{uth}, with variations up to only *17%* between the two curvature values. Such variations could be justified as the theoretical calculation of the ultimate curvature is at the wall-foundation interface, while the experimental ultimate curvature is calculated based on the average value over the bottom *150 mm* of the wall. However, as presented in Table 3.2, there are

significant variations between the experimental and theoretical ultimate curvature values of walls *W2* and *W3* because the inelastic strains of such walls were concentrated at a very limited height above the wall-foundation interface due to their low vertical reinforcement ratios. Specifically, during the tests, the inelastic strains of the two walls were observed to occur only in the vicinity of the primary flexural cracks, which resulted in the early snapping of the outermost rebars and subsequent concrete crushing at the wall toes which degraded the capacity of the walls at the early stages of loading (El-Azizy et al. 2015), leading to lower-than-expected ultimate curvatures. Conversely, by increasing the vertical reinforcement ratios in their *Phase II* counterparts (walls *W5* and *W6*), secondary cracks were initiated, resulting in better distribution of inelastic strains over multiples cracks, leading to higher ultimate curvatures and better agreement with the theoretically calculated curvatures, as presented in Table 3.2.

3.4.3 Reinforcement Strains

The outermost vertical reinforcement strains were measured at different elevations for each wall, as shown in Figure 3.4. The strain gauges were attached to the outermost vertical reinforcement bars at the following locations; wall-foundation interface, *50 mm* above the interface, *100 mm* above the interface, a height of half the wall length ($l_w/2 = 900\ mm$), and a height of the wall length ($l_w = 1800\ mm$). Figure 3.4 shows the reinforcement strains in compression and tension at different loading levels.

The tensile strains are typically expected to be with the highest values at the wall-foundation interface and then eventually yield and deform plastically. The strains are also

expected to become lesser at larger distances above the wall-foundation interface. As the displacement demands increase, the plastic strains are expected to extend vertically. This is not experimentally always the case (see Figure 3.4), where larger tensile strains at higher locations on the bars could be recorded as a result of different flexural cracking patterns. Specifically, when a wide flexural cracking occurs at the strain gauge location, the strain gauge measures the plastic strains over the vicinity of the crack. Nonetheless, all the walls have the highest strains either at the wall-foundation interface or up to *100 mm* above the interface, as shown in Figure 3.4.

3.4.4 Stiffness Degradation

The variation in the secant stiffness, K_e, defined as the ratio between the lateral resistance of the wall and its corresponding top displacement, is an important parameter when either force-based or displacement-based seismic design approaches are adopted. The secant stiffness of each wall is normalized in the current study by its theoretical gross stiffness to facilitate direct comparison between the walls due to their different concrete compressive strengths as well as their different end configurations. The theoretical gross stiffness is calculated based on the flexural and shear deformations of the wall using Eq. 3.1 (Priestley, et. al 2007):

$$K_i = 1/(\frac{h^3}{3E_cI_g} + \frac{kh}{G_cA}) \quad (3.1)$$

where h is the overall height of the wall; E_c is the young's modulus of concrete taken as $4500\sqrt{f_c'}$ (CSA A23.3-19); G_c is the shear modulus of concrete taken as $0.4E_c$ (CSA

A23.3-19); *k is* the shear shape factor taken as 1.2 (CSA A23.3-19); I_g is the gross second moment of inertia; and *A* is the wall cross-sectional area.

For all the walls, the variation in the normalized stiffness versus the lateral top drift is presented in Figure 3.5. As can be seen in the figure, all walls have a similar trend as the stiffness is reduced rapidly at low drift ratios and then the stiffness degradation becomes lower at higher drift ratios. Regarding *Phase I* walls, the normalized stiffness values of walls *W2* and *W3* are below *30%* of their initial stiffness values at a drift ratio of *0.20%.* A similar drop is observed for wall *W1* at a later stage of loading of *0.40%* drift. The same trend is also observed in *Phase II* walls, as shown in Figure 3.5. Specifically, the normalized stiffness values of walls *W5* and *W6* are below *30%* of their initial stiffness values at *0.30%*, while a similar drop is observed for wall *W4* at a drift ratio of *0.45%*. The results show that the stiffness of flanged and boundary element walls is reduced at a higher rate at low drifts compared to rectangular walls. This is mainly attributed to the lower reinforcement ratios used in flanged and boundary element walls (*W2*, *W3*, *W5,* and *W6*) in order to achieve the same lateral strength as their rectangular counterparts (*W1* and *W4*), and also to the significant reduction in the compression zone depth of the former walls, leading to their lower cracked stiffness values.

Figure 3.5 shows also that the normalized stiffness degradation of walls *W1* and *W4* are almost similar up to *0.30%* drift (*36%* of the initial stiffness, K_i) although the reinforcement ratio of wall *W4* is *2.4 times* that of wall *W1*. However, at larger drift ratios, the stiffness of wall *W4* degrades at a slower rate than wall *W1*. Regarding walls *W2* and *W5* with flanged ends and walls *W3* and *W6* with boundary elements, the stiffness

degradation trends for both wall configurations are similar at low drift ratios up to *0.15%* drift. Beyond this drift level, the stiffness degrades to *47%* and *40%* of their initial stiffness values for the flanged and boundary element walls, respectively. Also, at higher drifts, walls *W2* and *W3* have a higher stiffness degradation when compared to walls *W5* and *W6*.

Table 3.3 presents the normalized stiffness values of all the walls at yield, maximum load, and ultimate level (i.e., 80% strength degradation). The table shows that flanged and boundary element walls (*W2*, *W3*, *W5,* and *W6*) have lower normalized stiffness values when compared to their rectangular counterparts (*W1* and *W4*) at yield, maximum load, and ultimate level. When comparing the normalized stiffness values of *Phase I* walls to their *Phase II* counterparts, the values are fairly similar at the maximum load and the ultimate level. However, at yield, wall *W4* has lower normalized stiffness values relative to wall *W1*, while walls *W5 and W6* have higher normalized stiffness values when compared to walls *W2* and *W3*.

In conclusion, it is clear that flanged and boundary element walls have higher stiffness degradation rates than rectangular ones. These higher rates are attributed to the typically low vertical reinforcement ratios used in the flanged and boundary element walls compared to their rectangular counterparts. As a reminder, such lower ratios were utilized to achieve similar wall capacities to facilitate direct comparisons between the different wall configurations—one of the main goals of the current study. Coupled with the reduced compression zone depths, such low vertical reinforcement ratios resulted in lower cracked stiffness values and subsequently higher stiffness degradation rates for flanged and boundary elements walls relative to rectangular walls. The normalized stiffness values for

walls tested in *Phase I* with low reinforcement ratios are also lower than those for *Phase II* walls with high reinforcement ratios (i.e., except wall *W4*). The high stiffness degradation rate at low drift levels leads to period elongation of structures at the early stages of loading, thus minimizing their seismic design demands in an event of a major earthquake.

3.4.5 Energy Dissipation

Energy dissipation is a key aspect of seismic design as it facilitates reducing the amplitude of the seismic response through damping. Therefore, the ductility and strength demands are expected to be reduced on structures with high energy dissipation capacities. Previous research studies (Sinha et al. 1964; Jamison 1997) showed that calculating the energy dissipation, based on the area of the envelope of the load-displacement hysteresis loops, is not exactly accurate as the energy dissipated is directly related to the imposed displacement increments and the corresponding number of cycles. In this respect, the energy dissipation is calculated in the current study based on the sum of the areas enclosed by the force-displacement curve at each displacement level, as suggested by Hose and Seible (1999) and Priestley et al. (2007).

Figure 3.6(a) shows the energy dissipation values with respect to the lateral displacements (and percentage drifts) of the walls. At low drift levels, the energy dissipation is similarly low for all walls, indicating that walls were at early stages of loading (up to 0.2% drift) prior to significant inelastic deformation in the concrete and reinforcement took place (i.e., pre-yielding of the walls). At higher drift levels, the walls

have more energy dissipation relative to the early stages of loading. As can be seen in Figure 3.6(a), *Phase I* walls have similar energy dissipation values at the different drift levels, while wall *W5* has more energy dissipated relative to other *Phase II* walls at later stages of loading (from 0.4% drift). For example, the figure shows that the energy dissipation values at 0.75% and 1.25% drift are on average 50% and 40% higher for wall *W5*, respectively than those for walls *W4* and *W6*.

To facilitate direct comparisons between the walls within each phase, the energy dissipation values against multiples of each wall's yield displacement are plotted in Figure 3.6(b). This is mainly performed because the displacement histories are not identical for all the test walls as the loading cycles are performed at multiples of the initial yield displacement of each wall, Δ_y. As can be seen in the figure, all walls have similar low energy dissipation up to the yield displacement, Δ_y, as discussed earlier in Figure 3.6(a). Beyond the yield displacement level, Δ_y, Figure 3.6(b) shows that the walls within each phase (*W1*, *W2,* and *W3* in *Phase I* and *W4*, *W5,* and *W6* in *Phase II*) have similar high energy dissipation values. For example, at $4\Delta_y$, the maximum variation in the energy dissipation values between walls *W1*, *W2,* and *W3* is 4%, while the same variation is 19% between walls *W4*, *W5,* and *W6*. Beyond $4\Delta_y$, unlike wall *W4*, the energy dissipation of walls *W5* and *W6* increased significantly, as can be seen in Figure 3.6(b), because such flanged and boundary element walls sustained higher displacement levels and showed more inelastic deformations than the former rectangular wall (*W4*).

For a better comparison between *Phase I* and *Phase II* walls, the energy dissipation values for each wall are further normalized. The normalized energy dissipation is defined

in the current study as the ratio between the energy dissipation at any post-yield displacement level to that at the yield displacement level for each wall. The reason behind normalizing the energy dissipation values is to better compare the increase in the energy dissipation values between *Phase I* and *Phase II* walls, shown earlier in Figure 3.6(b), by eliminating the difference in the wall strengths. Figure 3.7 shows the normalized energy dissipation with respect to multiples of each wall's yield displacement, Δ_y. As can be seen in the figure, up to $3\Delta_y$, the normalized energy dissipation values increase at the same rate for all the walls, except wall *W5* which has a higher rate relative to the remaining walls at an earlier stage of loading (from 1.5 Δ_y). From $3\Delta_y$ to $5\Delta_y$, flanged and boundary element walls of *Phase I* (*W2* and *W3*), have a lower rate of increase in the energy dissipated when compared to the rest of the walls. This lower rate is due to the primary flexural cracks that occurred in walls *W2* and *W3* at earlier stages of loading near the wall-foundation interface that controlled the failure of the walls (El-Azizy et al. 2015), which explains the unexpected normalized energy dissipation trends of both walls. Beyond $5\Delta_y$, walls *W5* and *W6* were cycled to further displacement levels with more inelastic deformations, and therefore, their normalized energy dissipation values increase until their failure at almost $6\Delta_y$, as shown in Figure 3.7.

The results clearly show that significantly more energy dissipation is to be expected from flanged- *(W5)* and boundary element- *(W6)* walls with high vertical reinforcement ratios compared to similar walls with low vertical reinforcement ratios *(W2* and *W3)* or rectangular walls regardless of their reinforcement ratios *(W1* and *W4)*. The high energy dissipation values of walls *W5* and *W6* might be attributed to the secondary cracks that

were initiated because of the high reinforcement ratios of such walls at their critical outer regions, which distributed the rebar plastic strains over multiple cracks, thus increasing the energy dissipation of such flanged and boundary element walls over all other test walls. Such increased energy dissipation would in turn result in reduced seismic demands due to the increased damping following yield.

3.4.6 Equivalent Viscous Damping

The hysteretic damping behavior of the walls is defined in the current study by the equivalent viscous damping ratio, ξ_{eq}. that is calculated based on an equal area approach, representing the same quantity of energy loss for each cycle (Hose and Seible 1999; Chopra 2000). The equivalent viscous damping ratio, ξ_{eq}. is computed by combining the dissipated energy, E_d, and the strain energy, E_s, as presented in Eq. 3.2

$$\xi_{eq} = \frac{1}{4\pi} \times \left(\frac{E_d}{E_s}\right) \tag{3.2}$$

The equivalent viscous damping ratio, ξ_{eq}. is plotted against the lateral displacement (and percentage drift) for each wall as shown in Figure 3.8(a), and is also plotted against multiples of each wall's yield displacement, Δ_y, as shown in Figure 3.8(b). From both figures, all the walls in general have an increase in the damping ratios as the displacement values increase (except walls *W5* and *W6* up to 2.6 Δ_y and 6.0 Δ_y, respectively).

Presenting the viscous damping ratio, ξ_{eq}, of the walls is expected to influence the equivalent-damping ratio of a building, comprised of these walls, even though the viscous damping ratio is related to the whole structure rather than individual wall elements. Based on dynamic response measurements of structures, the equivalent viscous damping ratio,

ξ_{eq}, for *RC* could be assumed to vary between 5% to 7% in the elastic range and up to the yield strength (Paualay and Priestly 1992; NBCC 2015). However, the equivalent viscous damping ratios ξ_{eq} vary between *20-30%* at *1%* top drift for all walls, as shown in Figure 3.8(a). Figure 3.8(b) shows also that the equivalent viscous damping ratios, ξ_{eq}, vary between *8-17%* at the onset of yielding, Δ_y. While the equivalent viscous damping ratios, ξ_{eq}, vary between *10-20%* and *14-27%* at $2\Delta_y$ and $3\Delta_y$, respectively. These results show that the *RC* structural walls could experience high levels of damping post-yielding, resulting in seismic demand reductions. In addition, the equivalent viscous damping ratio, ξ_{eq}, increases in general when the lateral displacements increase, as shown in Figure 3.8(a). Therefore, *RC* structures can be assigned different damping ratios depending on their design limit states. Specifically, structures designed to be fully operational could be assigned lower damping ratios, while higher damping ratios could be assigned to structures designed for collapse prevention.

3.5 CONCLUSIONS

The current study presented a detailed analysis of six reinforced concrete (RC) shear walls with different configurations (i.e., rectangular, flanged, and boundary elements) that were tested under quasi-static cyclic loading to represent seismic demands. The walls had the same overall dimensions and were tested in two phases, where *Phase II* walls had *2.4 times* the vertical reinforcement ratio used in *Phase I* walls. The analysis results were presented in terms of the wall end strains, extents of plasticity, curvature profiles, stiffness

degradation trends, energy dissipation capacities, and equivalent viscous damping ratios. The analysis presented in the current study provided the following conclusions:

- The average compressive strains at the maximum load over the bottom *150 mm* and *300 mm* reached values up to *2.5* times and *1.5* times the ultimate compressive strain of *0.0035* stipulated by major design standards worldwide (e.g., CSA A23.3-19). The actual compressive strains would not affect the ultimate strength but would majorly affect the predicted curvatures.
- *Phase II* walls (*W4*, *W5,* and *W6*) with high vertical reinforcement ratios had larger plastic hinge lengths than their *Phase I* counterparts (*W1*, *W2,* and *W3*) with low vertical reinforcement ratios. This was due to the formation of several secondary cracks that extended the inelastic deformations over the height of the former walls, and thus, larger plastic hinge lengths relative to the latter walls.
- In both phases, rectangular walls (*W1* and *W4*) had higher yield curvatures when compared to flanged and boundary element walls (*W2*, *W3*, *W5,* and *W6*). *Phase II* walls (*W4*, *W5,* and *W6*) had also higher yield curvatures relative to their *Phase I* counterparts (*W1*, *W2,* and *W3*). In general, the experimental yield curvatures of the walls were in agreement with their corresponding theoretical curvatures.
- *Phase II* walls with flanges and boundary elements (*W5* and *W6*) achieved higher ultimate curvatures relative to the rectangular wall (*W4*); however, this finding was not observed in *Phase I* walls because of the concentration of primary cracks in walls *W2* and *W3* with flanges and boundary elements due their low vertical reinforcement

ratios, leading to lower-than-expected ultimate curvatures. For these reasons, the ultimate curvature of all the walls is well predicted, except for walls *W2* and *W3*.

- In both phases, walls with flanges and boundary elements (*W2*, *W3*, *W5,* and *W6*) had higher stiffness degradation rates relative to rectangular walls (*W1* and *W4*), and thus, lower seismic demands are expected on the former walls.
- Walls with flanges and boundary elements coupled with high vertical reinforcement ratios (*W5* and *W6*) had higher normalized energy dissipation values than similar wall configurations with low vertical reinforcement ratios (*W2* and *W3*) or rectangular walls regardless of their reinforcement ratios (*W1* and *W4*).
- The equivalent viscous damping ratio of the walls varied between *8-17%* at yield and up to *27%* at later stages of loading, Therefore, different and higher (i.e., than the typical *5-7%*) equivalent viscous damping ratios can be used in the elastic and inelastic ranges when *RC* shear walls are seismically designed.

Overall, the results demonstrated that *Phase II* walls with flanges and boundary elements (*W5* and *W6*) achieved better seismic performance than both; the rectangular wall of *Phase II* (*W4*) and *Phase I* walls with flanges and boundary elements (*W2* and *W3*). These findings support the enhancement strategies recommended by the Canterbury earthquake commission report (Canterbury Commission Report, 2011), including the use of high and confined vertical reinforcement ratios at the wall toes.

Based on the analysis results of the test walls, relevant design standards (e.g., CSA A23.3 and ACI 318) should consider addressing the following points in their future editions: i) *RC* shear walls may be assigned ultimate design compressive strain values

higher than *0.0035*; ii) reinforcement ratios of *RC* shear walls is key in determining such walls' plastic hinge lengths; iii) higher equivalent viscous damping ratios should be introduced for *RC* shear walls at yield and ultimate stages; and iv) *RC* shear walls should be assigned different ductility-related modification factors based on their corresponding end (e.g., rectangular, flanged, boundary elements). Unlike the NBCC (2020) as well as other building codes not listed herein that each assigns a single value of ductility-related modification factor for ductile *RC* shear walls, the study results demonstrated that different factors should be introduced for *RC* walls considering their wide range of design parameters as *Phase I* and *II* walls showed different cyclic performances when subjected to similar seismic demands. Nonetheless, as to be expected when such provisions are recommended, more studies are still needed to further verify and fine-tune such recommendations through enriching the experimental database with additional *RC* shear walls with different geometrical configurations (e.g., aspect ratios) and design parameters (e.g., axial load levels).

3.6 REFERENCES

ACI Committee. (2019). Building code requirements for structural concrete and commentary. ACI 318-19. American Concrete Institute.

Adebar, P., Ibrahim, A. M., & Bryson, M. (2007). Test of high-rise core wall: effective stiffness for seismic analysis. *ACI Structural Journal*, *104*(5), 549.

Akl, A., & Ezzeldin, M. (2023). Seismic collapse risk assessment of low-aspect-ratio reinforced concrete shear walls using the FEMA P695 methodology. *Journal of Structural Engineering*, http://10.1061/(ASCE)ST.1943-541X.0003505.

American Society for Testing and Materials (ASTM). (2021). *Standard test method for compressive strength of cylindrical concrete specimens*. C39/C39M-21. ASTM International, West Conshohocken, PA, USA.

American Society for Testing and Materials (ASTM). (2020). *Standard specification for deformed and plain carbon-steel bars for concrete reinforcement*. A615/A615M-20b. ASTM International, West Conshohocken, PA, USA.

Canadian Standards Association (CSA). (2019). *Design of concrete structures*. CSA A23.3-19, CSA, Mississauga, Canada.

Canadian Standards Association (CSA). (2021). *Carbon steel bars for concrete reinforcement.* CSA G30.18-21, CSA, Mississauga, Canada.

Canterbury Earthquake Royal Commission report. (2011). *Seismic performance Christchurch building under the Canterbury Earthquake.* Retrieved Nov. 19th, 2019, http://canterbury.royalcommission.govt.nz/Final-Report-Volume-One-Contents

Chopra, A. (2000). *Dynamics of structures; theory and application to earthquake engineering.* 2nd ed. Englewood Cliffs, NJ, USA; Prentice Hall Inc.

Christidis, K. I., & Trezos, K. G. (2017). Experimental investigation of existing non-conforming RC shear walls. *Engineering Structures*, *140*, 26-38.

El-Azizy, O., El-Dakhakhni, W. W., Shedid, M., & Drysdale, R. (2013). Comparative Seismic Performance Study between reinforced concrete and reinforced masonry structural walls. In *12th Canadian Masonry Symposium*.

El-Azizy, O. A., Shedid, M. T., El-Dakhakhni, W. W., & Drysdale, R. G. (2015). Experimental evaluation of the seismic performance of reinforced concrete structural walls with different end configurations. *Engineering Structures*, *101*, 246-263.

Ghorbanirenani, I., Tremblay, R., Léger, P., & Leclerc, M. (2012). Shake table testing of slender RC shear walls subjected to eastern North America seismic ground motions. *Journal of Structural Engineering*, *138*(12), 1515-1529.

Gondia, A., Ezzeldin, M., & El-Dakhakhni, W. (2020). Mechanics-guided genetic programming expression for shear-strength prediction of squat reinforced concrete walls with boundary elements. *Journal of Structural Engineering*, *146*(11), 04020223.

Hose, Y. D., & Seible, F. (1999). *Performance evaluation database for concrete bridge components and systems under simulated seismic loads*. Pacific Earthquake Engineering Research Center, College of Engineering, University of California.

Luu, H., Léger, P., & Tremblay, R. (2014). Seismic demand of moderately ductile reinforced concrete shear walls subjected to high-frequency ground motions. *Canadian journal of civil engineering*, *41*(2), 125-135.

Jamison Jr, J. B. (1997). *Monotonic and cyclic performance of structurally insulated panel shear walls* (Doctoral dissertation, Virginia Tech).

Massone, L. M., & Wallace, J. W. (2004). Load-deformation responses of slender reinforced concrete walls. *Structural Journal*, *101*(1), 103-113.

NBCC (2015): National Research Council of Canada (2015). *National Building Code of Canada.*

Park, R., & Paulay, T. (1975). *Reinforced concrete structures*, John Wiley & Sons. *NY, USA*.

Paulay, T., & Priestley, M. N. (1992). *Seismic design of reinforced concrete and masonry buildings* (Vol. 768). New York: Wiley.

Priestley, M. J. N. (2000). Performance-based seismic design. *Bulletin of the New Zealand society for earthquake engineering*, *33*(3), 325-346.

Priestley, M. N., Seible, F., & Calvi, G. M. (1996). *Seismic design and retrofit of bridges*. John Wiley & Sons.

Priestley, M. J. N., Calvi, G.M., & Kowalsky, M. J., (2007). *Displacement-based seismic design of structures.* Pavia, Italy: IUSS Press, Pavia, Italy.

Rong, X. L., Zheng, S. S., Zhang, Y. X., Zhang, X. Y., & Dong, L. G. (2020). Experimental study on the seismic behavior of RC shear walls after freeze-thaw damage. *Engineering Structures*, *206*, 110101.

Shedid, M. T., Drysdale, R. G., & El-Dakhakhni, W. W. (2008). Behavior of fully grouted reinforced concrete masonry shear walls failing in flexure: Experimental results. *Journal of structural engineering*, *134*(11), 1754-1767.

Shedid, M. T., El-Dakhakhni, W. W., & Drysdale, R. G. (2010). Alternative strategies to enhance the seismic performance of reinforced concrete-block shear wall systems. *Journal of structural engineering*, *136*(6), 676-689.

Sinha, B. P., Gerstle, K. H., & Tulin, L. G. (1964, February). Stress-strain relations for concrete under cyclic loading. In *Journal Proceedings* (Vol. 61, No. 2, pp. 195-212).

Thomsen IV, J. H., & Wallace, J. W. (1995). *Displacement-based design of RC structural walls: experimental studies of walls with rectangular and T-shaped cross sections* (Vol. 6). Report No. CU/CEE-95.

Thomsen IV, J. H., & Wallace, J. W. (2004). Displacement-based design of slender reinforced concrete structural walls—experimental verification. *Journal of structural engineering*, *130*(4), 618-630.

Tomazevic, M. (1999). *Earthquake-resistant design of masonry buildings* (Vol. 1). World Scientific.

Zhang, Y., & Wang, Z. (2000). Seismic behavior of reinforced concrete shear walls subjected to high axial loading. *Structural Journal*, 97(5), 739-750.

3.7 TABLES

Table 3.1: Design parameters and reinforcement details of the test walls (El-Azizy et. al 2015)

Specimen	Configuration	Wall Dimensions	Vertical Reinforcement		Horizontal Reinforcement		Axial Stress (MPa)	Axial ($\%f'_c$)
			Number of Bars and Bar Sizes	ρ_v (%)	D4 at Spacing (mm)	ρ_h (%)		
W1	Rectangular	1,802 mm × 3,990 mm length×height	42 D7	1.17	2 at 90	0.64	1.09	3.85
W2	Flanged		16 D7 & 22 D4	0.66	2 at 110	0.53	0.89	3.15
W3	Boundary Elements		20 D7 & 18 D4	0.69	2 at 110	0.53	0.89	3.15
W4	Rectangular		64 D11	2.80	2 at 45	1.28	1.09	2.66
W5	Flanged		16 D11 & 44 D7	1.58	2 at 55	1.05	0.89	2.17
W6	Boundary Elements		20 D11 & 40 D7	1.63	2 at 55	1.05	0.89	2.17

Table 3.2: Theoretical and average experimental values over the bottom *150 mm* of yield curvature ϕ_y, and ultimate curvature ϕ_u

	Phase I Walls						*Phase II* Walls					
	W1		*W2*		*W3*		*W4*		*W5*		*W6*	
	Exp.	Theo.	Exp.	Theo.	Exp.	Theo.	Exp.	Theo.	Exp.	Theo.	Exp.	Theo.
Yield Curvature $\phi_y \times 10^{-3}$ (rad/m)	1.94	1.82	1.27	1.71	1.43	1.75	2.01	1.99	1.73	1.83	1.76	1.88
Ultimate Curvature $\phi_u \times 10^{-3}$ (rad/m)	10.03	10.43	7.27	45.81	7.07	28.57	6.71	6.83	14.84	16.09	11.92	14.43

Note: The theoretical yield and ultimate curvatures were computed based on the average material properties of the walls, as presented in El-Azizy et al. (2015).

Table 3.3: Normalized stiffness for the test walls at yield, maximum load, and ultimate level

			Normalized Stiffness					
			At Yield, K_y *(%)*		At Maximum Load, K_u *(%)*		At Ultimate Level, $K_{0.8u}$ *(%)*	
Walls	Configuration		Push (+ve)	Pull (-ve)	Push (+ve)	Pull (-ve)	Push (+ve)	Pull (-ve)
W1	Rectangular	*Phase I*	53	34	24	24	13	10
W2	Flanged	*Phase I*	22	28	14	14	9	5
W3	Boundary Elements	*Phase I*	26	27	14	14	5	6
W4	Rectangular	*Phase II*	33	40	22	20	15	14
W5	Flanged	*Phase II*	38	37	-	12	-	6
W6	Boundary Elements	*Phase II*	28	30	15	14	6	6

3.8 FIGURES

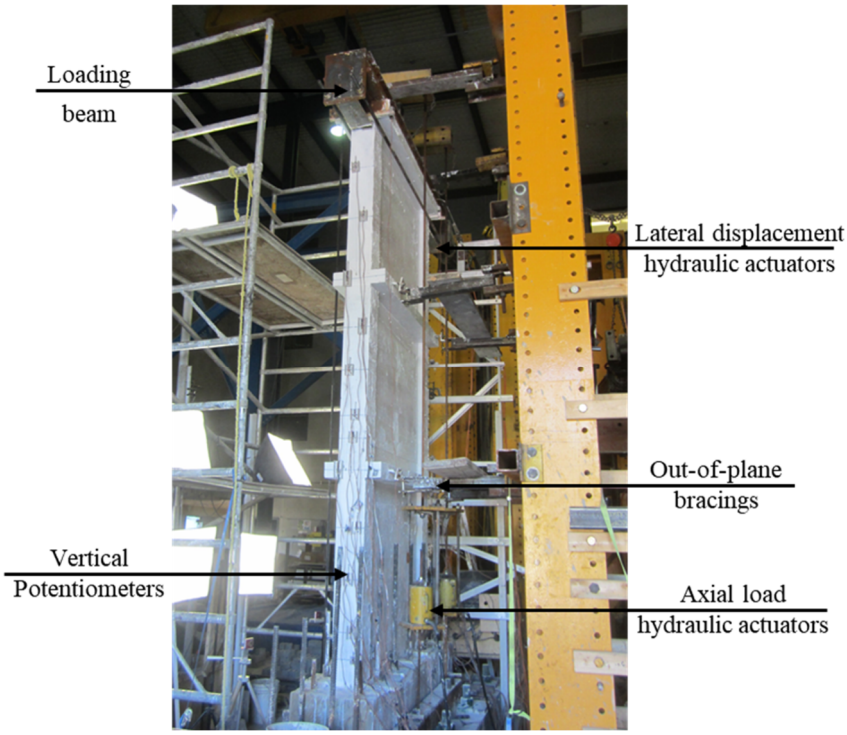

(a)

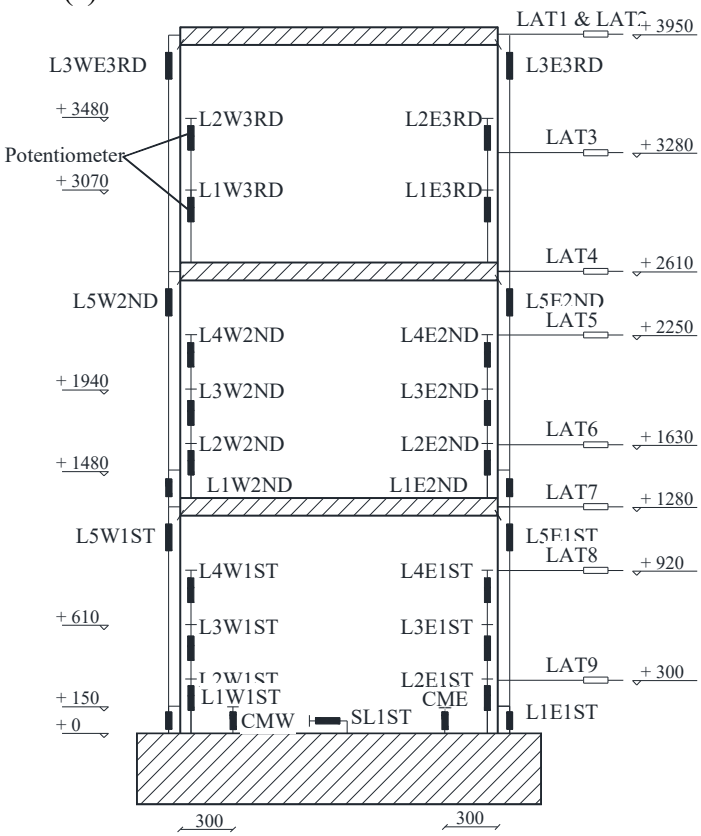

(b)

Figure 3.1: Experimental program: (a) Test setup; and (b) Potentiometer locations

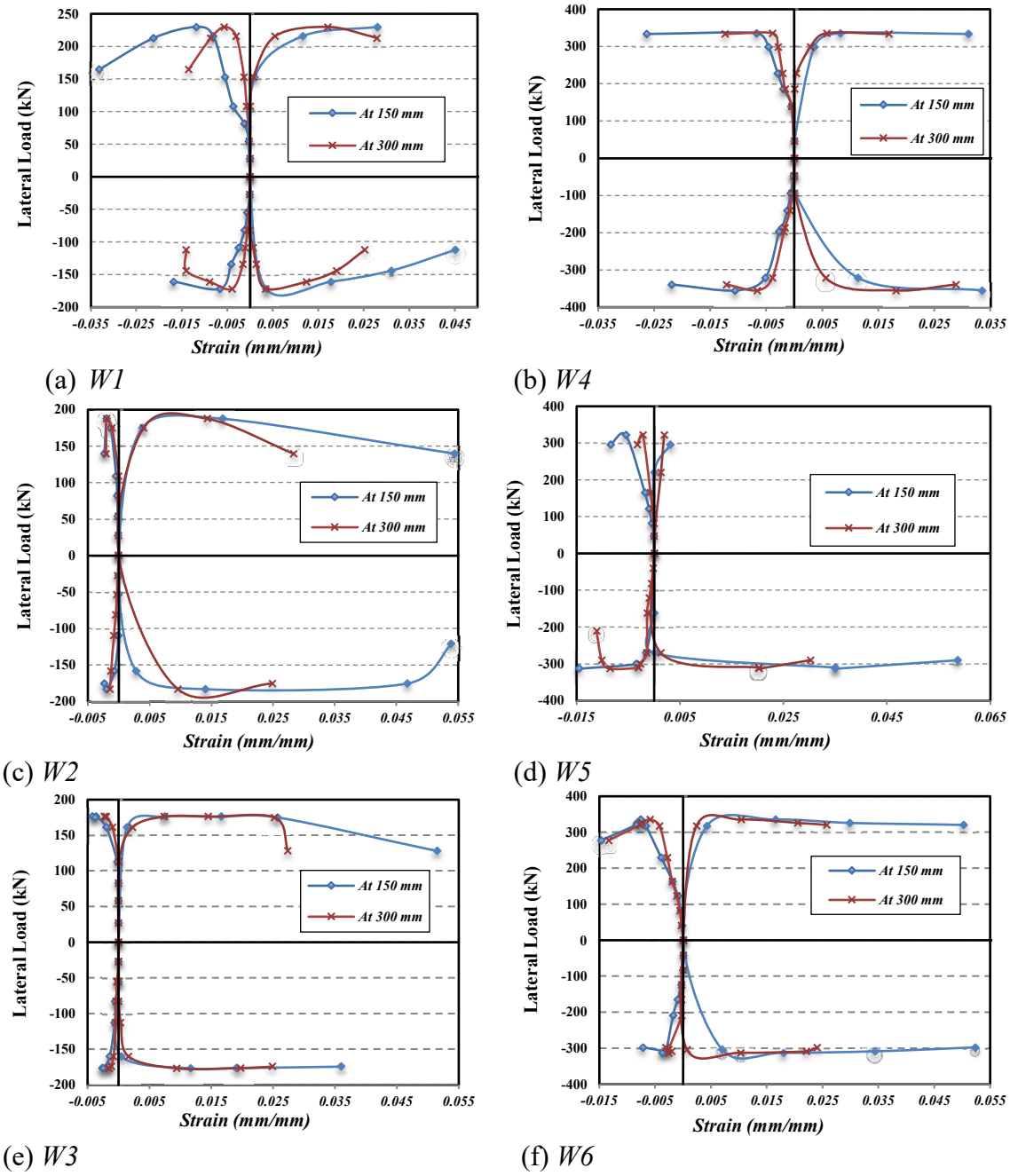

Figure 3.2: Average concrete strains over the lower *150 mm* and *300 mm* of walls: (a) *W1*; (b) *W4*; (c) *W2*; (d) *W5*; (e) *W3*; and (f) *W6*

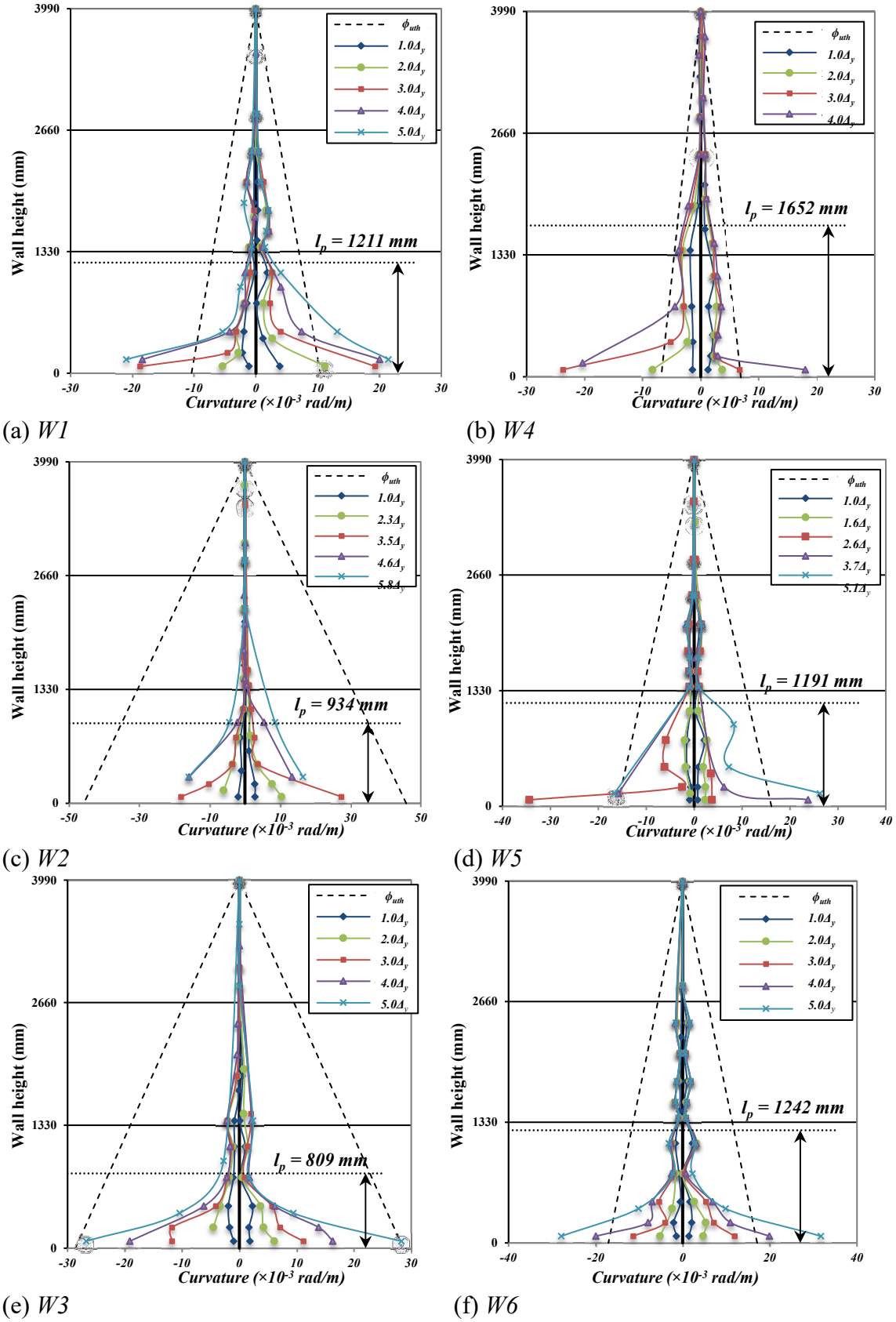

(a) *W1* (b) *W4*

(c) *W2* (d) *W5*

(e) *W3* (f) *W6*

Figure 3.3: Curvature profile along the height of walls: (a) *W1*; (b) *W4*; (c) *W2*; (d) *W5*; (e) *W3*; and (f) *W6*

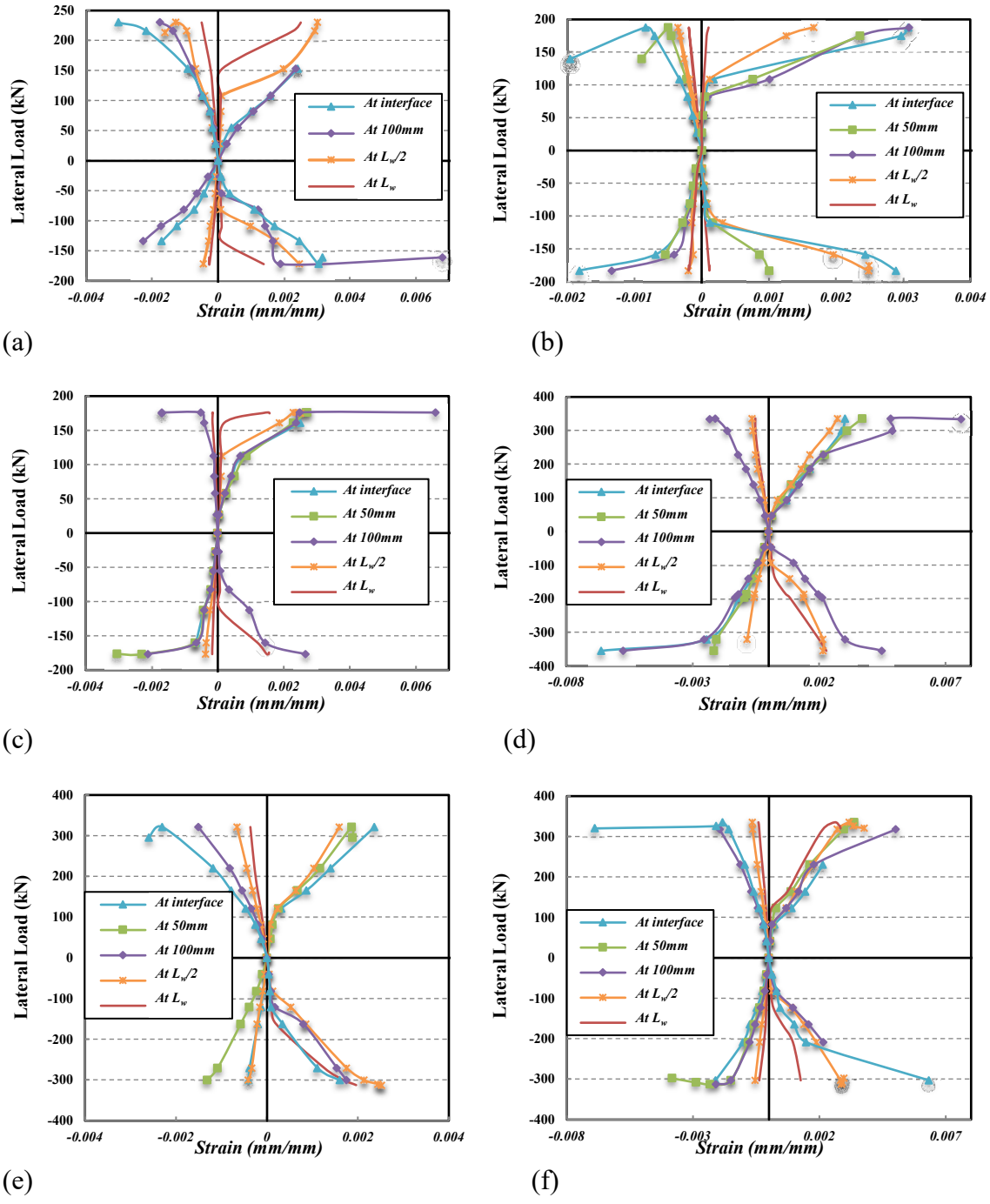

Figure 3.4: Load versus strains in outermost vertical reinforcement bars at different elevations (a) *W1*; (b) *W2*; (c) *W3*; (d) *W4*; (e) *W5*; and (f) *W6*

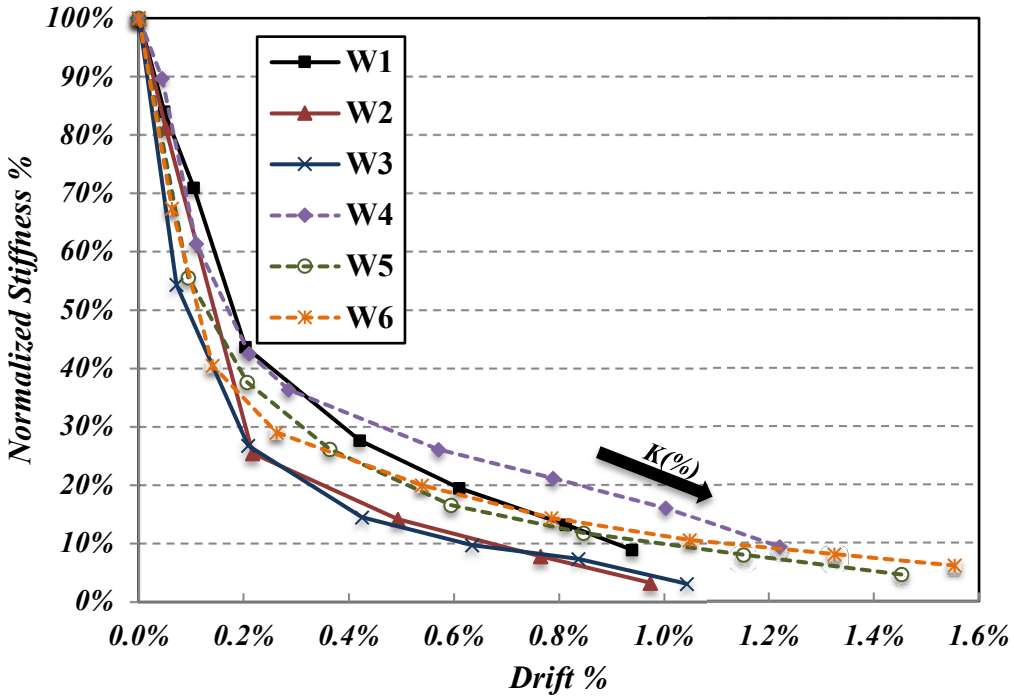

Figure 3.5: Normalized stiffness versus lateral drift

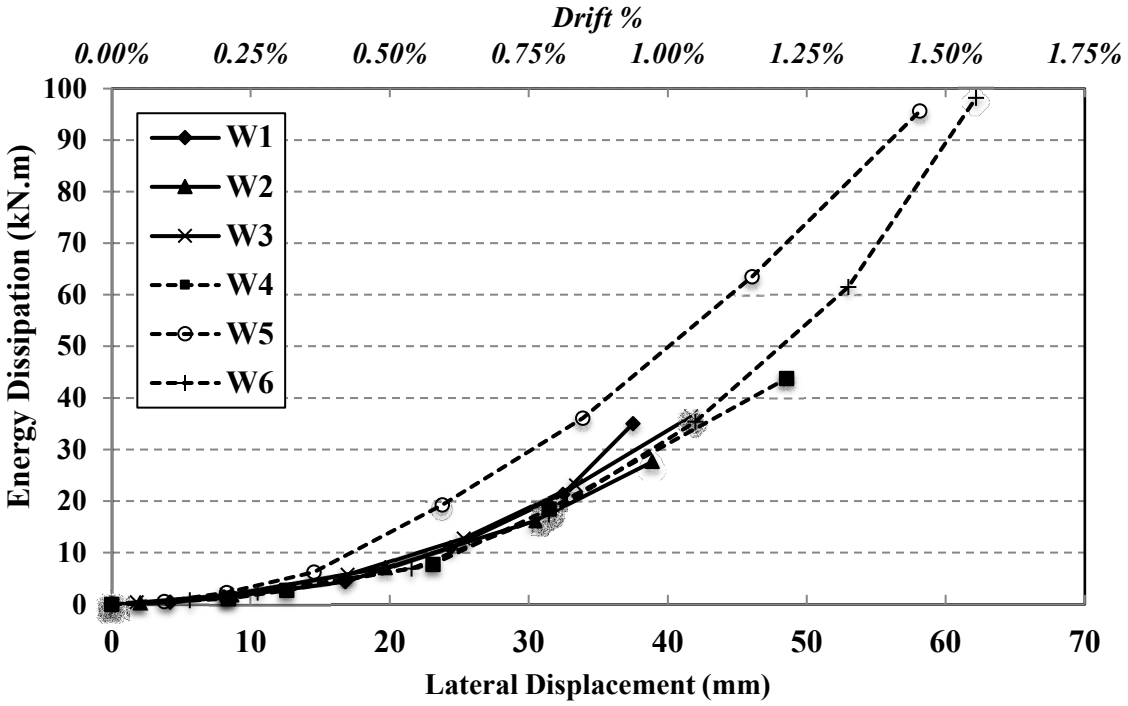

(a)

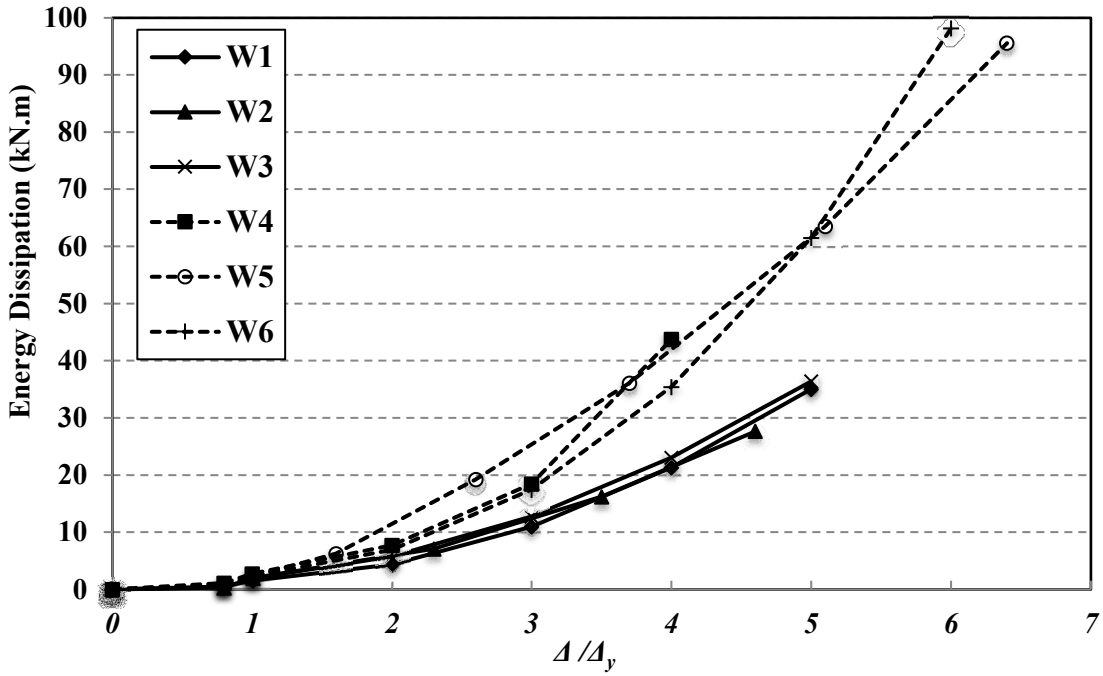

(b)

Figure 3.6: Energy dissipation versus (a) Lateral displacement and drift; and (b) Δ/Δ_y

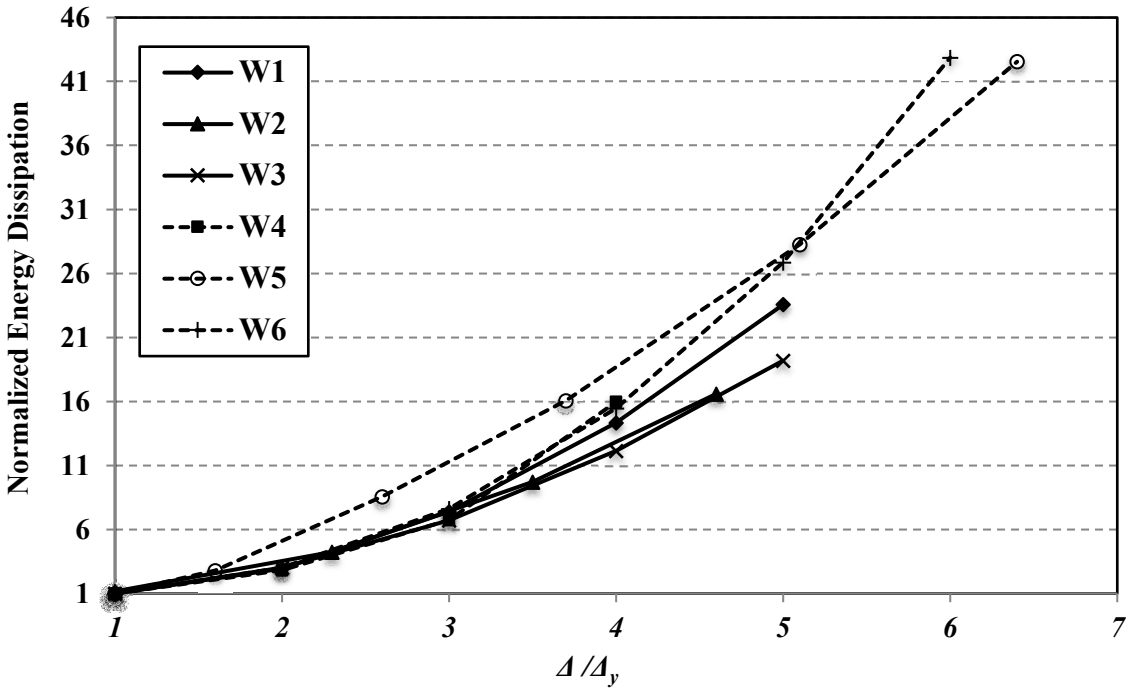

Figure 3.7: Normalized energy dissipation versus Δ/Δ_y

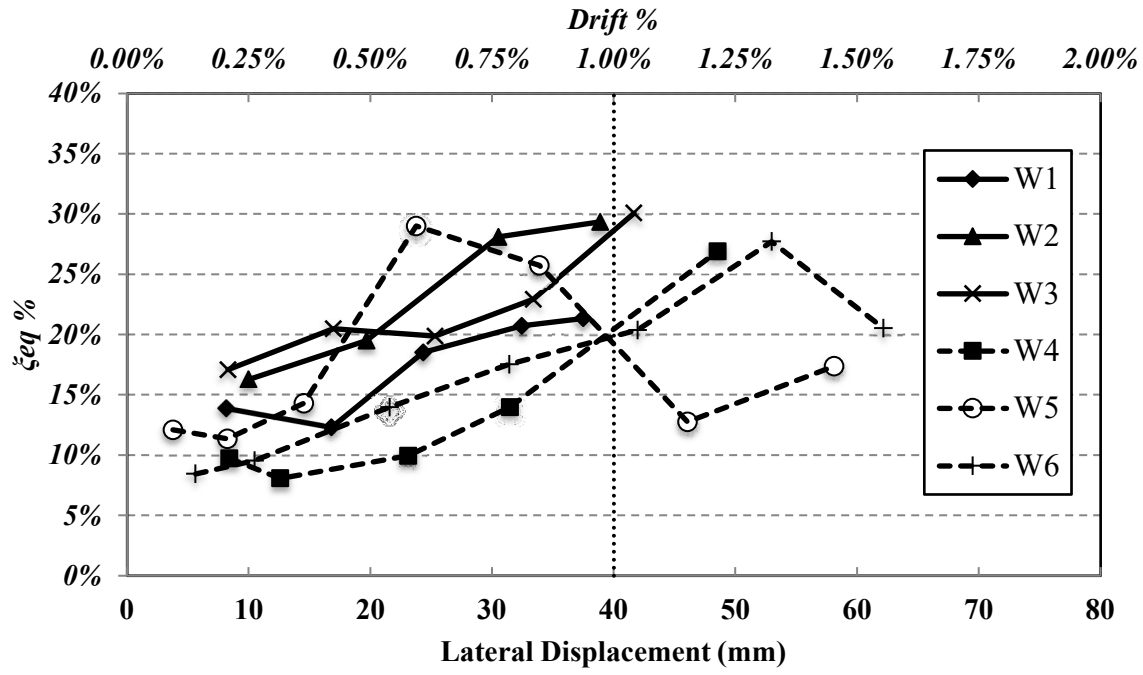

(a)

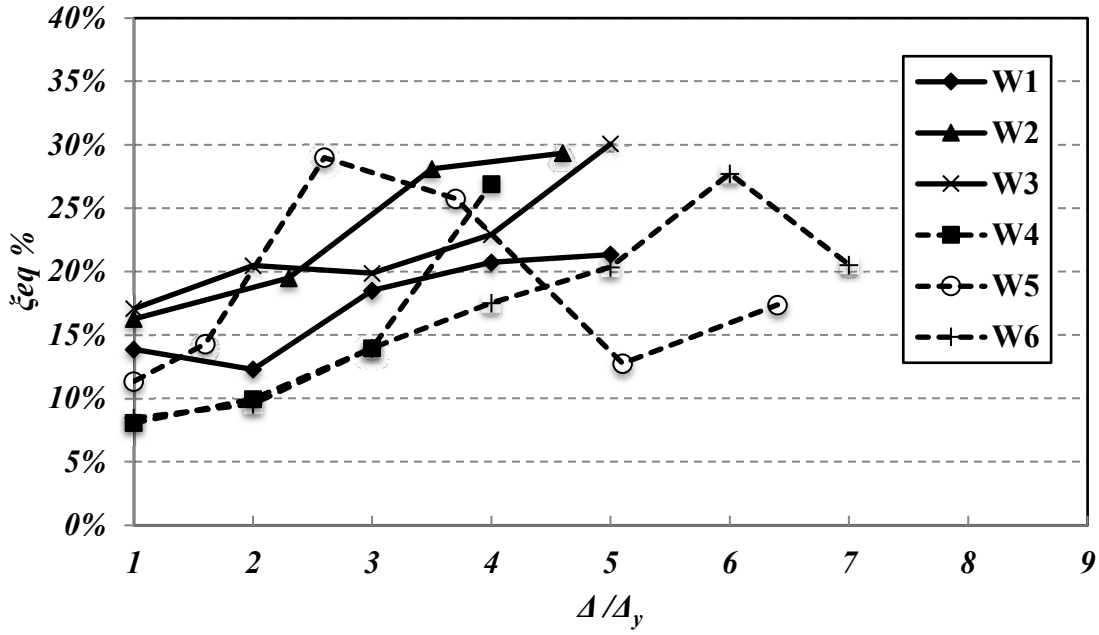

(b)

Figure 3.8: Equivalent viscous damping $\xi_{eq}\%$ versus (a) Lateral displacement and drift; and (b) Δ/Δ_y

CHAPTER 4
DATA-DRIVEN DISPLACEMENT DUCTILITY EXPRESSIONS FOR REINFORCED CONCRETE SHEAR WALLS WITH DIFFERENT CONFIGURATIONS

4.1 ABSTRACT

In several previous seismic events (e.g., the 2011 Canterbury Earthquake in New Zealand and the 2010 Maule earthquake in Chile), reinforced concrete (RC) shear walls did not show the expected seismic performance in terms of their ductility capacities. Therefore, the main objective of the current study is to develop data-driven expressions for *RC* shear walls that better quantify their displacement ductility when a wide range of geometrical configurations and design parameters are adopted. In this respect, based on the modified compression field theory, an analytical model is developed and experimentally validated to simulate the seismic response of *RC* shear walls with different configurations. The model is then used to perform nonlinear static pushover analyses on 40 full-scale rectangular *RC* walls and 53 full-scale *RC* walls with flanges and boundary elements. The analysis results are subsequently used to develop two data-driven expressions (i.e., using an inverse linear regression technique) that predict the displacement ductility of *RC* walls with rectangular and flange/boundary element configurations. To verify their effectiveness, the two developed expressions are validated using experimental results that are not originally used during the development of both the analytical model and such two expressions. Finally, the interpretability of the two expressions is evaluated to conform their outcomes with the mechanics of *RC* shear walls in terms of the thickness, aspect ratio, axial load level, vertical reinforcement ratio, and concrete compressive strength of such walls. The current study enlarges the database of displacement ductility capacity predictive expressions that will

facilitate a better understanding of the seismic response of *RC* shear walls with rectangular, flange, and boundary element configurations.

4.2 INTRODUCTION

According to the Canterbury earthquake royal commission report (Canterbury Commission Report, 2011), well-detailed reinforced concrete (RC) shear walls did not achieve the expected seismic performance due to the concentration of plastic strains at the location of the primary cracks. The report also indicated that *RC* walls with low vertical reinforcement ratios showed low ductile behavior as the use of these reinforcement ratios limited the formation of secondary cracks. Such *RC* shear walls were originally designed according to the New Zealand Standards (NZS 3101, 2006) that specify a minimum vertical reinforcement ratio, ρ_v, of 0.25%. However, Sritharan et al. (2014) demonstrated that *RC* shear walls, designed using this minimum vertical reinforcement ratio, may not show the expected ductility capacity. During the 2010 Maule earthquake in Chile, *RC* shear walls achieved also low seismic performance due to their high out-of-plane slenderness ratios (i.e., small thicknesses) and high axial load levels that negatively affected the ductility of such *RC* walls (Jünemann et al. 2012). Low ductility capacities were also attributed to poor detailing and confinement (Carpenter et al. 2011) and poor web-boundary detailing (Wallace et al. 2012). Such reinforcement detailing deficiencies resulted in severe strength degradation once the outermost vertical bar buckled after concrete crushing.

According to the aforementioned seismic events, as well as others not listed herein, inelastic deformations are expected to occur in *RC* shear walls forming the seismic force-

resisting system. Thus, it is key to properly quantify the ductility capacity of *RC* shear walls in order to accurately predict their performance during seismic events. In this respect, several previous studies have been conducted to evaluate the influence of several design parameters (e.g., aspect ratios, reinforcement ratios, and axial load levels) on the ductility capacity of *RC* shear walls when designed using different geometrical configurations. For example, Thomsen and Wallace (1995) evaluated the influence of confinement and transverse reinforcement on the ductility of *RC* walls by testing two rectangular and two T-shaped shear walls. The experimental results showed that minimizing the spacing of the horizontal hoops enhanced the seismic performance of the tested walls. Zhang and Wang (2000) also investigated the seismic performance of four rectangular *RC* shear walls and concluded that high axial loads reduced the displacement ductility of such walls. In addition, Preti and Giuriani (2011) tested a full-scale *RC* wall, where the vertical reinforcement of this wall was uniformly distributed using large bar diameters. The wall showed a high ductility level, governed by flexural deformations, with an idealized displacement ductility of *8*. The effect of the axial load and confinement ratios on the ductility of seven *RC* walls with different cross-section configurations was also studied by Jiang et al. (2013). The authors demonstrated that axial loads negatively affected the ductility of the walls, while higher ductility levels were achieved when the confinement ratios increased. To the best of the authors' knowledge, all the published studies to date that have focused on *RC* shear walls under seismic loading did not provide expressions to predict the displacement ductility capacity of these walls in terms of their corresponding geometrical configurations and design parameters.

The main objective of the current study is to develop data-driven expressions for *RC* shear walls that predict their displacement ductility capacities considering a wide range of geometrical configurations and design parameters. In this respect, an analytical model is developed and experimentally validated to simulate the seismic performance of *RC* shear walls in terms of their curvature profiles, reinforcement strains, load-displacement responses, and stiffness degradation trends. Following the model development and validation, nonlinear static pushover analyses are performed on 40 full-scale rectangular *RC* walls and 53 full-scale *RC* walls with flanges and boundary elements. Using inverse linear regression models, two data-driven expressions are then introduced and validated to predict the displacement ductility of *RC* shear walls with rectangular and flange/boundary element configurations, respectively. Finally, the interpretability of the two expressions is investigated to verify their outcomes with the mechanics of *RC* shear walls in terms of the wall thickness, aspect ratio, axial load level, vertical reinforcement ratio, and concrete compressive strength.

4.3 SUMMARY OF THE EXPERIMENTAL PROGRAMS

Six half-scaled *RC* shear walls with different configurations were constructed and tested by El-Azizy et al. (2015). The walls were classified into two phases, each phase had three different configurations (i.e., rectangular, flanged, and boundary elements), as shown in Figure 4.1. *Phase II* walls (*W4*, *W5*, and *W6*) had higher reinforcement ratios by *2.4* times and higher concrete compressive strengths, f_c', by *1.5* times than *Phase I* walls (*W1*, *W2*, and *W3*), as presented in Table 4.1. The vertical reinforcement ratio, ρ_v, horizontal

reinforcement ratio, ρ_h, configuration, axial stress, and the number of bars of all the walls are also listed in Table 4.1. Scaled rebars *D11*, *D7*, and *D4* were used in the walls with cross-sectional areas of $71mm^2$, $45mm^2$, and $26mm^2$, respectively. The reinforcements used were equivalent to full-scale *M20* ($300mm^2$), *M15* ($200mm^2$), and *M10* ($100mm^2$) rebars, respectively. All the walls, classified as *Ductile* walls according to the Canadian Standards Association (CSA A23.3-19), were tested under displacement-controlled quasi-static fully-reversed cyclic loading. The walls were subjected to a constant axial load of *160 kN* throughout the test with axial stress ratios that varied between $2\text{-}4\%f_c'$, as presented in Table 4.1. The results showed that all walls failed in a ductile manner by concrete crushing of the wall toes followed by buckling and then snapping of the outermost reinforcement bars before the tests were terminated when the maximum strength degraded to *50%*. All walls showed flexural and inclined shear cracks; however, *Phase II* walls had more cracks than their *Phase I* counterparts. Full details about the experimental program and test results can be found in El-Azizy et al. (2015).

Two quarter-scaled rectangular *RC* shear walls, tested by Thomsen and Wallace (1995) under displacement-controlled quasi-static fully-reversed cyclic loading, were also used in the current study. The two walls had the same dimensions of *914mm* (height), *1219mm* (length), and *102mm* (thickness); however, the spacing of the horizontal hoops at the wall toes was different in the two walls, as shown in Figure 4.2. Table 4.1 presents the vertical and horizontal reinforcement ratios of the walls along with their axial stress ratios that ranged between $7\text{-}10\%f_c'$. The results showed that the two walls failed in a flexural ductile manner, by crushing at the wall compressive toes followed by snapping of the

outermost reinforcement in the tensile regions. Full details about the experimental program and test results can be found in Thomsen and Wallace (1995).

4.4 ANALYTICAL MODEL OF *RC* WALLS

4.4.1 Model Development

Response-2000 software (Bentz and Collins 2000) was used in the current study to simulate the seismic response of *RC* shear walls with different end configurations. The software, originally introduced by Vecchio and Collins (1986) based on the modified compression field theory, performs nonlinear sectional analyses to analyze *RC* elements when subjected to shear demands. Therefore, the *RC* shear walls were modeled in the current study by dividing the full height of each wall into *20* segments. The applied axial load, moment, and shear forces were initially determined in each segment. Then, a nonlinear sectional analysis was performed on each segment. Each segment consisted of a series of biaxial nodes that were integrated along the cross-section, where each node contained a longitudinal strain, a shear strain, and a transverse strain. The longitudinal strain, ε_x, in each section was made up of 1) the longitudinal strain, ε_{x0}, at the centroid of the cross-section; 2) the curvature, ϕ; and 3) the average shear strain, γ_{xy0}. While the shear strain was made up of a numerical profile that modified the average shear strain, γ_{xy0}, due to the shear stress profile. Regarding the transverse strain, it was calculated from equilibrium assuming no clamping transverse stress. The global curvature and shear strain attributed to each load level were interpolated from the interaction diagram, which was combined with the moment-area method to compute the load and displacement of each segment, as explained by Bentz (2000)

The confined outer regions of the walls, shaded areas in Figures 4.1 and 4.2, were considered herein using the concrete model by Saatcioglu and Razvi (1992), as presented in Eq. 4.1. The model uses the spacing, cross-sectional area of the ties, the confined areas, and the vertical reinforcement spacing to predict the strength and strain of the confined regions.

$$f'_{cc} = f'_c + k_1 f_{le} \tag{4.1}$$

where f'_{cc} is the confined concrete strength used in the outer regions of the walls; f'_c is the unconfined concrete strength obtained from cylindrical tests; and k_1 is a coefficient that is a function in the Poisson's ratio of concrete. The latter was calculated based on the overall confining pressure, f_{le} *(MPa)*, as recommended by Richarts et al. (1928) and presented in Eq. 4.2

$$k_1 = 6.7\ (f_{le})^{-0.17} \tag{4.2}$$

The core dimensions of the confined region in the two orthogonal directions (length and thickness) were presented as $b_{cx}$and b_{cy}, as shown in Figures 4.1 and 4.2. The confined region had different reinforcement tie ratios and dimensions in the two directions. Therefore, the confining pressure was computed for each direction separately. The lateral pressures f_{lx} and f_{ly} were computed using Eq. 4.3 (Saatcioglu and Razvi 1992)

$$f_{lx} = \frac{\sum A_{sh} f_{yh} \sin(\alpha)}{s b_{cx}} \;\&\; f_{ly} = \frac{\sum A_{sh} f_{yh} \sin(\alpha)}{s b_{cy}} \tag{4.3}$$

where A_{sh} is the cross-section area of the ties; f_{yh} is the yield stress of the ties; α is the angle between the transverse tie and the orthogonal dimension adjacent to the lateral pressure; s is tie spacing; b_{cx} is the confined distance in the x direction; and b_{cy} is the confined distance in the y-direction, as shown in Figures 4.1 and 4.2.

The lateral pressure in each direction was then multiplied by coefficient k_2, which was a reduction factor that accounts for the vertical reinforcement spacing and the nodal forces due to the high-stress concentration at the locations of the vertical reinforcement and the horizontal ties. The reduction coefficient, k_2, for each orthogonal direction was computed, as shown in Eq. 4.4 (Saatcioglu and Razvi 1992)

$$k_{2x} = 0.26\sqrt{\left(\frac{b_{cx}}{s}\right)\left(\frac{b_{cx}}{s_{lx}}\right)\left(\frac{1}{f_{lx}}\right)} \;\&\; k_{2y} = 0.26\sqrt{\left(\frac{b_{cy}}{s}\right)\left(\frac{b_{cy}}{s_{ly}}\right)\left(\frac{1}{f_{ly}}\right)} \tag{4.4}$$

where s_{lx} and s_{ly} are the vertical reinforcement spacing in the x and y directions, respectively.

The effective lateral pressures f_{lex} and f_{ley} in each orthogonal direction were then computed by multiplying the lateral pressures by their reduction factors, as presented in Eq. 4.5

$$f_{lex} = k_{2x}f_{lx} \;\&\; f_{ley} = k_{2y}f_{ly} \tag{4.5}$$

The overall equivalent lateral pressure, f_{le}, was computed as (Saatcioglu and Razvi 1992)

$$f_{le} = \frac{f_{lex}b_{cx} + f_{ley}b_{cy}}{b_{cx} + b_{cy}} \tag{4.6}$$

The strain ε_1 corresponding to the peak stress f'_{cc}were computed (Saatcioglu and Razvi 1992)

$$\varepsilon_1 = \varepsilon_{01}(1 + 5K) \tag{4.7}$$

where ε_{01} is the strain at the peak stress of unconfined concrete that was evaluated according to Collins and Mitchell (1991). While factor K was computed according to Eq. 4.8 (Saatcioglu and Razvi 1992)

$$K = \frac{k_1 f_{le}}{f_c'} \tag{4.8}$$

Regarding the intermediate unconfined regions of the walls, the experimental compressive strength (f_c') of the concrete was used and the corresponding strain was evaluated according to Collins and Mitchell (1991), as presented in Eq. 4.9

$$\varepsilon_{01} = \frac{f_c'}{E_c} \frac{n}{n-1} \tag{4.9}$$

where the concrete Young's modulus, E_c, was calculated according to Carrasquillo et al. (1981)

$$E_c = 3320\sqrt{f_c'} + 6900 \tag{4.10}$$

while *n* was calculated according to Popovics (1973), as shown in Eq. 4.11

$$n = 0.8 + \frac{f_c'}{17} \tag{4.11}$$

The tensile strength of concrete, f_t, was computed according to Bentz (2000)

$$f_t = 0.45(f_c')^{0.4} \tag{4.12}$$

Popovics-Thorenfeldt-Collins (Collins and Mitchell 1991) base curve was used for the heavily confined region and the intermediate regions for all the walls. Compression softening, according to Vecchio and Collins (1986), was also included. In addition, tension stiffening was captured, in Response 2000 software (Bentz and Collins 2000), based on strain and concrete cover distance to steel. Although modification factors for tension stiffening could have been used in the software, a factor of *1.0* was used herein which came in agreement with the experimental results.

The reinforcement bars used in the experimental walls were tested under tension following American Society for Testing and Materials (ASTM) A615-09 (ASTM 2009).

The experimental stress-strain relationships were then used in the developed Response-2000 analytical model (Young's modulus E_s, yield stress F_y, ultimate stress F_u, strain at strain hardening $\varepsilon_{sh,}$ and strain at ultimate stress ε_{su}). Strain hardening and yield penetration in the foundation were also included in the model. Specifically, the yield penetration factor was taken as *0.01* which came in agreement when the experimental and analytical results were compared. At the wall-foundation interface, the extent of the plastic hinge length can penetrate the foundation, thus increasing the flexural rotation and the lateral displacement of the wall, as discussed by Priestley et al. (2007) and Shedid and El-Dakhakhni (2014). To account for the extent of plasticity in the model, an additional curvature at the interface was superimposed to better predict the flexural rotation of the walls (Bentz 2000).

For all the walls, the nonlinear plane sectional analysis program loading protocol for the pushover analysis was as follows: 1) constant axial loads were applied to the cross-section of the wall models; and 2) an increasing lateral load with *0.25kN* increments was applied at the top of the wall models.

4.4.2 Model Validation

The developed Response-2000 analytical model was used to simulate the cyclic performance of the six *RC* shear walls tested by El-Azizy et al. (2015) as well as the two rectangular walls tested by Thomsen and Wallace (1995). These walls were selected as they had rectangular, flanged, and boundary element configurations and they were also reinforced vertically with different reinforcement ratios, ρ_v, varying from *0.66%* to *2.80%* while being also subjected to axial stress demands. In this subsection, the analytical model

results for each wall are compared with the experimental results in terms of the: 1) extent of plasticity; 2) reinforcement strains; 3) load-displacement relationship; 4) stiffness degradation; and 5) displacement ductility.

4.4.2.1 Extent of Plasticity

The experimental and analytical curvature profiles along the height of each wall are shown in Figure 4.3. The experimental curvature profiles are at one displacement cycle beyond the maximum lateral strength of the wall, where the strength of the walls dropped slightly by a value of up to 10% at this ultimate displacement. As can be seen in the figure, the model is able to accurately predict the experimental curvature profiles of all the walls with rectangular, flange, and boundary element configurations. The experimental and analytical plastic hinge lengths for all the walls are also presented in Figure 4.3. The plastic hinge length, l_p, presented in the figure is the height above the wall-foundation interface where the curvature values exceed the yield curvature of the wall. The experimental yield curvature was determined as the average curvature of the first potentiometers above the wall-foundation interface at the onset of reinforcement bar yielding (i.e., based on the strain gauge readings), while the analytical yield curvature was calculated at the wall-foundation interface once the wall reached the theoretical yield load. The experimental and analytical plastic hinge lengths for all the walls are listed in Table 4.2. As can be seen in Table 4.2 and Figure 4.3, for the six walls tested by El-Azizy et. al (2015), the experimental l_p values vary from $45\%l_w$ to $92\%l_w$, while the analytical l_p predictions range from $47\%l_w$ *to* $95\%l_w$, where the maximum deviation between the experimental and analytical l_p values is only *5.1%*. Therefore, it can be concluded that the experimental l_p, values are in good agreement

with their analytical l_p counterparts. As can be seen also in Table 4.2 and Figure 4.3, the model can capture the higher l_p values of *Phase II* walls relative to those of *Phase I* walls as the former walls had higher reinforcement ratios compared to the latter walls. These results agree with the Canterbury earthquake royal commission report (2011), where walls with high reinforcement ratios showed secondary cracks, thus extending the inelastic deformations along the wall heights and subsequently their plastic hinge lengths. For the two rectangular walls (*RW1* and *RW2*) tested by Thomsen and Wallace (1995), the analytical results were compared with the average curvature over the bottom *762* mm as the potentiometers of this experimental program were mounted to the walls at only *229 mm* and *762 mm* from the wall-foundation interface. Therefore, information about the experimental l_p is not available for these two walls. However, as presented in Table 4.2, the analytical l_p values for walls *RW1* and *RW2* are $111\% l_w$ and $123\% l_w$, respectively, which shows that the model can capture the influence of confinement in enhancing the plastic hinge length, where the latter wall had lower spacing between the perimeter hoops at the wall toes, as shown earlier in Figure 4.2.

4.4.2.2 Reinforcement Strains

Figure 4.4 shows the experimental and analytical loads versus the corresponding outermost rebar strains. As can be seen in the figure, at the early stages of loading, the predicted analytical strains are in good agreement with their experimental counterparts. However, at later stages of loading with high strain demands, the strain gauges attached to the outermost rebars stopped working and their readings were not reported (Thomsen and Wallace 1995; El-Azizy et. al 2015). For these reasons, Figure 4.5 is presented to compare the strains

captured from the vertically mounted potentiometers to the analytical rebar strains. In general, the analytical model is in good agreement with the experimental results with the exception of walls *W1* in the pull direction, *RW2*, and *W5* in the push direction. Wall *W1* showed low lateral loads in the pull direction during the test due to a construction error that required remedial work with high-strength mortar, as reported by El-Azizy et. al (2015). Regarding wall *RW2*, the analytical predictions capture closely the experimental results; however, beyond *0.024* strain, the analytical model showed higher strains than their experimental counterparts. This deviation might be attributed to either that the potentiometer reached its maximum stroke and could not record higher strains or that the experimental strains are average values over the bottom 229 mm and are not exactly at the wall-foundation interface. For wall *W5*, foundation cracks were reported by El-Azizy et. al (2015) when the wall was loaded in the push direction, and therefore, the corresponding experimental strains at high drift levels are not included in the figure for model validation. Overall, the level of agreement between the experimental and analytical results shown in Figure 4.5 can be considered acceptable in terms of predicting the lateral load-strain relationships of *RC* shear walls.

4.4.2.3 Load-Displacement Relationships

The analytical load-displacement relationship for each wall is plotted versus their experimental counterparts in Figure 4.6, while Table 4.3 compares the analytical and experimental ultimate lateral loads, Q_u. As can be seen in the figure, the experimental results of the walls are closely predicted by the model. For example, relative to the experimental results, the maximum deviation in the ultimate lateral load in either push or

pull direction is less than *12.5*%, *14.1*%, and *13.1*% for walls with rectangular, flange, and boundary element configurations, respectively, as presented in Table 4.3. Table 4.4 shows also that the experimental yield and ultimate displacements of the walls are well estimated by the analytical model. For example, the model captures the yield displacements of walls with rectangular, flange, and boundary element configurations with maximum deviations of *16.0*%, *6.6*%, and *7.2*%, respectively. The ultimate displacements of the same walls are also well represented by the model, with maximum deviations of *15.9*%, *4.1*%, and *5.6*%, respectively. Based on these results, it can be concluded that the analytical model can capture the experimental lateral load-displacement relationships of the walls, including the ultimate lateral loads, and the yield/ultimate displacements.

4.4.2.4 Stiffness Degradation

The secant stiffness, K_e, defined as the ratio between the lateral load and the corresponding top displacement, was used to further validate the analytical model. The secant stiffness was normalized using the theoretical gross stiffness of each wall, K_g, which was calculated based on the flexural and shear deformations

$$K_g = 1/(\frac{h_w^3}{3E_cI_g} + \frac{kh_w}{G_cA_g}) \quad (4.13)$$

where h_w is the height of the wall; A_g is the wall cross-sectional area; I_g is the gross moment of inertia; E_c is Young's modulus of concrete (CSA 2019); G_c is the shear modulus which was taken as $0.4E_c$ (CSA 2019); and k is a shape factor which was taken as 1.2.

$$E_c = 4500\sqrt{f_c'} \quad (4.14)$$

The experimental and analytical normalized stiffness values versus the lateral drifts for all walls are shown in Figure 4.7. The analytical and experimental curves show similar

responses that are characterized by high rates of degradation at lower drifts and lower rates at higher drifts. The model shows excellent correlation with the experimental results with the exception of wall *W4* at the initial stages of loading. Specifically, up to a drift ratio of *0.30%*, the analytical normalized stiffness values are lower than their corresponding experimental results. However, beyond *0.30%* drift, the analytical results of wall *W4* are in good agreement with the experimental results.

4.4.2.5 Displacement Ductility

The displacement ductility is defined as the ratio of the ultimate displacement, Δ_u, to the yield displacement, Δ_y. However, *RC* shear walls are typically characterized by nonlinear behavior, as shown earlier in Figure 4.6. Therefore, in the current study, the idealized displacement ductility is defined as the ratio between the ultimate displacement and the effective yield displacement of an equivalent elastic-perfectly plastic system that provides equal energy under the idealized curve as the actual data up to the ultimate displacement (Park and Paulay 1991; Paulay and Priestley, 1992; Tomazevic 1999; Priestley et al. 2007; Shedid et al. 2008). Specifically, as shown in Figure 4.8 for wall *W6* as a demonstration example, the effective yield displacement, Δ_{ye}, is quantified as the intersection between a horizontal line at the ultimate displacement, Δ_u, and an inclined line with a slope that is equal to the initial stiffness, K_i. This stiffness is calculated as the secant stiffness at the onset of yielding. The elevation of the horizontal line is subsequently determined by equating the area under the actual curve, highlighted in Figure 4.8 as *Area 1*, to the area below the bilinear idealized curve, indicated as *Area 2* in the same figure. The idealized displacement ductility, μ_{Δ}^{id}, can be then calculated as

$$\mu_{\Delta}^{id} = \frac{\Delta_u}{\Delta_{ye}} \quad (4.15)$$

The idealized displacement ductility, μ_{Δ}^{id}, was calculated for the analytical and experimental results, as presented in Table 4.5. The results show excellent agreement, where the maximum deviation between the analytical and experimental values are *13.7%*, *4.0%*, and *2.4%* for the rectangular, flanged, and boundary elements walls, respectively. Therefore, it can be determined that the analytical model can accurately predict the idealized displacement ductility values for *RC* shear walls.

4.5 DISPLACEMENT DUCTILITY EXPRESSIONS

A *training* dataset of *40* rectangular *RC* walls and *53 RC* walls with flanges and boundary elements was generated in the current study to develop data-driven displacement ductility expressions for such wall configurations, considering a wide range of their design parameters (i.e., wall dimensions, reinforcement ratios, axial loads, and concrete compressive strengths). As shown in Figure 4.9, the rectangular *RC* walls have vertical reinforcement ratios, ρ_v, from *0.5%* to *3%*, axial load levels, $\frac{N}{f_c' A_g}$, from *0.02* to *0.22*, concrete compressive strengths, f'_c, from *30MPa* to *50 MPa*, thickness to length ratios, b_w/l_w, from *0.05* to *0.10*, and aspect ratios, h_w/l_w, from *2.20* to *11.25*. The figure shows also that the flanged and boundary element walls have vertical flange reinforcement ratios, ρ_{vf}, from *0.16%* to *1.5%*; vertical web reinforcement ratios, ρ_{vw}, from *0.23%* to *2.0%*, axial load levels, $\frac{N}{f_c' A_g}$, from *0.018* to *0.24*, concrete compressive strengths, f'_c, from *30MPa* to *50MPa*, flange/boundary element areas to gross cross-sectional areas, A_f/A_g, from *0.25* to

0.46, and aspect ratios, h_w/l_w, from *2.2* to *11.25*. The vertical reinforcement ratios of the latter walls were represented by ρ_{vf} and ρ_{vw} to investigate the influence of each parameter on the ductility of the walls, as recommended by previous relevant studies (e.g., Preti and Giuriani 2011; Sritharan et al. 2014). Flanged and boundary element walls were also merged in the same dataset because both wall configurations have shown similar responses in previous experimental tests (e.g., Gulec et al. 2009) in terms of their displacement ductility capacities.

The developed analytical model was used to perform pushover analyses on the *training* dataset and the load-displacement relationship of each wall was idealized to determine the displacement ductility, μ_Δ^{id}. Afterward, the geometrical/design parameters and the corresponding displacement ductility, μ_Δ^{id}, value of each wall were combined via the Design Expert statistical software *V13* (2020), through the inverse linear regression technique, in order to generate two data-driven expressions that can predict the displacement ductility of *RC* shear walls with rectangular (Eq. 4.16) and flange/boundary element (Eq. 4.17) configurations.

$$\mu_\Delta^{id} = [11.24(\rho_v) + 1.17\left(\frac{N}{f_c' A_g}\right) - 1.24 \times 10^3(f_c') - 1.57\left(\frac{b_w}{l_w}\right) + 8.19 \times 10^{-3}\left(\frac{h_w}{l_w}\right) + 0.19]^{-1} \quad \{R^2 = 0.92\} \tag{4.16}$$

$$\mu_\Delta^{id} = [8.07(\rho_{vf}) + 7.42(\rho_{vw}) + 0.57\left(\frac{N}{f_c' A_g}\right) - 4.10 \times 10^{-4}(f_c') - 0.26\left(\frac{A_f}{A_g}\right) + 6.92 \times 10^{-3}\left(\frac{h_w}{l_w}\right) + 0.22]^{-1} \quad \{R^2 = 0.90\} \tag{4.17}$$

As shown in Eq. 4.16 and Eq. 4.17, the coefficient of determination, R^2, are *0.92* and *0.90* for walls with rectangular and flange/ boundary element configurations,

respectively. Therefore, the data-driven expressions can accurately predict the displacement ductility values of *RC* walls with design parameters falling within the ranges of the *training* dataset, as shown in Figure 4.9.

4.5.1 Experimental Validation

To verify the effectiveness of the developed expressions, ten walls tested in previous experimental programs under fully-reversed cyclic loading were used to experimentally validate Eq. 4.16 and Eq. 4.17. These ten walls were selected as a *testing* dataset because they were not originally used during the development of both the analytical model and the two data-driven expressions presented in Eq. 4.16 and Eq. 4.17. Three rectangular walls (*RW-A20-P10-S38*, *RW-A20-P10-S64*, and *R1*) tested by Tran and Wallace (2012) and Oesterle et al. (1979), two flanged walls (*F1* and *F2*) tested by Oesterle et al. (1979), five boundary element walls (*H-1.4-No.25*, *H-1.4-No.33*, *B3*, *B5*, and *B8*) tested by Esaki (1994) and Oesterle et al. (1979), were all used, as presented in Table 4.6. The experimental load-displacement envelopes of the ten walls were idealized in the push (+ve) and pull (-ve) directions and their corresponding displacement ductility values were then computed in both loading directions, as shown in Table 4.6. As can be seen in the table, the predicted displacement ductility values based on Eq. 4.16 and Eq. 4.17 can closely capture their experimental counterparts, where the maximum deviation between the expression and experimental values is *8.5%*, *12.6%*, and *10.1%* for walls with rectangular, flange, and boundary element configurations, respectively. These results demonstrate that the two

expressions can well predict the experimental displacement ductility capacities of *RC* shear walls with different configurations.

4.6 INTERPRETABILITY OF EXPRESSIONS

This section evaluates the displacement ductility predictions when different input geometrical and design parameters are adopted. The interpretability of the data-driven expressions can be then assessed by comparing their predictions relative to the known mechanics of *RC* shear walls (Kuo et al. 2009; Gondia et al. 2020).

The analysis results for the rectangular walls and the flanged/boundary element walls are shown in Figures 4.10 and 4.11, respectively. These figures were developed by changing one input parameter only while all other parameters were kept constant at their mean values based on the generated dataset. As can be seen in the figures, for both wall configurations, the results show that the vertical reinforcement ratio (Figures 4.10a, 4.11a, and 4.11b), axial load level (Figures 4.10b and 4.11c), and aspect ratio (Figures 4.10e and 4.11f) are inversely proportional to the predicted displacement ductility values, while the concrete compressive strength (Figures 4.10c and 4.11d) is directly proportional to the displacement ductility predictions. The ratio of the thickness to the length for rectangular walls (Figure 4.10d) and the ratio of the flange/boundary element areas to gross cross-sectional areas (Figure 4.11e) are also directly proportional to the predicted displacement ductility values. These analysis results agree with the known behavior of mechanics, observations reported following previous earthquakes (e.g., the Maule Earthquake 2010),

and experimental findings based on walls tested by different researchers (e.g., Zhang and Wang 2000; Shedid et al. 2010; Carpenter et al. 2011; Burgueño et al. 2014).

To provide further understanding pertaining to the effect of each input parameter on the data-driven expressions, Eq. 4.18 and Eq. 4.19 were used (Gandomi et al. 2013; Gondia et al. 2020)

$$\Delta\mu_{\Delta}^{id} = \mu_{\Delta max}^{id}(x_i) - \mu_{\Delta min}^{id}(x_i) \qquad (4.18) \quad \& \quad S_i = \frac{\Delta\mu_{\Delta}^{id}}{\sum_{i=1}^{n}\Delta\mu_{\Delta}^{id}}\, x100 \quad (4.19)$$

where $\mu_{\Delta max}^{id}(x_i)$ and $\mu_{\Delta min}^{id}(x_i)$ are the maximum and minimum ductility values resulting from the analysis performed earlier for each parameter, respectively.

The analysis results are shown in Figures 4.12 (a and b) for the rectangular and the flanged/boundary element walls, respectively. The figures show that the vertical reinforcement ratio and axial load level are the most effective parameters for the displacement ductility predictions, followed by the aspect ratio, the thickness-to-length ratio for rectangular walls and flange/boundary element areas to gross-cross sectional areas, as shown in Figures 4.12 (a and b). While the concrete compressive strength is the least effective parameter to the predicted displacement ductility values, as shown in the same figures. The interpretability results (Figures 4.10, 4.11, and 4.12) coupled with the experimental validation results (Table 4.6) confirm that developed data-driven displacement ductility expressions are robust to be directly implemented in future editions of relevant design standards.

4.7 CONCLUSIONS

The current study developed an analytical model to simulate the seismic response of reinforced concrete (RC) shear walls with different configurations. The model was validated against the results of several walls tested in previous experimental programs under fully-reversed cyclic loading. The analytical and experimental results were compared in terms of the extent of plasticity, reinforcement strains and load-displacement relationships, stiffness degradation trends, and displacement ductility values. The results can be concluded as:

- The analytical curvature profiles were in good agreement with their experimental counterparts for rectangular, flanged, and boundary element walls. The model also accurately captured the experimental plastic hinge length with a maximum deviation of *5.1%* for all walls.
- The analytical and experimental load-strain results showed an acceptable agreement for all walls.
- The analytical model closely estimated the yield displacement, ultimate displacement, and ultimate load of the walls with maximum deviations of *16.0%*, *15.9%*, and *14.1%*, respectively. Overall, the experimental load-displacement envelopes of the walls were well captured by the analytical model.
- The model was able to estimate the experimental displacement ductility values of the walls with a maximum deviation of *13.7%.*

Following the model development and validation, *40* rectangular *RC* walls and *53* flanged/boundary element *RC* walls were generated as a *training* dataset to develop two

data-driven displacement ductility expressions for both wall configurations. The two expressions considered a wide range of geometrical configurations and design parameters, including the vertical reinforcement ratio, axial load level, concrete compressive strength, thickness-to-length ratio, aspect ratio, and the ratio of the flange/boundary element area to the gross cross-sectional area of the wall. The two data-driven expressions were in good agreement with the *testing* dataset that comprised ten *RC* shear walls experimentally investigated by previous researchers, with a maximum deviation of *12.6%*. The interpretability analyses showed also that the two developed expressions were in agreement with the known response of mechanics, previous seismic events (Canterbury earthquake 2011 and Maule earthquake 2010), and other research findings. The analysis results showed that the vertical reinforcement ratio and the axial load level are the most effective parameters for the predicted displacement ductility values, followed by the aspect ratio, thickness-to-length ratio, and the flanged/ boundary element area to gross cross-sectional area, while the least effective parameter is the concrete compressive strength. Through the data-driven expressions presented in the current study, the displacement ductility and hence the performance of *RC* shear walls with different configurations in major seismic events can be accurately predicted, and therefore, such expressions can be adapted by standards committees and design engineers.

Appendix 4. Response 2000 inputs and outputs

This section presents a step-by-step guide that was used to develop the analytical model.

Step 1: Input material properties

Unconfined Concrete:

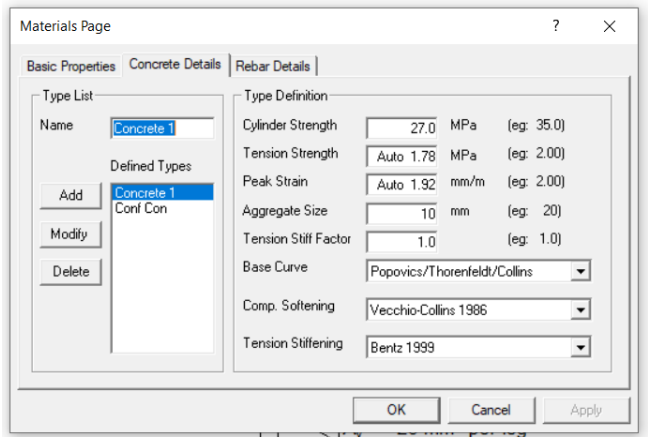

Confined Concrete:

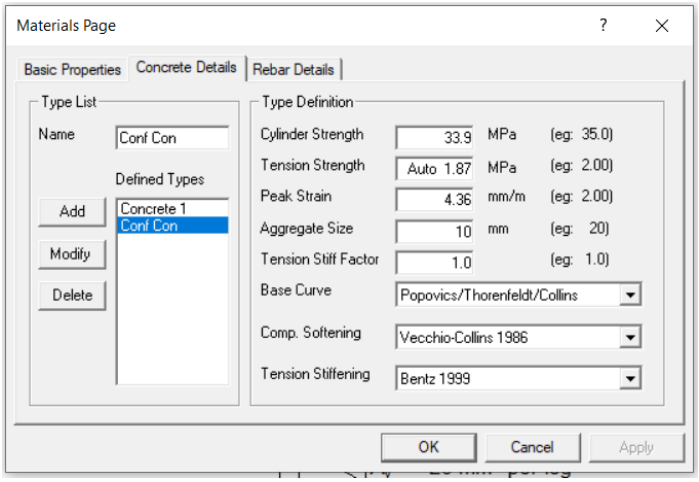

Rebar:

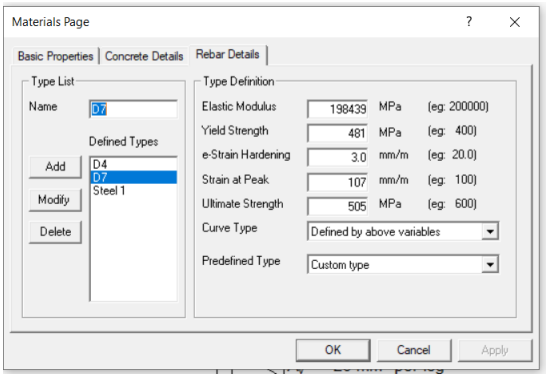

Step 2: Input wall dimensions, configurations and confined regions

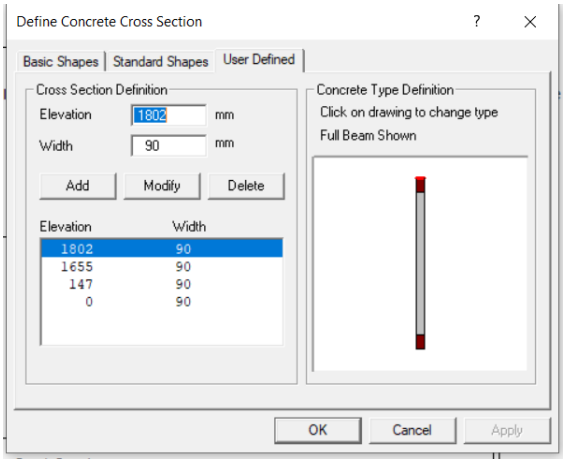

Step 3: Input vertical and horizontal rebars

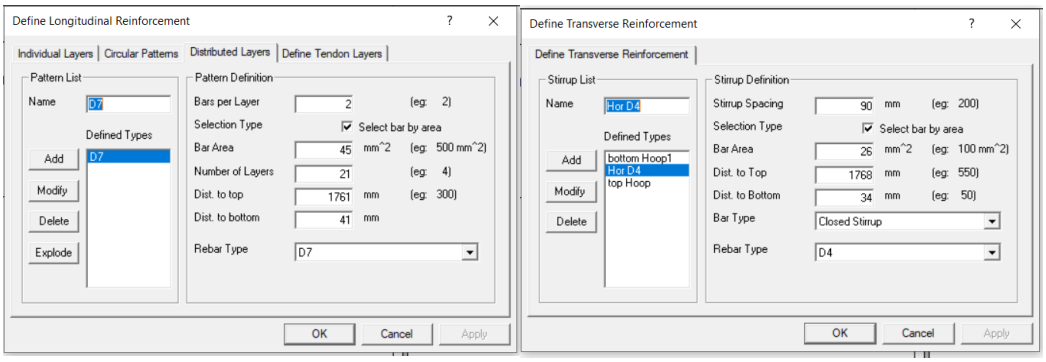

Step 4: Input height of the wall and the yield penetration factor

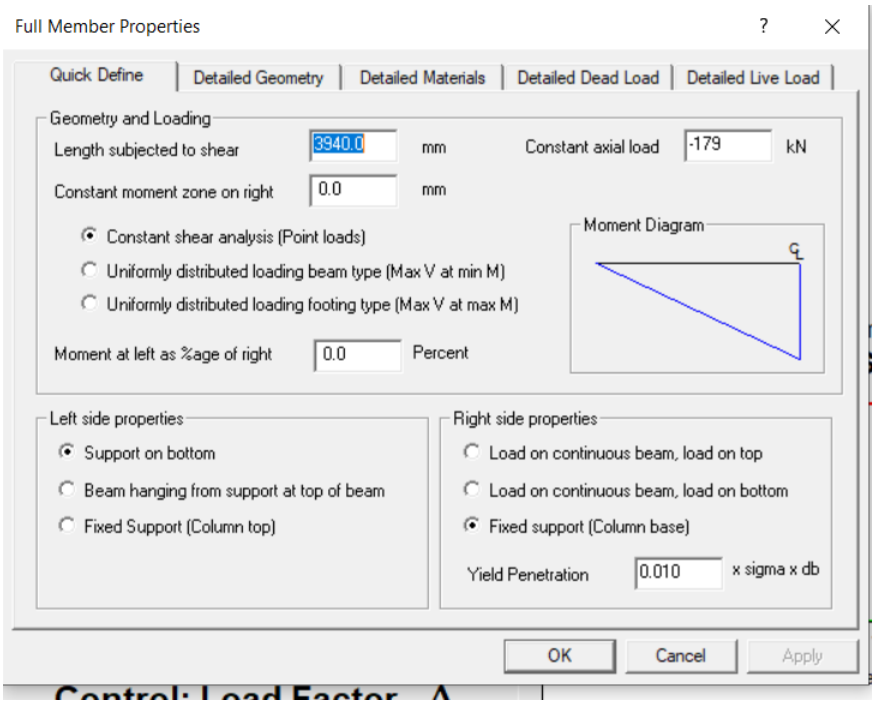

Step 5: Run the model

Step 6: Show the curvature profile

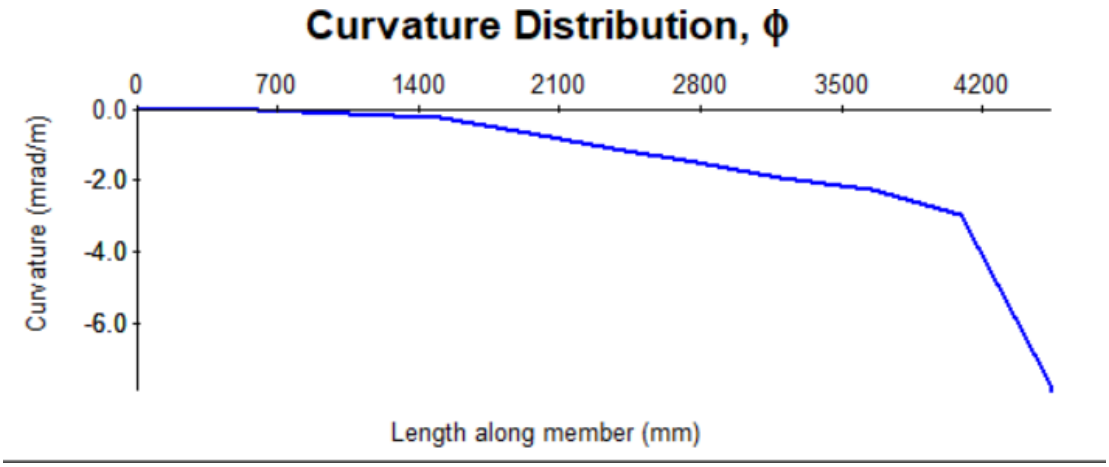

Step 7: Import Force- Strain relationship

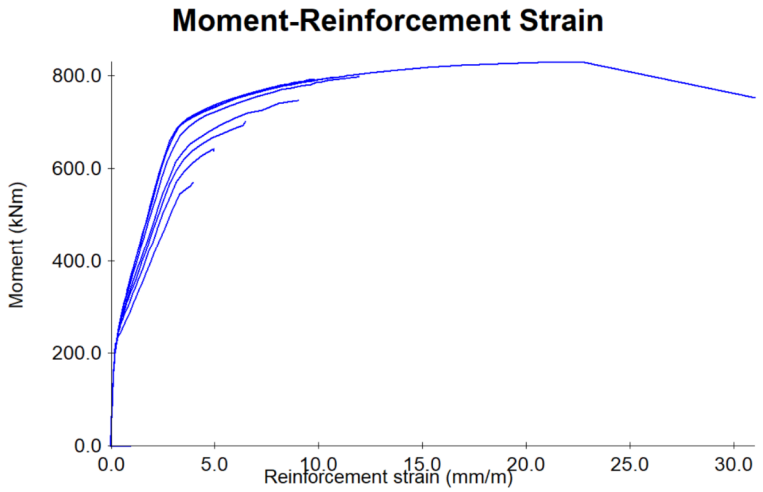

Step 8: Determine yield load when strain reaches yield, and then use the yield load to find the corresponding yield curvature

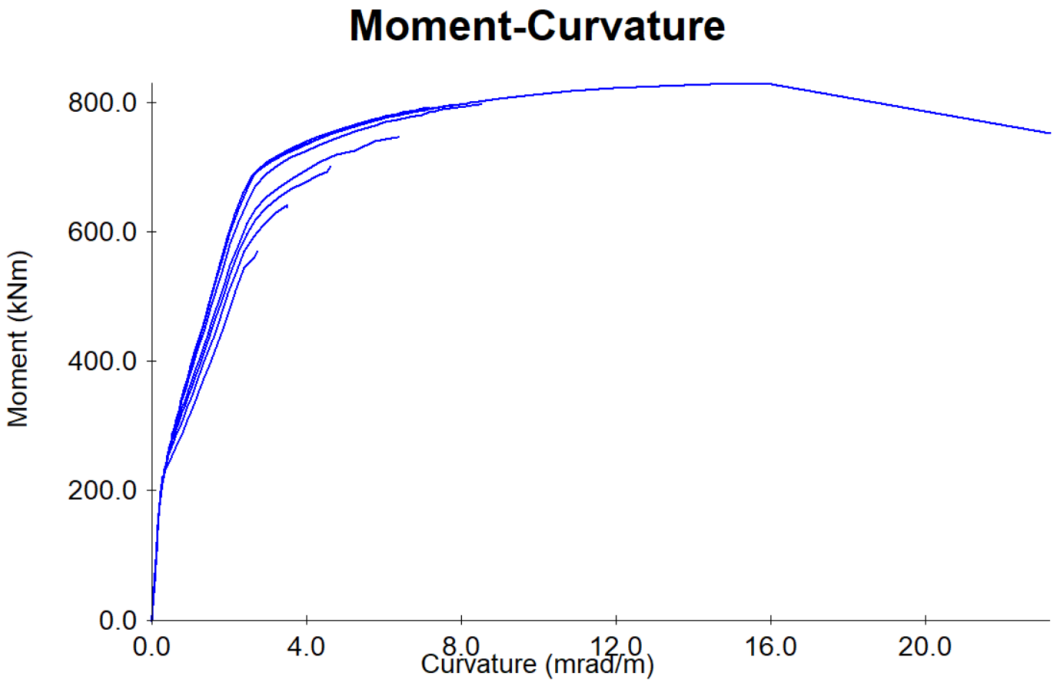

Step 10: Show the load-displacement relationship highlighted in the red box below

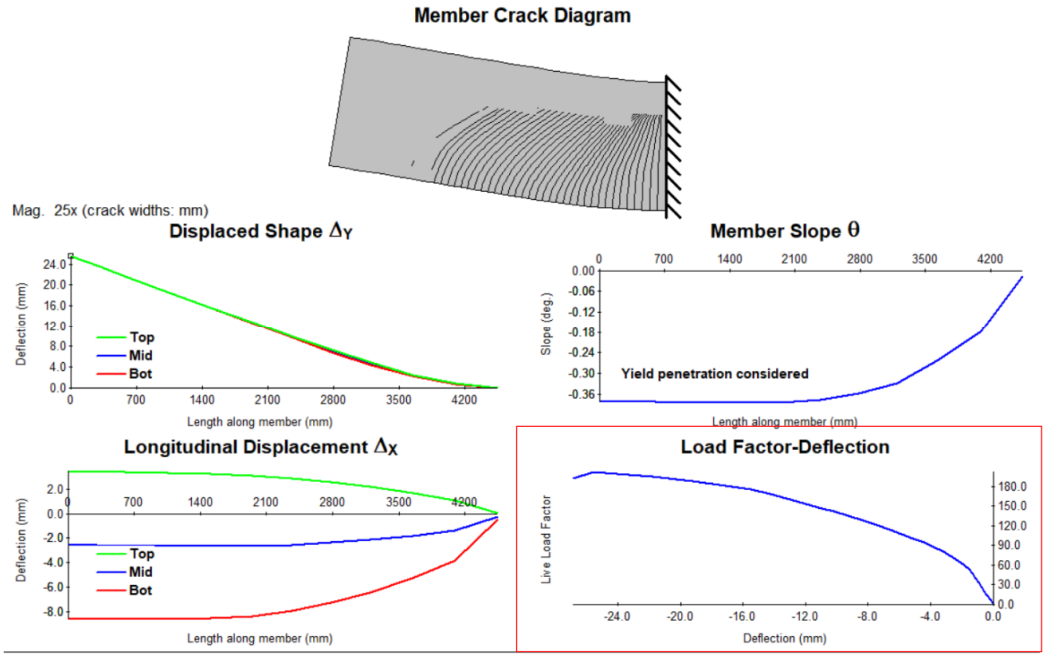

4.8 REFERENCES

American Society for Testing and Materials (ASTM), S. (2009). Standard specification for deformed and plain carbon-steel bars for concrete reinforcement. *ASTM A615/A615M-09b*.

Bentz, E. C. (2000). *Sectional analysis of reinforced concrete members* (p. 310). University of Toronto.

Bentz, E. C., & Collins, P. (2000). Response 2000, Reinforced Concrete Section Analysis using the Modified Compression Theory. *Toronto, University of Toronto*.

Burgueño, R., Liu, X., & Hines, E. M. (2014). Web crushing capacity of high-strength concrete structural walls: experimental study. *ACI Structural Journal*, *111*(2), 235.

Canadian Standards Association (CSA). (2019). *Design of concrete structures*. CSA A23.3-19, CSA, Mississauga, Canada.

Canterbury Earthquake Royal Commission report. (2011). *Seismic performance Christchurch building under the Canterbury Earthquake.* Retrieved Nov. 19th, 2019, http://canterbury.royalcommission.govt.nz/Final-Report-Volume-One-Contents

Carpenter, L. D., Naeim, F., Lew, M., Youssef, N. F., Rojas, F., Saragoni, G. R., & Adaros, M. S. (2011). Performance of tall buildings in Viña del Mar in the 27 February 2010 offshore Maule, Chile earthquake. *The Structural Design of Tall and Special Buildings*, *20*(1), 17-36.

Carrasquillo, R. L., Nilson, A. H., & Slate, F. O. (1981, May). Properties of high strength concrete subject to short-term loads. In *Journal Proceedings* (Vol. 78, No. 3, pp. 171-178).

Collins, M. P., & Mitchell, D. (1991). *Prestressed concrete structures* (Vol. 9). Englewood Cliffs, NJ: Prentice Hall.

El-Azizy, O. A., Shedid, M. T., El-Dakhakhni, W. W., & Drysdale, R. G. (2015). Experimental evaluation of the seismic performance of reinforced concrete structural walls with different end configurations. *Engineering Structures*, *101*, 246-263.

Esaki, F. (1994). Reinforcing effect of square steel tube on ductility of R/C framed shear wall whose predominant action is flexure. *Proceedings of the JCI*, *16*(2), 1325-1330.

Gandomi, A. H., Yun, G. J., & Alavi, A. H. (2013). An evolutionary approach for modeling of shear strength of RC deep beams. *Materials and structures*, *46*(12), 2109-2119.

Gondia, A., Ezzeldin, M., & El-Dakhakhni, W. (2020). Mechanics-guided genetic programming expression for shear-strength prediction of squat reinforced concrete walls with boundary elements. *Journal of Structural Engineering*, *146*(11), 04020223.

Gulec, C. K., and A. S. Whittaker. 2009. *Performance-based assessment and design of squat reinforced concrete shear walls*, 291. Buffalo, NY: MCEER.

Jiang, H., Wang, B., & Lu, X. (2013). Experimental study on damage behavior of reinforced concrete shear walls subjected to cyclic loads. *Journal of earthquake engineering*, *17*(7), 958-971.

Jünemann, R., Hube, M., De La Llera, J. C., & Kausel, E. (2012, September). Characteristics of reinforced concrete shear wall buildings damaged during 2010 Chile earthquake. In *Proceedings of the 15th World Conference of Earthquake Engineering*.

Kuo, Y. L., Jaksa, M. B., Lyamin, A. V., & Kaggwa, W. S. (2009). ANN-based model for predicting the bearing capacity of strip footing on multi-layered cohesive soil. *Computers and Geotechnics*, *36*(3), 503-516.

Oesterle, R. G., Aristizabal-Ochoa, J. D., Fiorato, A. E., Russell, H. G., & Corley, W. G. (1979). Earthquake resistant structural walls-tests of isolated walls-phase II. *Construction Technology Laboratories*, Portland Cement Association.

Park, R., & Paulay, T. (1991). *Reinforced concrete structures*. John Wiley & Sons.

Paulay, T., & Priestley, M. N. (1992). Seismic design of reinforced concrete and masonry buildings (Vol. 768). New York: Wiley.

Popovics, S. (1973). A numerical approach to the complete stress-strain curve of concrete. *Cement and concrete research*, *3*(5), 583-599.

Preti, M., & Giuriani, E. (2011). Ductility of a structural wall with spread rebars tested in full scale. *Journal of Earthquake Engineering*, *15*(8), 1238-1259.

Priestley, M. J. N., Calvi, G.M., & Kowalsky, M. J., (2007). *Displacement-based seismic design of structures.* Pavia, Italy: IUSS Press,

Richart, F. E., Brandtzæg, A., & Brown, R. L. (1928). *A study of the failure of concrete under combined compressive stresses*. University of Illinois at Urbana Champaign, College of Engineering. Engineering Experiment Station.

Saatcioglu, M., & Razvi, S. R. (1992). Strength and ductility of confined concrete. *Journal of Structural engineering*, *118*(6), 1590-1607.

Shedid, M. T., Drysdale, R. G., & El-Dakhakhni, W. W. (2008). Behavior of fully grouted reinforced concrete masonry shear walls failing in flexure: Experimental results. *Journal of structural engineering*, *134*(11), 1754-1767.

Shedid, M. T., El-Dakhakhni, W. W., & Drysdale, R. G. (2010). Characteristics of rectangular, flanged, and end-confined reinforced concrete masonry shear walls for seismic design. *Journal of structural engineering*, *136*(12), 1471-1482.

Shedid, M. T., & El-Dakhakhni, W. W. (2014). Plastic hinge model and displacement-based seismic design parameter quantifications for reinforced concrete block structural walls. *Journal of Structural Engineering*, *140*(4), 04013090.

Standards New Zealand (NZS). (2006). *Concrete Structures Standard.* NZS 3101, NZS, Wellington, New Zealand.

State-Ease. *Design Expert Software Version 13 User Guide.* Stat-Ease, Inc., Minneapolis, USA, 2020.

Sritharan, S., Beyer, K., Henry, R. S., Chai, Y. H., Kowalsky, M., & Bull, D. (2014). Understanding poor seismic performance of concrete walls and design implications. *Earthquake Spectra*, *30*(1), 307-334.

Thomsen IV, J. H., & Wallace, J. W. (1995). *Displacement-based design of RC structural walls: experimental studies of walls with rectangular and T-shaped cross sections* (Vol. 6). Report No. CU/CEE-95.

Tomazevic, M. (1999). *Earthquake-resistant design of masonry buildings* (Vol. 1). World Scientific.

Tran, T. A., & Wallace, J. W. (2012). Experimental Study of the Lateral Load Response of Moderate Aspect Ratio Reinforced Concrete Structural Walls. *Report No. UCLA-SGEL 2012*, *12*.

Vecchio, F. J., & Collins, M. P. (1986). The modified compression-field theory for reinforced concrete elements subjected to shear. *ACI J.*, *83*(2), 219-231.

Wallace, J. W., Massone, L. M., Bonelli, P., Dragovich, J., Lagos, R., Lüders, C., & Moehle, J. (2012). Damage and implications for seismic design of RC structural wall buildings. *Earthquake Spectra*, *28*(1_suppl1), 281-299.

Zhang, Y., & Wang, Z. (2000). Seismic behavior of reinforced concrete shear walls subjected to high axial loading. *Structural Journal*, *97*(5), 739-750.

4.9 TABLES

Table 4.1: Walls specifications

Wall	Configuration		Wall Dimensions (mm)	Vertical Reinforcement		Horizontal Reinforcement		Axial stress (MPa)	Axial ($\% f'_c$)
				Number of bars and bar sizes	ρ_v (%)	Bar & spacing (mm)	ρ_h (%)		
W1	Rectangular	*Phase I El-Azizy et al. (2015)*	1,802 × 3,990 Length × height	42 D7	1.17	2D4at 90	0.64	1.09	3.85
W2	Flanged			16 D7 & 22 D4	0.66	2D4 at 110	0.53	0.89	3.15
W3	Boundary Elements			20 D7 & 18 D4	0.69	2D4 at 110	0.53	0.89	3.15
W4	Rectangular	*Phase II El-Azizy et al. (2015)*		64 D11	2.80	2D4 at 45	1.28	1.09	2.66
W5	Flanged			16 D11 & 44 D7	1.58	2D4 at 55	1.05	0.89	2.17
W6	Boundary Elements			20 D11 & 40 D7	1.63	2D4 at 55	1.05	0.89	2.17
RW1*	Rectangular	*Thomsen & Wallace (1995)*	1,219 × 3,658 Length × height	16#3bars & 8#2bars	1.12	2-#2@191	0.33	3.22	10.19
RW2*	Rectangular			16#3bars & 8#2bars	1.12	2-#2@191	0.33	3.04	6.96

**Note: The difference between RW1 and RW2 is the spacing of the horizontal hoops at the confined area as noted in Figure 3*

Table 4.2: Experimental and analytical plastic hinge length, l_p

			Plastic Hinge Length				
			Experimental		**Analytical**		**Deviation (%)**
Wall	**Configuration**		**l_p (mm)**	**l_p (%l_w)**	**l_p (mm)**	**l_p (%l_w)**	
W1	Rectangular	*Phase I El-Azizy et al. (2015)*	1211	67.2	1202	66.7	0.7
W2	Flanged		934	51.8	887	49.2	5.0
W3	Boundary Elements		809	44.9	844	46.8	4.3
W4	Rectangular	*Phase II El-Azizy et al. (2015)*	1652	91.7	1710	94.9	3.5
W5	Flanged		1191	66.1	1199	66.5	0.7
W6	Boundary Elements		1242	68.9	1305	72.4	5.1
RW1	Rectangular	*Thomsen & Wallace (1995)*	-	-	1354	111	-
RW2	Rectangular		-	-	1503	123	-

Table 4.3: Experimental and analytical lateral load, Q_u

				Ultimate Lateral Load Q_u		
Wall	**Configuration**		**Direction**	**Experimental (kN)**	**Analytical (kN)**	**Deviation (%)**
W1	Rectangular	*Phase I El-Azizy et al. (2015)*	+(ve)	230	211	8.3
			-(ve)	172*		22.7
W2	Flanged		+(ve)	187	184	1.6
			-(ve)	183		0.5
W3	Boundary Elements		+(ve)	176	189	7.4
			-(ve)	177		6.8
W4	Rectangular	*Phase II El-Azizy et al. (2015)*	+(ve)	336	378	12.5
			-(ve)	355		6.5
W5	Flanged		+(ve)	322	357	10.9
			-(ve)	313		14.1
W6	Boundary Elements		+(ve)	334	354	6.0
			-(ve)	313		13.1
RW1	Rectangular	*Thomsen & Wallace (1995)*	+(ve)	142	153	7.7
			-(ve)	148		3.4
RW2	Rectangular		+(ve)	158	156	1.3
			-(ve)	156		0.1

**Note: The ultimate lateral load of wall W1 in the pull (-ve) direction is excluded due to a construction error (El-Azizy et al. 2015)*

Table 4.4: Experimental and analytical: yield displacement, Δ_y, and ultimate displacement Δ_u

		Yield Displacement					**Ultimate Displacement**				
		Experimental		**Analytical**		**Deviation (%)**	**Experimental**		**Analytical**		**Deviation (%)**
Wall	**Direction**	***Δ_y (mm)***	***Drift (%)***	***Δ_y (mm)***	***Drift (%)***		***Δ_u (mm)***	***Drift (%)***	***Δ_u (mm)***	***Drift (%)***	
W1	+(ve)	8.3	0.21	9.6	0.24	15.7	32.5	0.82	33.2	0.83	2.1
	-(ve)						-	-			-
W2	+(ve)	8.7	0.22	8.5	0.21	2.3	-[a]	-[a]	31.5	0.79	-
	-(ve)						31.4	0.79			0.3
W3	+(ve)	8.3	0.21	8.9	0.22	7.2	35.2	0.88	34.3	0.86	2.6
	-(ve)						33.2	0.83			3.3
W4	+(ve)	10.9	0.27	12.5	0.31	14.7	43.0	1.08	38.1	0.96	11.4
	-(ve)						45.3	1.14			15.9
W5	+(ve)	9.1	0.23	9.7	0.24	6.6	-[b]	-[b]	44.1	1.11	-
	-(ve)						46.0	1.15			4.1
W6	+(ve)	10.5	0.26	11.1	0.28	5.7	53.1	1.33	50.3	1.26	5.3
	-(ve)						53.3	1.34			5.6
RW1	+(ve)	13.1	0.36	15.2	0.42	16.0	69.1	1.89	65.7	1.80	4.9
	-(ve)						64.9	1.77			1.2
RW2	+(ve)	14.8	0.41	15.3	0.42	3.4	85.0	2.24	83.6	2.28	1.7
	-(ve)						83.2	2.28			0.5

[a]*Note: The ultimate displacement of wall W2 in the push (+ve) direction is not included because of premature failure due to localized damage at the wall-foundation interface (El-Azizy et al. 2015)*

[b]*Note: The ultimate displacement of wall W5 in the push (+ve) direction is not included due to foundation cracking (El-Azizy et al. 2015)*

Table 4.5: Experimental and analytical idealized displacement ductility, μ_{Δ}^{id}

				Displacement Ductility μ_{Δ}^{id}		
Wall	**Configuration**		**Direction**	**Experimental**	**Analytical**	**Deviation (%)**
W1	Rectangular	*Phase I El-Azizy et al. (2015)*	+(ve)	2.96	2.78	6.1
			-(ve)	2.54		9.4
W2	Flanged		+(ve)	-[a]	3.00	-
			-(ve)	3.06		2.0
W3	Boundary Elements		+(ve)	3.22	3.26	1.2
			-(ve)	3.29		0.9
W4	Rectangular	*Phase II El-Azizy et al. (2015)*	+(ve)	2.26	2.02	10.6
			-(ve)	2.34		13.7
W5	Flanged		+(ve)	-[b]	3.62	-
			-(ve)	3.48		4.0
W6	Boundary Elements		+(ve)	3.44	3.48	1.2
			-(ve)	3.40		2.4
RW1	Rectangular	*Thomsen & Wallace (1995)*	+(ve)	3.48	3.47	0.3
			-(ve)	3.64		4.7
RW1	Rectangular		+(ve)	4.01	4.28	6.7
			-(ve)	4.20		1.9

[a]*Note: The ductility of wall W2 in the push (+ve) direction is not included because of premature failure due to localized damage at the wall-foundation interface (El-Azizy et al. 2015)*

[b]*Note: The ductility of wall W5 in the pull (+ve) direction is not included due to foundation cracking (El-Azizy et al. 2015)*

Table 4.6: Experimental validation of displacement ductility predictions

			Displacement Ductility μ_{Δ}^{id}				
			Experimental		**Expression**	**Deviation (%)**	
Walls	**Source**	**Configuration**	**+ve**	**-ve**		**+ve**	**-ve**
RW-A20-P10-S38	*Tran & Wallace (2012)*	Rectangular	4.93	4.83	4.51	8.5	6.6
RW-A20-P10-S64	*Tran & Wallace (2012)*	Rectangular	2.73	2.79	2.57	5.9	7.9
R1	*Oesterle et al. (1979)*	Rectangular	7.04	7.10	7.57	7.5	6.6
F1	*Oesterle et al. (1979)*	Flanged	3.34	3.45	3.74	12.0	8.4
F2	*Oesterle et al. (1979)*	Flanged	3.34	3.47	3.76	12.6	8.4
H-1.4-No.25	*Esaki (1994)*	Boundary Element	3.06	3.09	3.07	0.3	0.7
H-1.4-No.33	*Esaki (1994)*	Boundary Element	2.80	2.70	2.87	2.5	6.3
B3	*Oesterle et al. (1979)*	Boundary Element	8.38	8.26	7.53	10.1	8.8
B5	*Oesterle et al. (1979)*	Boundary Element	3.87	3.81	3.92	1.3	2.9
B8	*Oesterle et al. (1979)*	Boundary Element	3.56	3.46	3.28	7.9	5.2

4.10 FIGURES

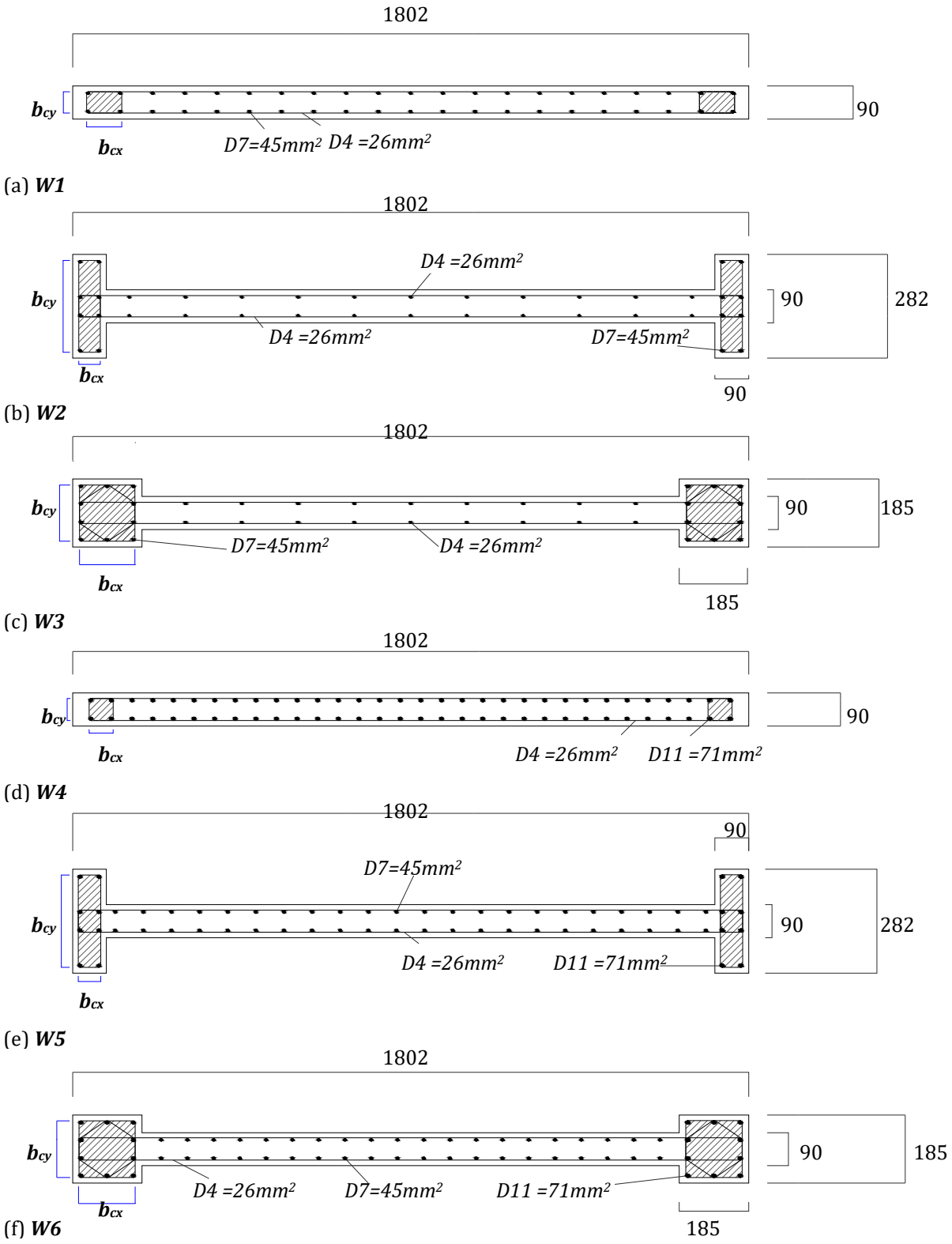

Figure 4.1: Walls configurations and reinforcement details (El-Azizy et al. 2015)

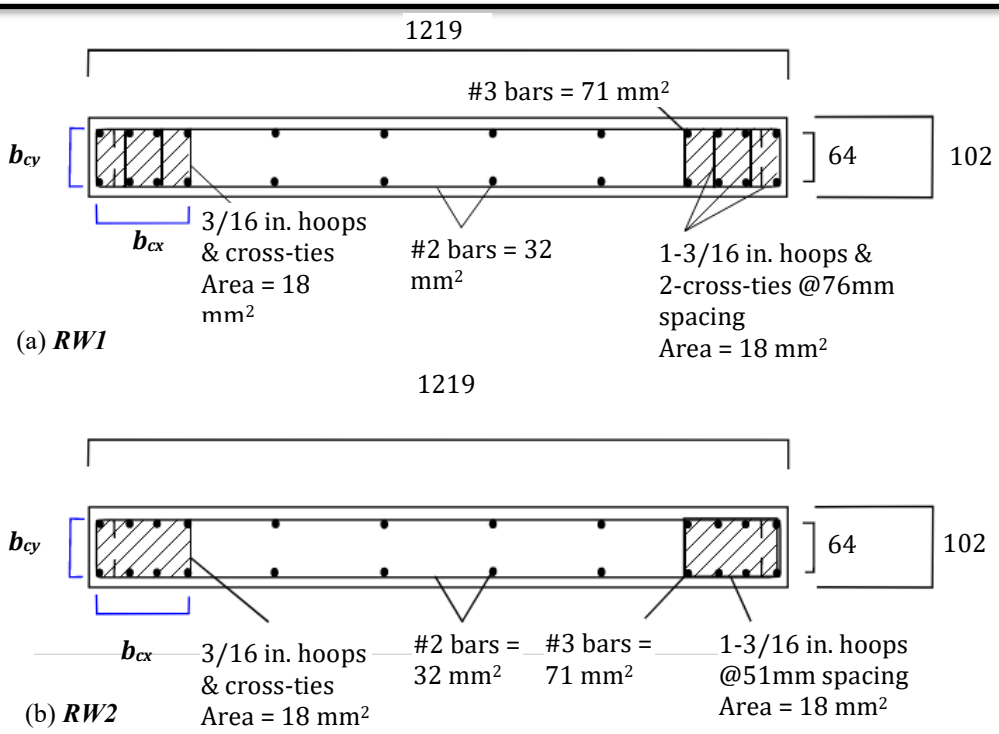

Figure 4.2: Rectangular wall configurations and reinforcement details (a) RW1; and (b) RW2 (Thomsen and Wallace 1995)

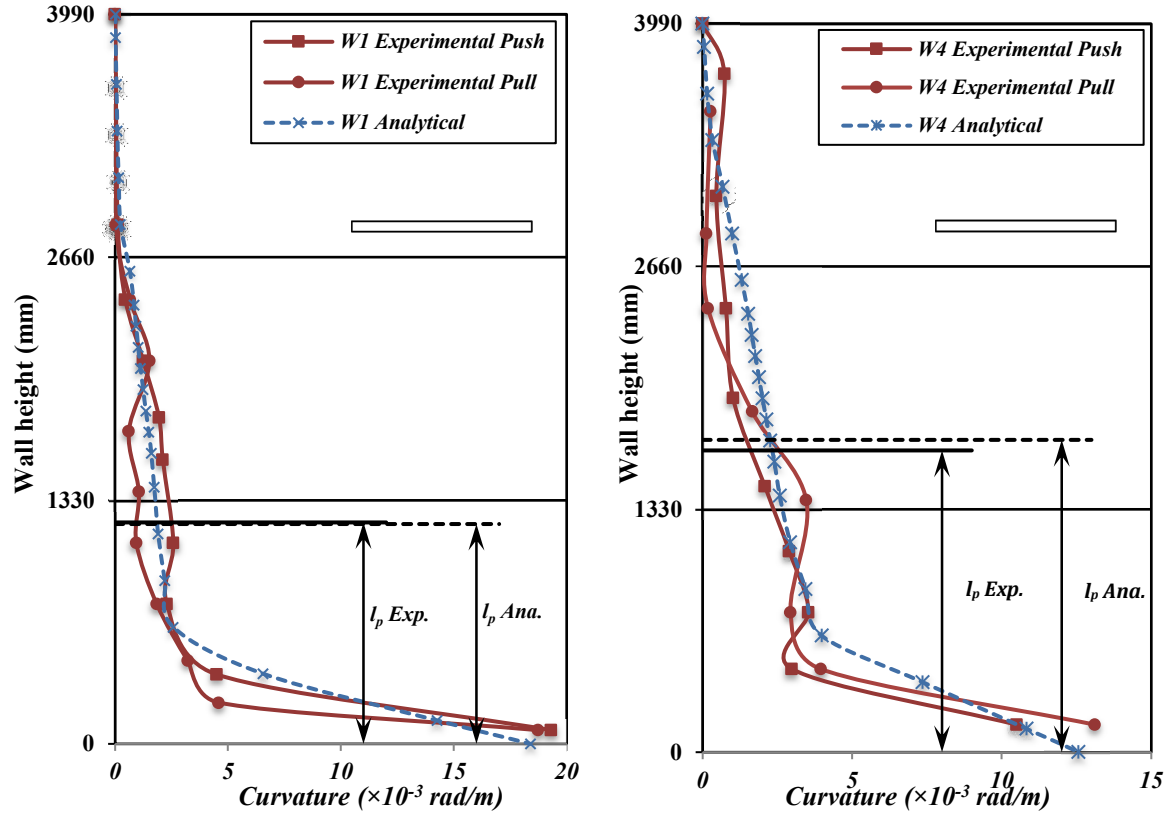

(a) *W1*

(b) *W4*

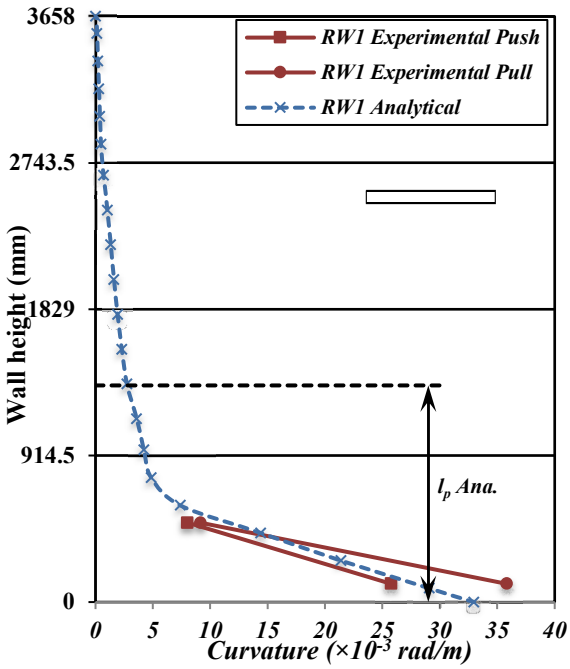

(c) *RW1*

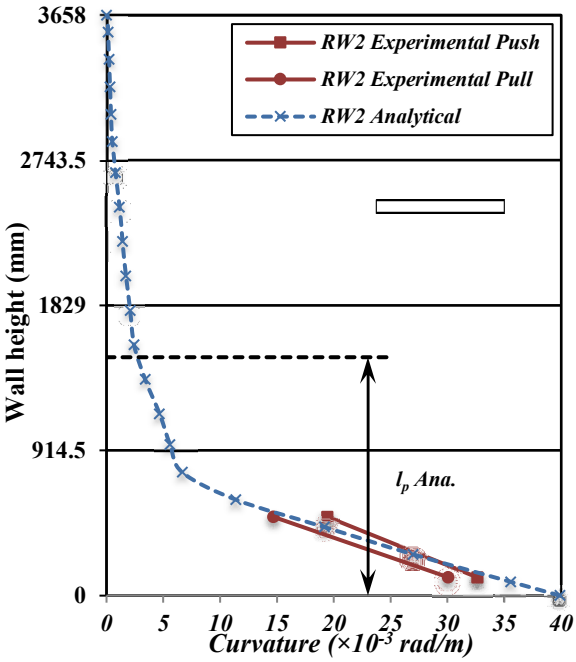

(d) *RW2*

Note: Thomsen and Wallace (1995) vertical potentiometers go up to 762 mm from the wall-foundation interface

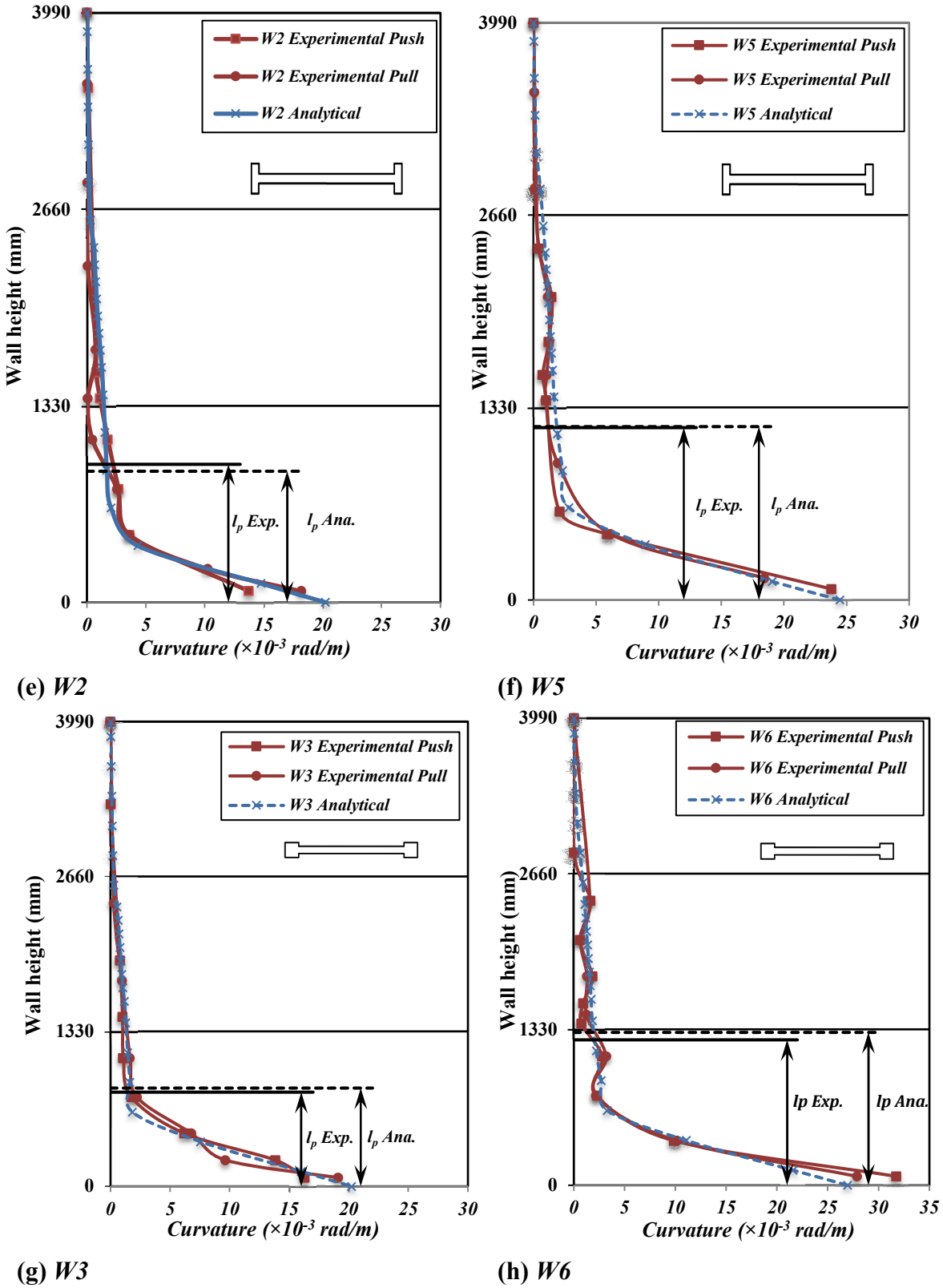

Figure 4.3: Experimental versus analytical curvature profiles:
Rectangular walls (a) *W1*, (b) *W4*, (c) *RW1* & (d) *RW2*; Flanged walls (e) *W2* & (f) *W5*;
Boundary Elements walls (g) *W3* & (h) *W6*

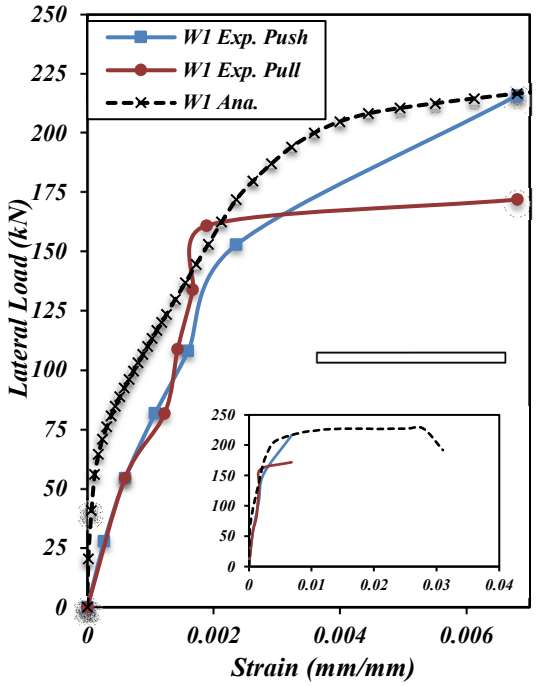

(a) *W1*

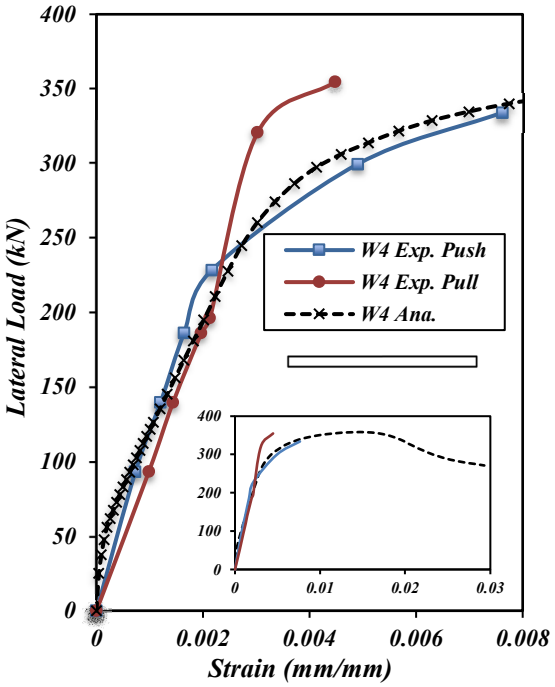

(b) *W4*

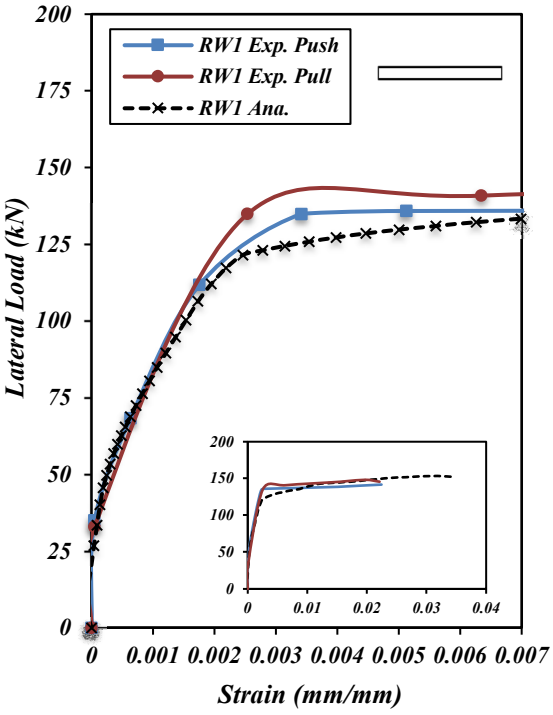

(c) *RW1*

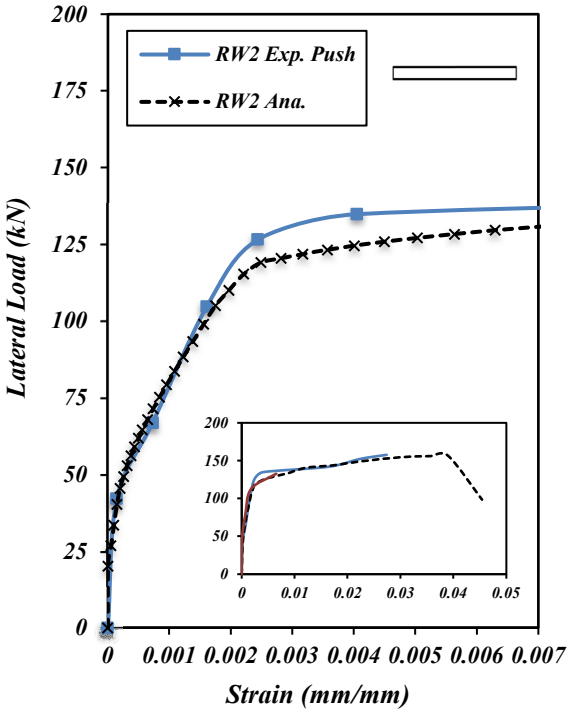

(d) *RW2*

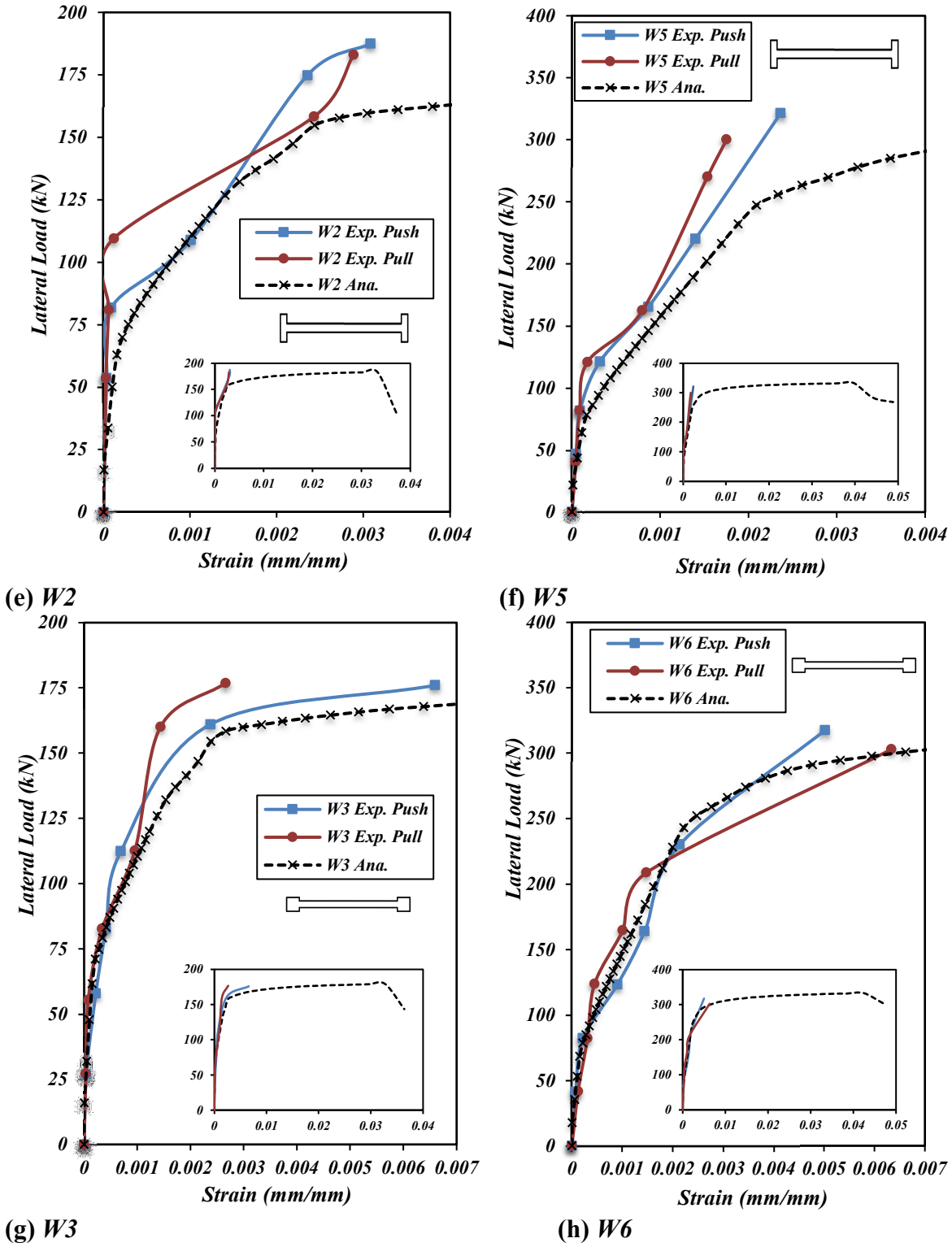

Figure 4.4: Experimental versus analytical outermost vertical reinforcement strains: Rectangular walls (a) *W1*, (b) *W4*, (c) *RW1* & (d) *RW2*; Flanged walls (e) *W2* & (f) *W5*; Boundary Elements walls (g) *W3* & (h) *W6*

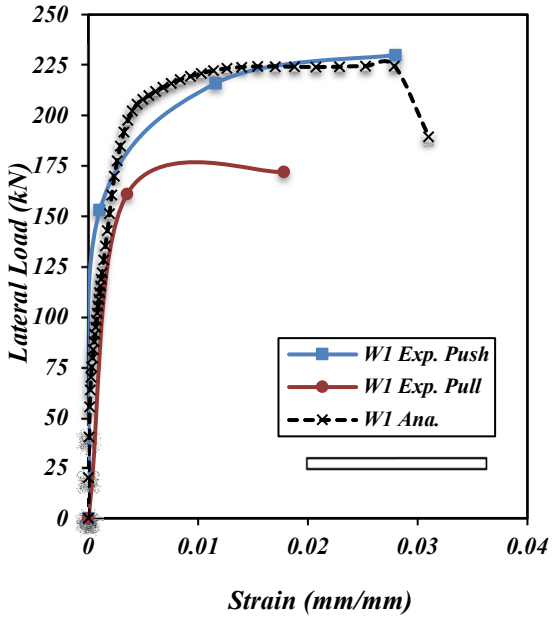

(a) *W1*

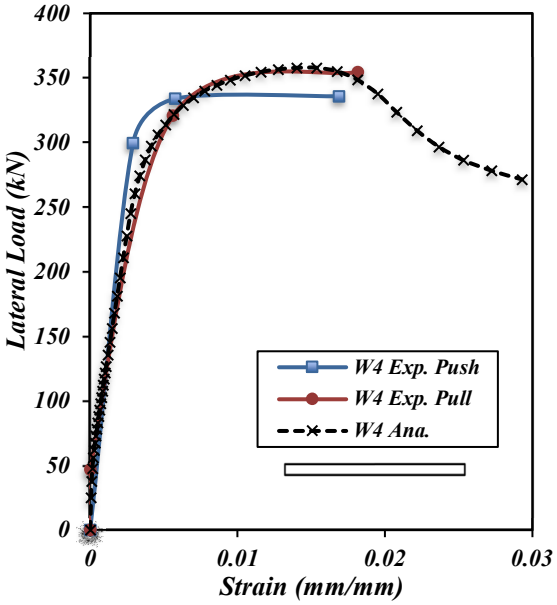

(b) *W4*

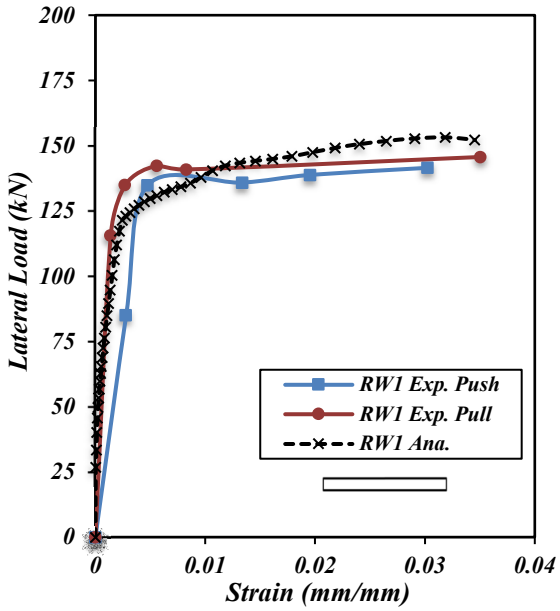

(c) *RW1*

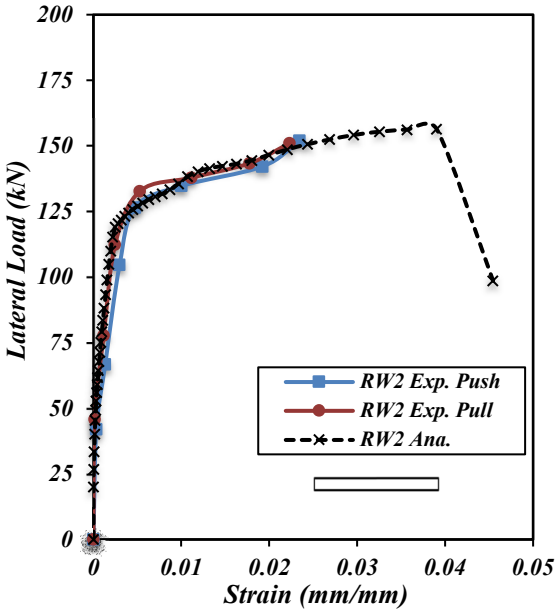

(d) *RW2*

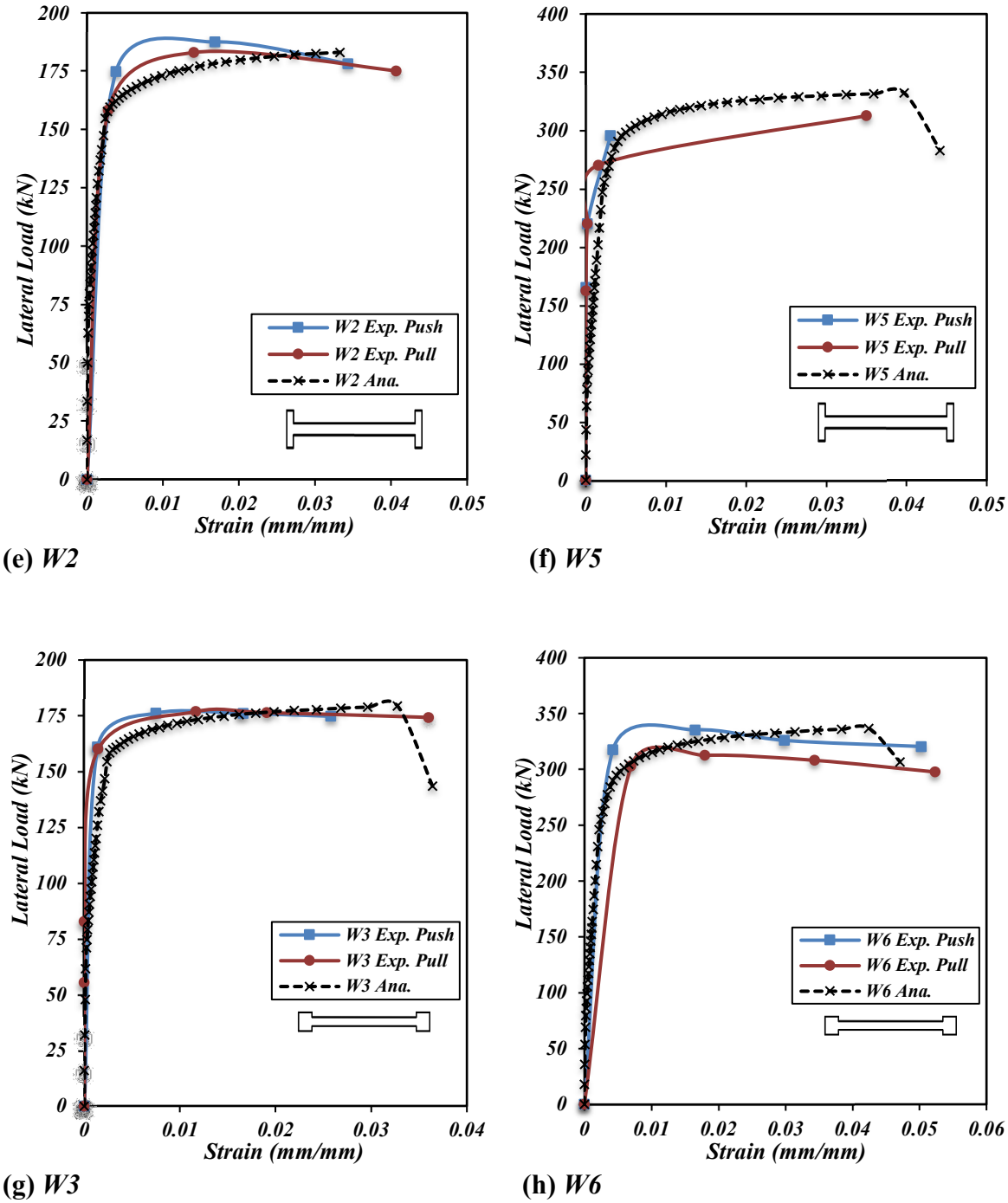

Figure 4.5: Experimental tensile strains versus analytical outermost vertical reinforcement strains: Rectangular walls (a) *W1*, (b) *W4*, (c) *RW1* & (d) *RW2*; Flanged walls (e) *W2* & (f) *W5*; Boundary Elements walls (g) *W3* & (h) *W6*

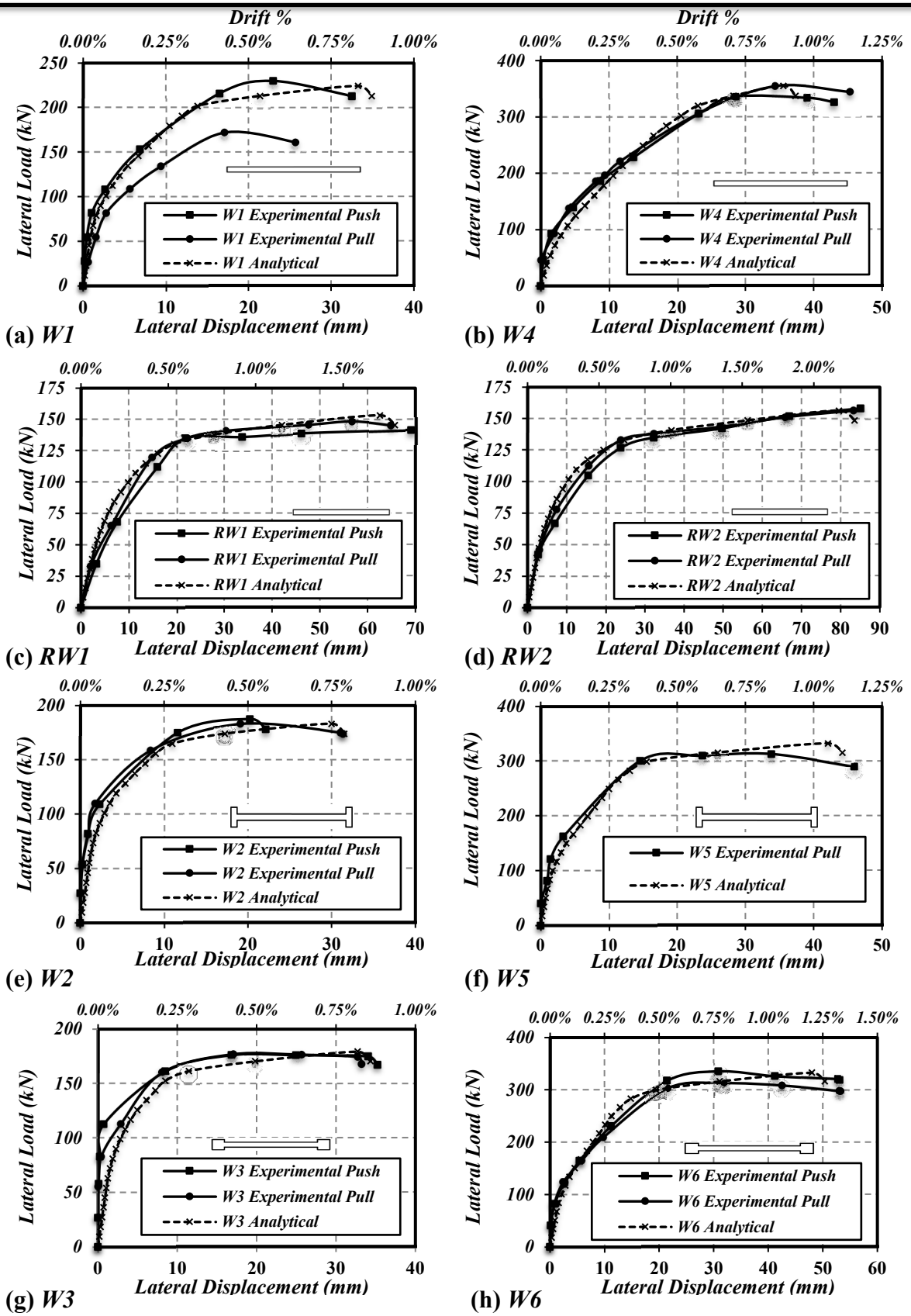

Figure 4.6: Experimental versus analytical load-displacement envelopes: Rectangular walls (a) *W1*, (b) *W4*, (c) *RW1* & (d) *RW2*; Flanged walls (e) *W2* & (f) *W5*; Boundary Elements walls (g) *W3* & (h) *W6*

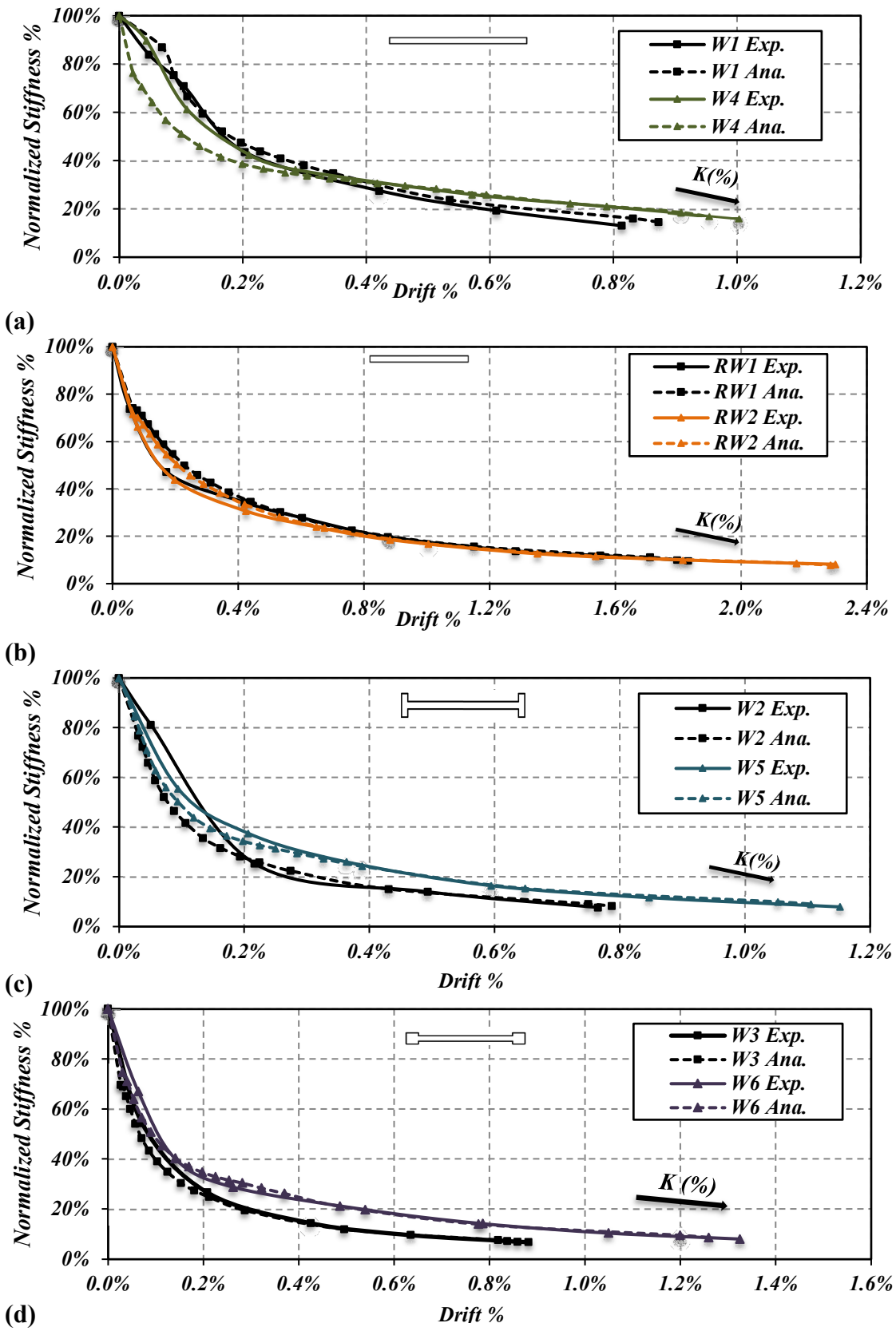

Figure 4.7: Experimental versus analytical normalized stiffness: Rectangular walls (a) *W1* & *W4* and (b) *RW1* & *RW2*; Flanged walls (c) *W2* & *W5*; Boundary Elements walls (d) *W3* & *W6*

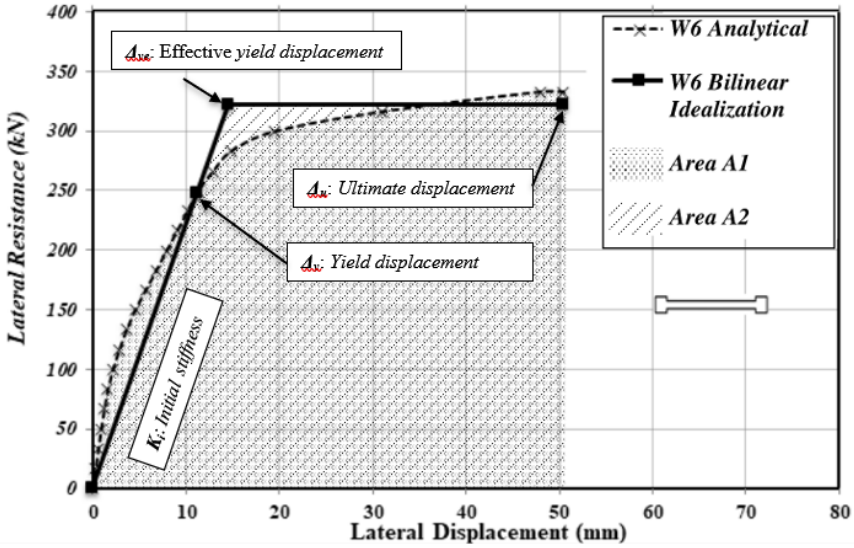

Figure 4.8: Bilinear idealization of the analytical load-displacement relationship for boundary element wall *W6*

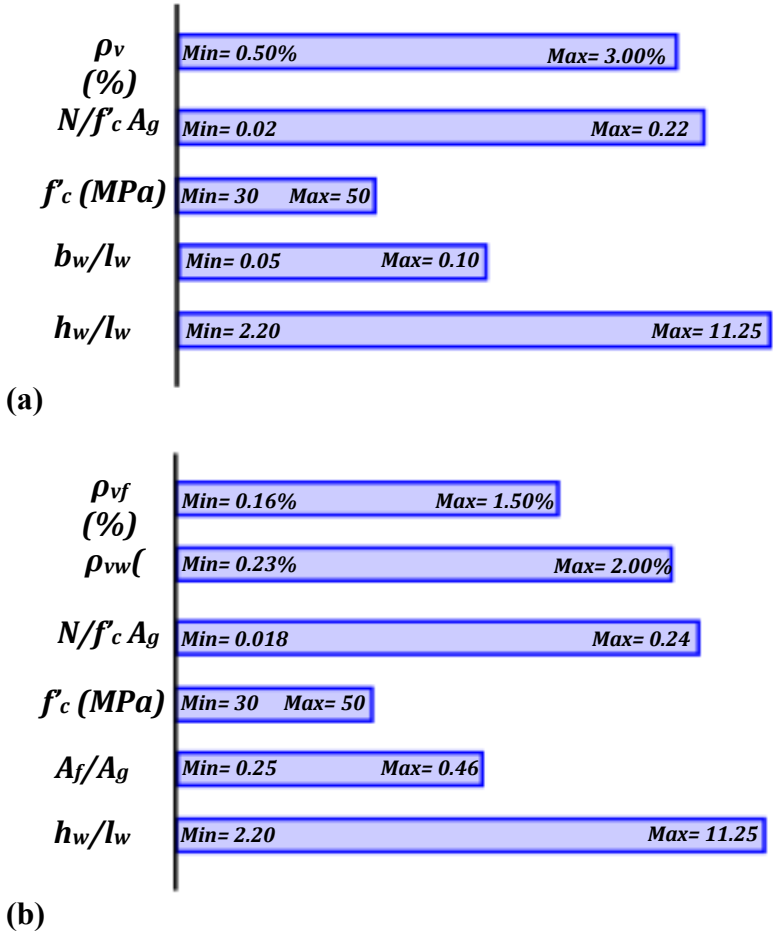

Figure 4.9: Parameter ranges within the *training* dataset
(a) Rectangular walls; (b) Flanged and boundary element walls

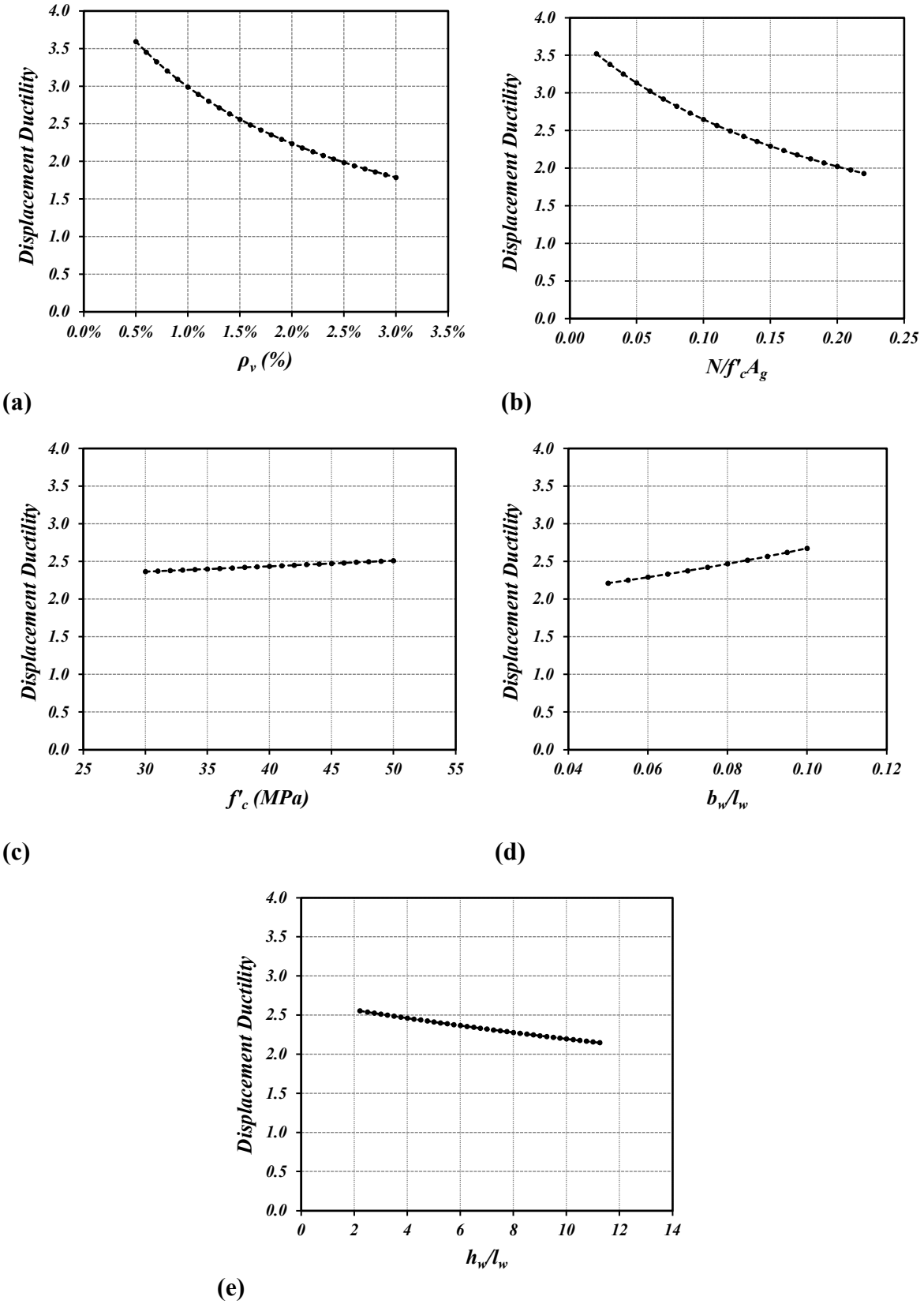

Figure 4.10: Displacement ductility values using the developed expression for rectangular walls (a) ρ_v *(%)*; (b) N/f'_cA_g; (c) f'_c (MPa); (d) b_w/l_w; (e) h_w/l_w

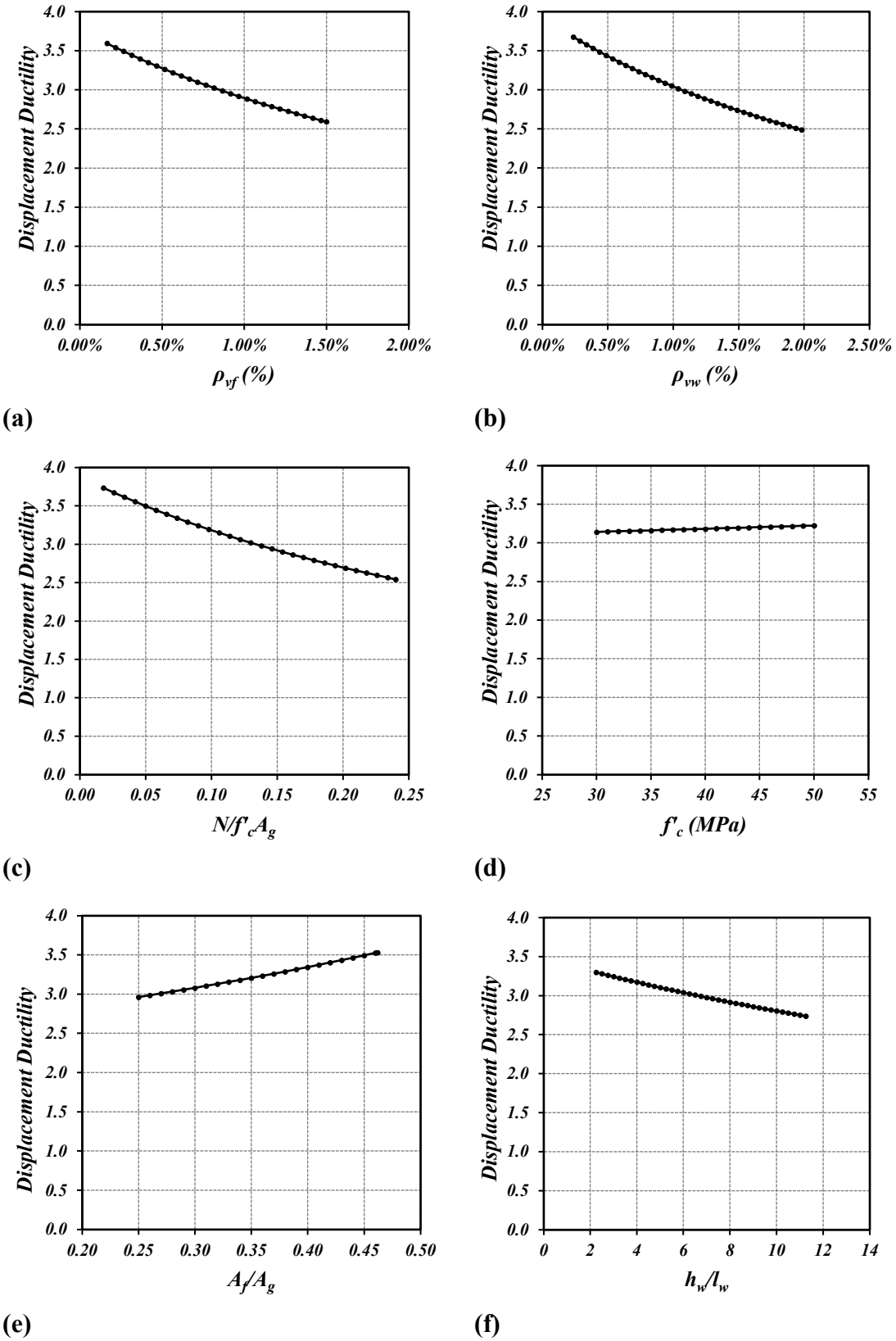

Figure 4.11: Displacement ductility values using the developed expression for flanged and boundary element walls (a) ρ_{vf} *(%)*; (b) ρ_{vw} *(%)*; (c) N/f'_cA_g; (d) f'_c (MPa); (e) A_f/A_g; (f) h_w/l_w

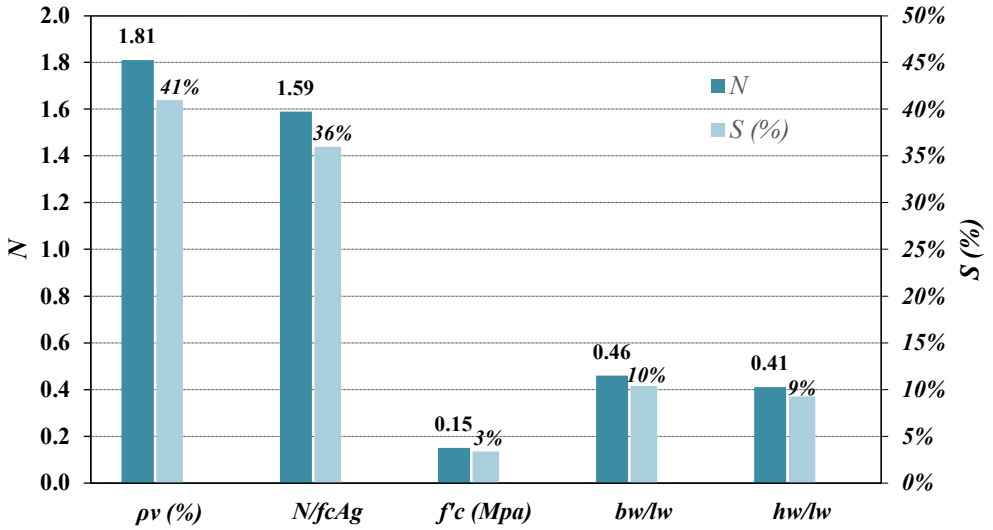

(a)

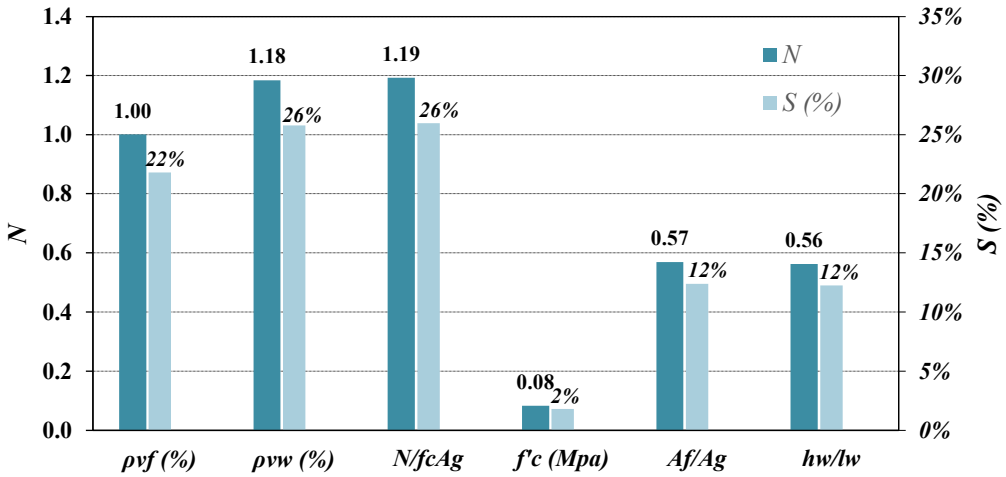

(b)

Figure 4.12: Analysis of input parameters in the developed expressions
(a) Rectangular walls; (b) Flanged and boundary element walls

CHAPTER 5
COMPARATIVE ANALYSIS OF REINFORCED MASONRY AND REINFORCED CONCRETE SHEAR WALLS WITH DIFFERENT END CONFIGURATIONS: SEISMIC PERFORMANCE AND ECONOMIC ASSESSMENT

5.1 ABSTRACT

Recent research has been demonstrating that fully-grouted reinforced masonry *(RM)* shear walls possess high ductile capacity levels that resulted in excellent performance under seismic loading. Considering the results of these studies, the current ductility modification factors assigned to such shear walls in relevant building codes and design standards are excessively conservative compared to the corresponding higher values assigned to ductile reinforced concrete (*RC*) counterparts. To address this, the objective of the current study is to show detailed comparative analyses between the performance of several *RC* and *RM* shear walls with different end configurations when both wall systems are subjected to similar seismic demands. In this respect, six half-scaled *RC* shear walls were compared to three half-scaled *RM* shear walls, where all nine walls were tested under a quasi-static cyclic fully-reversed loading. The six *RC* shear walls were tested in two phases, where each phase consisted of three different wall types (i.e., rectangular, flanged, and boundary element walls) that had identical dimensions to their *RM* counterparts. To allow for direct comparison between the walls, *Phase I RC* walls with low vertical reinforcement ratios had similar lateral strength capacities as the *RM* walls, whereas *Phase II RC* walls with high vertical reinforcement ratios had similar ultimate curvature values as the *RM* walls. The comparison results are presented in the current study in terms of the crack patterns, load-displacement envelopes, curvature profiles, and wall displacements. Displacement

ductility values, normalized periods, and equivalent viscous damping ratios are also presented for the nine walls. Finally, an economic assessment is performed to compare the walls in terms of their total rebar weights and approximate construction costs. The results demonstrate that *RM* shear walls can achieve an enhanced seismic performance similar to that of *RC* shear walls if the former walls are well-detailed (e.g., adequate confinement). Such an enhanced performance of *RM* shear walls is also coupled with low construction costs when compared to their *RC* counterparts. The current study enlarges the database of results that will facilitate assigning effective seismic performance metrics (e.g., ductility-related modification factors) for *RM* shear wall buildings in future editions of building codes and design standards.

5.2 INTRODUCTION

In high seismic regions, it is not economical to design shear walls to respond elastically. Therefore, displacement ductility, defined as the ability of the wall to deform beyond yielding with minor strength degradation, is a key parameter for seismic design. Specifically, walls capable of providing high ductility levels should be assigned higher seismic force reduction factors, when the force-based design approach is adopted, which is the case in several current building codes and design standards. In the National Building Code of Canada (NBCC 2020), the highest ductility modification factors, R_d, assigned for reinforced concrete *(RC)* and reinforced masonry *(RM)* ductile shear walls are *3.5* and *3.0*, respectively. Similarly, in the ASCE 7 (ASCE 2022), the response modification coefficients, R, are *6.0* and *5.5*, for special reinforced concrete shear walls and special

reinforced masonry shear walls, respectively. These typically lower values assigned for *RM* shear wall systems in the North American codes are due to the common perception that masonry systems cannot provide high ductility levels and subsequently they are less robust against seismic loading when compared to their *RC* counterparts.

Several research studies have been conducted on *RC* shear walls with various design parameters (e.g., reinforcement ratios, aspect ratios, cross-sectional properties, axial loads) to analyze their crack patterns, ductility levels, plastic hinge lengths, curvatures, stiffness degradation trends, equivalent viscous damping ratios, and the contributions of flexure and shear deformations to total deflections (e.g., Zhang et al. 2000; Massone and Wallace, 2004; Thomsen and Wallace 2004; Adebar et al. 2007; Ghorbanirenani et al. 2012; Luu et al. 2014; Christidis and Trezos 2017; Rong et al. 2020; Gondia et al. 2020; Akl and Ezzeldin 2023). Such studies, along with other observations during earthquake events (e.g., the 2010 Maule earthquake in Chile), demonstrated that several well-detailed *RC* shear walls showed low seismic performance due to their high out-of-plane slenderness ratios and high axial load levels (Jünemann et al. 2012). In addition, as documented in the Canterbury earthquake royal commission report (Canterbury Commission Report, 2011), several *RC* shear walls did not reach the expected seismic performance due to the concentration of plastic strains at the primary crack locations. Similarly, other researchers have tested *RM* components and systems to investigate their seismic performance through a wide range of design parameters (e.g., Eikanas 2003; Shedid et al. 2008; Shedid et al. 2010; Haach et al. 2010; Banting et al. 2012; Ahmadi et al. 2014; El Ezz et al. 2015; Siyam et al. 2016; Ezzeldin et al. 2017). The results showed that *RM* shear walls can achieve an

enhanced seismic performance if they are well-detailed through a sufficiently conservative and comprehensive set of prescriptive requirements, including the use of adequate masonry confinement strategies at the wall ends.

Due to the findings of such studies and the reconnaissance reports following the aforementioned earthquake events, it was intriguing to perform a study that directly compares the seismic performance of *RC* shear walls against well-detailed *RM* shear walls given the fact that the latter walls are typically assigned lower seismic performance factors than the former walls, as discussed earlier. In this respect, the current study presents a detailed comparative analysis between the performance of six *RC* shear walls and three *RM* shear walls when both wall systems are subjected to similar seismic demands. Specifically, six half-scaled *RC* shear walls with different end configurations (i.e., rectangular, flanged, and boundary element walls) tested by El-Azizy et al. (2015) were compared to three half-scaled *RM* shear walls tested by Shedid et al. (2010) with corresponding similar dimensions and end-configurations. To facilitate direct comparisons between the walls, *Phases I* and *II RC* walls had similar lateral strength capacities and ultimate curvature values as their *RM* counterparts, respectively. Following a summary of the experimental program and test results, the current study initially shows the comparative analysis between the *RC* and *RM* walls in terms of their crack patterns, load-displacement envelopes, and curvature profiles. The contributions of flexure, shear, and sliding deformations to the total displacement, displacement ductility values, normalized periods, and equivalent viscous damping ratios are then presented for the nine walls. Finally, an economic evaluation is performed to show

a comparison between the *RC* and *RM* walls in terms of their toral rebar weights and total construction costs.

5.3 SUMMARY OF THE EXPERIMENTAL PROGRAMS

Six *RC* (*RC1* to *RC6*) and three *RM* (*RM1* to *RM3*) half-scaled three-story shear walls were constructed and tested by El-Azizy et al. (2015) and Shedid et al. (2010), respectively. The *RC* walls were constructed and tested in two phases (i.e., *Phases I* and *II*), each phase contained rectangular (*RC1* and *RC4*), flanged (*RC2* and *RC5*), and boundary element (*RC3* and *RC6*) walls. Table 1 shows the vertical reinforcement ratio, ρ_v, horizontal reinforcement ratio, ρ_h, number of bars and sizes, and axial stress levels. As can be seen in the table and Figure 5.1, all the walls have the same overall dimensions (i.e., length and thickness) and walls with flanges and boundary elements have the same confined areas, thus facilitating a comparative analysis between the walls. *RC* walls were reinforced with scaled *D4*, *D7*, and *D11* with cross-sectional areas of $26mm^2$, $45mm^2$, and $71mm^2$, respectively, which are equivalent to *M10*, *M15* and *M20* ($100mm^2$, $200mm^2$ and $300mm^2$, respectively) full-scale rebars. *RM* walls were reinforced with scaled *D4* and full-scale *M10* rebars. The rebars used in the nine walls conform to *CSA G30.18-21* (CSA 2021) standards. Both wall types were also detailed as *Ductile* walls according to *CSA A23.3-19* (CSA 2019a) and *CSA S304.1-19* (CSA 2019b) for *RC* and *RM* walls, respectively. All walls were subjected to the same axial load of *160kN* via hydraulic actuators and an out-of-plane bracing system was provided to ensure in-plane loading throughout the tests, as shown in Figure 5.2.

Each wall was mounted with *38* and *36* displacement potentiometers, for *RC* and *RM* walls, respectively. The potentiometers were used to record axial and lateral displacements as well as any sliding displacements at the wall-foundation interface. Also, *14* and *8* strain gauges were attached to the outermost vertical bars of the *RC* and *RM* walls, respectively, to measure reinforcement strains throughout the loading history. The walls were subjected to a quasi-static fully-reversed cyclic loading at their top levels. The experimental results demonstrate that both wall systems (*RC* and *RM*) failed in a flexural ductile manner by crushing at the outer wall toes followed by buckling and then snapping of the outermost reinforcement bars. The tests were terminated when the lateral strength of the walls degraded to *50%* of their maximum capacities.

5.4 Analysis of Test Results

The current study compares the seismic performance between *RC* and *RM* shear walls by analyzing their crack patterns, load-displacement envelopes, curvature profiles, displacements, ductility capacities, normalized periods, and equivalent viscous damping ratios. As intended during the design stage of the nine walls, Table 5.2 confirms that *Phase I RC* walls (*RC1*, *RC2*, and *RC3*) have similar experimental lateral strength capacities as their *RM* counterparts (*RM1*, *RM2*, and *RM3*) with a maximum deviation of *17.5%* between *RC2* and *RM2*. Table 5.3 demonstrates also that *Phase II RC* walls (*RC4*, *RC5*, and *RC6*) and *RM* walls (*RM1*, *RM2*, and *RM3*) have similar experimental ultimate curvature values at *75mm* from the wall-foundation interface with a maximum deviation of *19.5%* between *RC5* and *RM2*. Such small deviations, which might be attributed to the material variability

associated with the construction during each wall and other limitations related to the location of rebars within the walls (e.g., placing rebars within standard spacings between masonry cells and courses), facilitate the comparative analysis between the *RC* and *RM* walls, as will be discussed in the following subsections.

5.4.1 Crack Patterns

Figure 5.3 shows the crack patterns at the first story of each wall at the end of the tests. As can be seen in Figures 5.3 (a, d, and g), *Phase I RC* walls (*RC1*, *RC2*, and *RC3*) exhibited only a few flexural cracks that turned into diagonal shear cracks at high displacement levels. At the upper stories of the same three walls, a few flexural cracks were visible at the bottom half of the second story and minimal hairline diagonal shear cracks were visible along the full length of the second and third stories. As shown also in Figures 5.3 (b, e, and h), *Phase II RC* walls (*RC4*, *RC5*, and *RC6*) exhibited extensive flexural and diagonal cracks at the first story. The second and third stories experienced relatively fewer diagonal shear cracks. For *Phases I* and *II*, at high displacement levels, the cracks propagated and increased in length and width till the crushing of the outermost wall toes and the buckling of the bars followed by the outermost bar snapping in the following load cycles.

RM walls (*RM1*, *RM2*, and *RM3*) exhibited diagonal shear cracks and flexural cracks, where most of the cracks followed the bed and head mortar joints of the walls, as can be seen in Figures 5.3 (c, f, and i). As the drift increased, flexural and diagonal shear cracks widened at the mortar joints. At high displacement levels, vertical cracks were visible at the wall corners followed by crushing in the compression toes and snapping in

the outermost tensile bars. The diagonal cracks were relatively less at the second story and very minimal cracks were visible at the third story.

As shown in Figure 5.3, *RM* walls showed a higher number of diagonal shear cracks when compared to *Phase I RC* walls. On the other hand, flexural cracks were higher in number for *RC Phase I* walls when compared to their *RM* counterparts. For flanged, *RC2*, and boundary element, *RC3*, walls, the flexural cracking was mostly hairline cracks, and one major primary crack was localized at the plastic hinge of each wall, while flexural cracks were distributed at the mortar joints of their *RM* counterparts and such cracks increased in width as the displacement level increased. When comparing *RM* walls with *Phase II RC* walls, Figure 5.3 shows that the cracks in *RC* walls were substantially more for both diagonal shear and flexural cracks. This latter observation might be attributed to the higher vertical reinforcement ratios of *Phase II RC* walls; however, this crack pattern did not overcome the benefits of having head and bed mortar joints which facilitated the development of cracks and the subsequent distribution of plastic strains along several masonry courses rather than concentrating the plastic hinges around the wall-foundation interfaces, which is the case for *RC* walls.

The crack patterns of both wall systems in Figure 5.3 demonstrate that the diagonal shear cracks in addition to the flexural cracks at the mortar joints contributed to the higher ultimate displacement levels achieved by the *RM* walls when compared to *Phase I* and *II RC* walls. Specifically, the results show that weak bed and head mortar joints of *RM* walls are key to achieving high displacement capacities with no/minimum strength degradation, as will be discussed next.

5.4.2 Load-Displacement Envelopes

Figure 5.4 shows the normalized load-displacement envelope for each wall. All walls reached yield at a similar drift ratio ranging from *0.21%-0.27%*. As can be seen in the figure and Table 5.4, all *RM* walls reached their maximum lateral strengths at higher drift ratios than their *RC* counterparts (i.e., except *RC4* and *RC5*). For example, the drift ratios of *RM1*, *RM2,* and *RM3* at their maximum lateral strengths are higher than those of *RC1*, *RC2,* and *RC3* by *26%*, *60%*, and *215%*, respectively. Figure 5.4 and Table 5.4 show also that high drift ratios are achieved by the *RM* walls beyond their maximum capacities while also maintaining their lateral strengths. For example, the ultimate drift (i.e., defined herein as the top lateral drift at *20%* strength degradation from the maximum lateral strength) of *RM1* is *30%* higher than that of *RC1*. *RM* walls with flanges and boundary elements showed also significantly high ultimate drifts when compared to their *RC* counterparts, where *RM2 and RM3* achieved higher ultimate drifts by *210%* and *250%* than *RC2* and *RC3* and by *30%* and *50%* than *RC5* and *RC6*, respectively, as presented in Table 5.4.

The higher ultimate drifts of *RM* walls compared to their *RC* counterparts can be attributed to the existence of mortar joints in the former walls. As in flexural, the mortar joints in the tensile regions opened spreading the plastic hinge over a few courses of *RM* walls rather than concentrating it at the bottom of *RC* walls. Also, diagonal shear cracks at the horizontal (bed) and vertical (head) mortar joints opened and contributed to the high ultimate drifts of *RM* shear walls when compared to *RC* shear walls that show hairline diagonal cracks which result in low ultimate drifts, as discussed earlier.

5.4.3 Curvature Profiles

Table 5.3 shows the experimental ultimate curvatures (i.e., at the maximum lateral strength of the wall) at *75mm*, *490mm,* and *775mm* from the wall-foundation interface, while Figure 5.5 shows the curvature profiles of *RC* walls of *Phases I* and *II* versus *RM* walls. As shown in Table 5.3 and Figure 5.4, the curvatures of the *RC* walls are concentrated at the bottom *225 mm* from the wall-foundation interface, while higher curvature values are achieved by the *RM* walls at higher elevation levels at *490mm* and *775mm* from the wall-foundation interface. For example, *RM1* achieved a lower ultimate curvature at *75mm* than *RC1* by *23%*; however, at *490mm* and *775mm*, the ultimate curvature values of *RM1* exceeded *RC1* by *61%* and *47%*, respectively. While *RM2* and *RM3* achieved higher ultimate curvature values when compared to *RC2* and *RC3*, by *62%* and *76%* at *75mm*; by *46%* and *308%* at *490mm*, and by *313%* and *345%* at *775mm*, respectively. As can be seen in Table 5.3, the differences in curvature values between the *RM* walls and *Phase II RC* walls at the different elevation levels are smaller, but the *RM* walls achieved in general higher curvatures along the first story when compared to their *Phase II RC* walls.

Based on the results presented in Table 5.3 and Figure 5.4, it can be concluded that *RM* walls have a better distribution of curvatures over the first story when compared to *RC* walls due to the weak mortar joints that initiate multiple plastic hinges along the height of the wall. It is also worth noting that the high curvatures achieved by *RM3* are due to the combination of the weak mortar joints that distributed the curvature over several courses and due to also the confinement of the four bars at the wall ends which enhanced the stress-strain relationship of the masonry within the wall.

5.4.4 Wall Displacements

Figure 5.6 shows the contributions of flexure, shear, and sliding displacements to the total displacement of each wall at its maximum lateral strength. The most contributing component in the lateral displacements is the flexural component for both *RC* and *RM* walls, where the flexural components of *Phase I RC* walls, *Phase II RC* walls, and *RM* walls range between *76%-90%*, *72%-73%*, and *73%-82%*, respectively, as shown in Figure 5.6. The figure also shows that the sliding components for all walls range from *0.1% to 3.6%*, which is considered minor when compared to flexure and shear components.

The diagonal shear components for the rectangular walls are *10%*, *27%*, and *18%* for *RC1*, *RC4*, and *RM1*, respectively, while the diagonal shear components for the flanged walls are *22%*, *25%*, and *19%* for *RC2*, *RC5*, and *RM2*, respectively. The diagonal shear components for the boundary element walls are *13%*, *27%*, and *18%* for *RC3*, *RC6*, and *RM3*, respectively. The results show that due to the higher vertical reinforcement ratios of *Phase II RC* walls, the shear components of such walls are higher than those of *Phase I RC* and *RM* walls with lower vertical reinforcement ratios, which are aligned with the crack patterns of the walls that were discussed earlier. *RM* walls with rectangular and boundary element configurations showed also higher shear contributions when compared to their counterparts in *Phase I* walls. For walls with flanges, the combined shear and sliding contributions of *RM2* are equivalent to *RC2*. This can be attributed to the weak horizontal and vertical mortar joints in *RM* walls, which forced the diagonal shear cracks and sliding to follow the mortar joints and increased in size at higher displacement levels, resulting in higher displacement contributions when compared to *Phase I RC* walls.

5.4.5 Displacement Ductility

Displacement ductility was evaluated to better quantify the displacement ductility capabilities of well-detailed *RM* walls when compared to *RC* walls. Elastic-perfectly-plastic bilinear idealization was performed by several researchers (Park and Paulay 1991; Paulay and Priestley, 1992; Tomazevic 1999; Priestley et al. 2007; Shedid et al. 2008). Table 5.4 shows the idealized displacement ductility values for both *RM* and *RC* walls following the methodology by Priestley et al. (2007). The displacement ductility, $\mu_{\Delta 0.8u}^{id}$, is the ratio between the ultimate displacement $\Delta_{0.8u}$ and the idealized yield displacement, Δ_y^{id}. Where the idealized yield displacement, Δ_y^{id}, is the intersecting point between two lines. The first line starts at point (0,0) with a slope that is equal to the initial stiffness of the wall. The initial stiffness, K_i, can be calculated, as presented in Eq. (5.1)

$$K_i = \frac{Q_y}{\Delta_y} \tag{5.1}$$

where Q_y is the yield load and Δ_y is the yield displacement.

The second line is a horizontal line taken at the ultimate displacement level, $\Delta_{0.8u}$, at *20%* strength degradation of the wall. The intersecting point between these two lines results in the idealized yield displacement, Δ_y^{id} and the displacement ductility is calculated, as presented in Eq. (5.2)

$$\mu_{\Delta 0.8u}^{id} = \frac{\Delta_{0.8u}}{\Delta_y^{id}} \tag{5.2}$$

Table 5.4 shows that the displacement ductility value of *RM1* is higher than those of *RC1* and *RC4* by *10%* and *25%,* respectively. The displacement ductility value of *RM2* exceeds those of *RC2* and *RC5* by *54%* and *7%,* respectively, while the displacement ductility value

of *RM2* is higher than those of *RC3* and *RC6* by *81%* and *81%,* respectively. The results show that the mortar joints played a vital role in enhancing the ductility of *RM* walls. Specifically, the weak mortar joints distributed the flexural and shear cracks on multiple courses and the tensile bars reached higher plastic strains at several locations. Conversely, in *RC* shear walls, most of the plastic strains were concentrated at the wall-foundation zones. Therefore, *RM* walls reached higher displacement ductility levels with minimal strength degradation when compared to their *RC* counterparts. It is worth mentioning that *RM3* achieved a high displacement ductility value when compared to all other *RC* and *RM* walls because the wall benefited from the weak mortar joints and the confinement of the four bars at the wall ends, as discussed earlier.

5.4.6 Normalized Periods

The effective period of a structure is a key seismic design parameter because when the period decreases, the seismic demands on the structure decrease. The effective period can be computed at any displacement level from a set of design displacement spectra for a given level of ductility demand (Priestley 2000). Figure 5.7 shows the normalized period, T_{norm}, along the lateral displacements of the wall and multiples of the yield displacement of the wall, Δ_y. The normalized period, T_{norm}, was taken as the ratio between the periods at different displacement levels and the initial period, as presented in Eq. (5.3)

$$T_{norm} = \frac{T_e}{T_i} \qquad (5.3)$$

where T_e is the period of the structure at a certain displacement level and T_i is the initial period of the structure.

If a single degree of freedom (SDOF) oscillator was assumed, the T_e period can be computed, as presented in Eq. (5.4)

$$T_e = 2\pi \sqrt{\frac{m}{K_e}} \quad (5.4)$$

where m is the mass and K_e is the secant stiffness at a certain displacement level.

At higher displacement levels, the effective mass of the equivalent SDOF system is not affected. Therefore, the normalized period, T_{norm}, could be related directly to the square root of the ratio between the initial stiffness, K_i, and the secant stiffness, K_e, at a certain displacement level

$$T_{norm} = \sqrt{\frac{K_i}{K_e}} \quad (5.5)$$

Figure 5.7 shows that the normalized period values of the rectangular walls are similar up to *0.5%* drift. At higher drifts, the normalized period values of *RC1* are higher than those of *RC4* and *RM1*. For example, at the ultimate displacement levels (i.e., *20%* strength degradation), the normalized period values of *RM1*, *RC1*, and *RC4* are *3.13*, *3.19*, and *2.73*, respectively. Regarding the flanged and boundary elements walls, *Phase I RC* walls (*RC2* and *RC3*) showed higher normalized period values when compared to their *RC* and *RM* counterparts. For example, at the ultimate displacement levels, the normalized period value of *RC2* is higher than those of *RC5* and *RM2* by *29%* and *14%*, respectively, while the normalized period value of *RC3* exceeds those of *RC6* and *RM3* by *15%* and *10%*, respectively. Therefore, it can be concluded that, for *RC* (*Phase I*) and *RM* walls with similar lateral strengths, reduced seismic demands are expected for *RC* walls when compared to *RM* walls.

5.4.7 Equivalent Viscous Damping

The hysteric damping behavior of *RC* and *RM* walls is defined herein as the equivalent viscous damping ratio, ξ_{eq}. An equal area approach was used to calculate the equivalent damping ratio, ξ_{eq}, which represents the sum of energy loss for each cycle (Hose and Seible 1999; Chopra 2000). The equivalent viscous damping ratio, ξ_{eq}, was computed as shown in Eq. (5.6)

$$\xi_{eq} = \sum_{i=1}^{\Delta_i} \frac{1}{4\pi} \times \left(\frac{E_d}{E_s}\right) \qquad (5.6)$$

where E_d is the dissipated energy and E_s is the strain energy.

Figure 5.8 shows the equivalent viscous damping ratios versus multiples of yield displacement, Δ / Δ_y, for all the walls. At yield, the equivalent viscous damping ratios of *RM* walls are around 8%, and the ratios of *RC* walls are between *10%* and *18%*. At $2\Delta_y$, the equivalent viscous damping ratios of *RM* and *RC* walls range between *8%-13%* and *11%-21%*, respectively. At ultimate displacement levels, the equivalent viscous damping ratios of *RM* and *RC* walls are *21%-35%* and *30%-53%*, respectively.

For *RM* walls, the elastic to yield equivalent viscous damping ratios typically range between *7%-10%* as per Drysdale and Hamid (2008) which agrees with the results of *RM1*, *RM2*, and *RM3*, as shown in Figure 5.8. However, the equivalent viscous damping ratios of *Phases I* and *II RC* walls are higher than *5%-7%* as per recommended by Paulay and Priestley (1992) and NBCC (2020) for *RC* walls in the elastic range up to yield. Both *RC* and *RM* walls achieved also significantly high damping ratios beyond their yield levels; however, Figure 5.8 shows that the equivalent viscous damping ratios of *RC* walls are higher than those of *RM* walls.

5.5 CONSTRUCTION ECONOMIC ASSESSMENT

A comparative economical evaluation was performed between the *RC* and *RM* shear walls, where the total rebar weights and total construction costs of the nine walls were calculated and compared.

5.5.1 Total Rebar Weight

The total rebar weight used in the construction of each *RC* and *RM* wall was calculated. To allow for direct comparisons between the walls, the total rebar weight of each wall was then normalized by its average experimental lateral strength, Q_u, (Abouyoussef and Ezzeldin 2023; Barbachyn et al. 2017), as presented in Eq. (5.7)

$$\Omega = \frac{W_r}{Q_u} \tag{5.7}$$

where *Wr* is the total rebar weight (kg) and Ω is the rebar weight factor (kg/kN).

Figure 5.9(a) shows that the rebar weight factor, Ω, values for the *RC* walls in *Phases I* and *II* are higher than their RM counterparts, where such factors range between *0.48-0.68 (kg/kN)*, *0.65-0.67 (kg/kN)*, and *0.38-0.45(kg/kN)* for *Phase I RC* walls, *Phase II RC* walls, and *RM* walls, respectively. These results are mainly attributed to the strict requirements for ductile shear walls in CSA A23.3-19 (CSA 2019a), where the spacing requirements between the horizontal ties are tighter than those in CSA S304-19 (CSA 2019b). In addition, CSA A23.3-19 (CSA 2019a) specifies two mats of vertical and horizontal rebars, unlike the single mat that is permitted in *RM* walls as per CSA S304-19 (CSA 2019b). Therefore, it can be concluded that, based on the rebar weight factor, Ω, *RM*

walls require significantly less rebar weight (kg) per unit lateral force (kN) when compared to their *RC* counterparts.

5.5.2 Overall Construction Cost

Based on RS-Means (Gordian Group 2016), the costs associated with the construction of each wall system are presented in Table 5.5. Specifically, the costs of the ready-mix concrete with different compressive strengths are presented in Table 5.5(a), while the costs of the concrete forms (material and labor) and concrete placing are presented in Table 5.5(b). For *RM* walls, the costs associated with the concrete block, grout, and labor are summarized in Table 5.5(c). The rebar costs and labor costs for bending rebars are also noted in Table 5.5(d). The cost of each wall was computed and normalized by its respective average experimental lateral strength, Q_u, (Abouyoussef and Ezzeldin 2023; Barbachyn et al. 2017), as presented in Eq. (5.8)

$$\Gamma = \frac{C_w}{Q_u} \tag{5.8}$$

where C_w is the total construction cost of each wall ($) and Γ is the construction cost factor ($/kN).

Figure 5.9(b) shows the construction cost factor, Γ, values for *Phase I RC* walls range between *10.07-14.74($/kN),* where the highest factors are associated with flanged (*RC2*) and boundary element (*RC3*) walls. For *Phase II RC* walls, the construction cost factor, Γ, values are *7.68-9.48($/kN)*, whereas the values for *RM* walls range between *6.37-8.38($/kN)*. Interestingly, the gaps between *Phase II RC* walls and *RM* walls are closer than

those between *Phase I RC* walls and *RM* walls. Overall, as can be seen in Figure 5.9(b), the total construction costs of all *RM* walls are lower than those of *RC* walls in both phases.

5.6 CONCLUSIONS

A comparative seismic analysis was performed in the current study between six reinforced concrete (*RC*) shear walls and three reinforced masonry (*RM*) shear walls. The three *RC* walls tested in *Phase I* with low reinforcement ratios had similar lateral strengths as their three *RM* counterparts, while the three *Phase II RC* walls with high reinforcement ratios had similar ultimate curvature values when compared to their three corresponding *RM* walls. The analysis results presented for the nine walls in terms of their crack patterns, load-displacement envelopes, curvature profiles, wall displacements, displacement ductility, normalized periods, and equivalent viscous damping ratios. An economical assessment was also performed to compare the walls in terms of their total rebar weights and total construction costs. The comparatives analysis concluded the following:

- Cracks of *RM* walls mostly followed the weak horizontal and vertical mortar joints. The diagonal shear cracks of *RM* walls were higher in number and width when compared to their *Phase I RC* counterparts. On the other hand, *RM* walls experienced fewer diagonal shear cracks when compared to *Phase II RC* walls, due to the higher vertical reinforcement ratios used in *Phase II RC* walls. *RM* walls had a lower number of flexural cracks when compared to their *RC* counterparts; however, most of the flexural cracks of *RC* walls were hairline cracks.

- *RM* shear walls achieved higher ultimate displacements when compared to *Phase I RC* walls by *1.3*, *1.8*, and *2.5* times for the rectangular, flanged, and boundary element walls, respectively. *RM* shear walls also achieved higher ultimate displacements than *Phase II RC* walls by *1.3* and *1.5* times for the flanged and boundary element walls, respectively. In addition, *RM* walls showed higher ultimate curvature values above the wall-foundation interface when compared to their *RC* counterparts. These results are attributed to the weak mortar joints in *RM* walls that distributed the plastic strains over several courses and enlarged the diagonal shear cracks at the joint locations, in which the plastic strains were concentrated in *RC* walls at the wall-foundation interfaces and diagonal shear cracks were mostly hairline cracks.
- *RM* walls showed higher displacement ductility values at the ultimate level for rectangular, flanged, and boundary element walls by *10%*, *54%*, and *82%*, respectively, than *Phase I RC* walls. When compared to *Phase II RC* walls, *RM* walls achieved higher displacement ductility values by *25%*, *7%*, and *82%* for rectangular, flanged, and boundary element walls, respectively.
- The normalized period values of *Phase I RC* walls increased with higher rates of *2%-14%* when compared to *RM* walls, while *RM* walls showed higher normalized periods when compared to *Phase II RC* walls by *6-14%*.
- The equivalent viscous damping ratios of *RM* shear walls at the yield stage were within the recommended ranges; however, *RC* shear walls showed higher equivalent viscous damping ratios than *RM* shear walls beyond the yield stage.

- *RM* shear walls showed lower rebar weight factors when compared to their *RC* counterparts. The construction cost factors of *RM* shear walls were lower than those of *RC* shear walls in both phases. These results are due to the more stringent design requirements (e.g., the reinforcement spacing and the number of reinforcement mats) for *RC* ductile walls in CSA A23.3-19 (CSA 2019a) than those for *RM* ductile shear walls in S304.1-19 (CSA 2019b).

5.7 REFERENCES

Abouyoussef, M., & Ezzeldin, M. (2023) Fragility and Economic Evaluations of High-Strength Reinforced Concrete Shear Walls in Nuclear Power Plants. *Journal of Structural Engineering*, https://doi.org/10.1061/JSENDH/STENG-11397.

Adebar, P., Ibrahim, A. M., & Bryson, M. (2007). Test of high-rise core wall: effective stiffness for seismic analysis. *ACI Structural Journal*, *104*(5), 549.

Akl, A., & Ezzeldin, M. (2023). Seismic collapse risk assessment of low-aspect-ratio reinforced concrete shear walls using the FEMA P695 methodology. *Journal of Structural Engineering*, http://10.1061/(ASCE)ST.1943-541X.0003505.

Ahmadi, F., Hernandez, J., Sherman, J., Kapoi, C., Klingner, R. E., & McLean, D. I. (2014). Seismic performance of cantilever-reinforced concrete masonry shear walls. *Journal of Structural Engineering*, *140*(9), 04014051.

ASCE. (2022). *Minimum Design Loads and Associated Criteria for Buildings and Other Structures*. ASCE 7-22, ASCE, Reston, Va.

Banting, B. R., & El-Dakhakhni, W. W. (2012). Force-and displacement-based seismic

performance parameters for reinforced masonry structural walls with boundary elements. *Journal of Structural Engineering*, *138*(12), 1477-1491.

Barbachyn, S. M., Devine, R. D., Thrall, A. P., & Kurama, Y. C. (2017). Economic evaluation of high-strength materials in stocky reinforced concrete shear walls. *Journal of Construction Engineering and Management*, *143*(10), 04017074.

Canadian Standards Association (CSA). (2019a). *Design of concrete structures*. CSA A23.3-19, CSA, Mississauga, Canada.

Canadian Standards Association CSA (2019b). *"Design of masonry structures." CSA S304-19*, Mississauga, Ontario, Canada.

Canadian Standards Association (CSA). (2021). *Carbon steel bars for concrete reinforcement.* CSA G30.18-21, CSA, Mississauga, Canada.

Canterbury Earthquake Royal Commission report. (2011). *Seismic performance Christchurch building under the Canterbury Earthquake.* Retrieved Nov. 19th, 2019, http://canterbury.royalcommission.govt.nz/Final-Report-Volume-One-Contents

Chopra, A. (2000). *Dynamics of structures; theory and application to earthquake engineering.* 2nd ed. Englewood Cliffs, NJ, USA; Prentice Hall Inc.

Christidis, K. I., & Trezos, K. G. (2017). Experimental investigation of existing non-conforming RC shear walls. *Engineering Structures*, *140*, 26-38.

Drysdale, R. G., & Hamid, A. A. (2008). Masonry structures: Behaviour and design (Canadian edition). *Canada Masonry Design Centre, Mississauga, Ontario*, *769*.

Eikanas, I. K. (2003). Behavior of concrete masonry shear walls with varying aspect ratio and flexural reinforcement MS Thesis, Department of Civil and Environmental Engineering. *Pullman, WA: Washington State University*.

El-Azizy, O. A., Shedid, M. T., El-Dakhakhni, W. W., & Drysdale, R. G. (2015). Experimental evaluation of the seismic performance of reinforced concrete structural walls with different end configurations. *Engineering Structures*, *101*, 246-263.

El Ezz, A. A., Seif Eldin, H. M., & Galal, K. (2015). Influence of confinement reinforcement on the compression stress–strain of grouted reinforced concrete block masonry boundary elements". *Structures*, 2, 32-43, Elsevier.

Ezzeldin, M., El-Dakhakhni, W., & Wiebe, L. (2017). Experimental assessment of the system-level seismic performance of an asymmetrical reinforced concrete block–wall building with boundary elements. Journal of Structural Engineering, 143(8), 04017063.

Ghorbanirenani, I., Tremblay, R., Léger, P., & Leclerc, M. (2012). Shake table testing of slender RC shear walls subjected to eastern North America seismic ground motions. *Journal of Structural Engineering*, *138*(12), 1515-1529.

Gondia, A., Ezzeldin, M., & El-Dakhakhni, W. (2020). Mechanics-guided genetic programming expression for shear-strength prediction of squat reinforced concrete walls with boundary elements. *Journal of Structural Engineering*, *146*(11), 04020223.

Gordian Group. (2016). RSMeans building construction cost data, 75th Annual Ed., Greenville, SC, 825.

Haach, V. G., Vasconcelos, G., & Lourenço, P. B. (2010). Experimental analysis of reinforced concrete block masonry walls subjected to in-plane cyclic loading.

Hose, Y. D., & Seible, F. (1999). *Performance evaluation database for concrete bridge components and systems under simulated seismic loads*. Pacific Earthquake Engineering Research Center, College of Engineering, University of California.

Jünemann, R., Hube, M., De La Llera, J. C., & Kausel, E. (2012, September). Characteristics of reinforced concrete shear wall buildings damaged during 2010 Chile earthquake. In *Proceedings of the 15th World Conference of Earthquake Engineering*.

Luu, H., Léger, P., & Tremblay, R. (2014). Seismic demand of moderately ductile reinforced concrete shear walls subjected to high-frequency ground motions. *Canadian journal of civil engineering*, *41*(2), 125-135.

Massone, L. M., & Wallace, J. W. (2004). Load-deformation responses of slender reinforced concrete walls. *Structural Journal*, *101*(1), 103-113.

NBCC (2020): National Research Council of Canada (2020). *National Building Code of Canada.*

Park, R., & Paulay, T. (1991). *Reinforced concrete structures*. John Wiley & Sons.

Paulay, T., & Priestley, M. N. (1992). Seismic design of reinforced concrete and masonry buildings (Vol. 768). New York: Wiley.

Priestley M. (2000). *"Performance based seismic design."* Proc. 12th World Conference Earthquale Engineering, New Zealand Society for Earthquake Engineering, New Zealand.

Priestley, M. J. N., Calvi, G.M., & Kowalsky, M. J., (2007). *Displacement-based seismic design of structures.* Pavia, Italy: IUSS Press,

Rong, X. L., Zheng, S. S., Zhang, Y. X., Zhang, X. Y., & Dong, L. G. (2020). Experimental study on the seismic behavior of RC shear walls after freeze-thaw damage. *Engineering Structures*, *206*, 110101.

Shedid, M. T., Drysdale, R. G., & El-Dakhakhni, W. W. (2008). Behavior of fully grouted reinforced concrete masonry shear walls failing in flexure: Experimental results. *Journal of structural engineering*, *134*(11), 1754-1767.

Shedid, M. T., El-Dakhakhni, W. W., & Drysdale, R. G. (2010). Alternative strategies to enhance the seismic performance of reinforced concrete-block shear wall systems. *Journal of structural engineering*, *136*(6), 676-689.

Siyam, M. A., El-Dakhakhni, W. W., Shedid, M. T., & Drysdale, R. G. (2016). Seismic response evaluation of ductile reinforced concrete block structural walls. I: Experimental results and force-based design parameters. *Journal of Performance of Constructed Facilities*, *30*(4), 04015066.

Thomsen IV, J. H., & Wallace, J. W. (2004). Displacement-based design of slender reinforced concrete structural walls—experimental verification. *Journal of structural engineering*, *130*(4), 618-630.

Tomazevic, M. (1999). *Earthquake-resistant design of masonry buildings* (Vol. 1). World Scientific.

Zhang, Y., & Wang, Z. (2000). Seismic behavior of reinforced concrete shear walls subjected to high axial loading. *Structural Journal*, 97(5), 739-750.

5.8 TABLES

Table 5.1: Wall configurations, dimensions, vertical and horizontal reinforcement ratios, and axial stress levels

Walls	Configuration		Wall Dimensions	Vertical Reinforcements		Horizontal Reinforcements		Axial Stress (MPa)
				Number of bars and bar sizes	ρ_v (%)	D4 at spacing (mm)	ρ_h (%)	
RC1	Rectangular	***Phase I El-Azizy et al. (2015)***	1,802mm × 3,990mm length×height	42 D7	1.17	2 at 90	0.64	1.09
RC2	Flanged			16 D7 & 22 D4	0.66	2 at 110	0.53	0.89
RC3	Boundary Elements			20 D7 & 18 D4	0.69	2 at 110	0.53	0.89
RC4	Rectangular	***Phase II El-Azizy et al. (2015)***		64 D11	2.80	2 at 45	1.28	1.09
RC5	Flanged			16 D11 & 44 D7	1.58	2 at 55	1.05	0.89
RC6	Boundary Elements			20 D11 & 40 D7	1.63	2 at 55	1.05	0.89
RM1	Rectangular	***Shedid et al. (2010)***		19 M10	1.17	1 at 95	0.30	1.09
RM2	Flanged			11 M10	0.55	1 at 95	0.30	0.89
RM3	Boundary Elements			11 M10	0.55	1 at 95	0.30	0.89

Note: In this chapter, to avoid confusion between RC & RM walls, RC walls W1-W6 were named RC1-RC6, respectively.

Table 5.2: Theoretical and experimental strengths of the walls

Walls	Configuration		Yield Strength, Q_y			Maximum Strength, Q_u		
			Theoretical (kN)	Experimental (kN)		Theoretical (kN)	Experimental (kN)	
				Push (+ve)	Pull (-ve)		Push (+ve)	Pull (-ve)
RC1	Rectangular	***Phase I El-Azizy et al. (2015)***	136	152	123	193	230	172
RC2	Flanged		136	175	158	177	187	183
RC3	Boundary Elements		135	160	160	178	176	177
RC4	Rectangular	***Phase II El-Azizy et al. (2015)***	233	222	195	351	336	355
RC5	Flanged		218	220	270	330	322	313
RC6	Boundary Elements		213	227	209	332	334	313
RM1	Rectangular	***Shedid et al. (2010)***	95	101	110	170	177	180
RM2	Flanged		122	121	123	163	151	154
RM3	Boundary Elements		123	110	106	165	152	147

Table 5.3: Yield and ultimate curvatures of the walls

Walls	Configuration	Ultimate Curvature, $\phi_u \times 10^{-3}$ (rad/m)		
		At *75mm* from the interface	At *490mm* from the interface	At *775mm* from the interface
RC1	Rectangular	10.03	2.67	1.84
RC2	Flanged	7.27	3.53	1.50
RC3	Boundary Elements	7.07	3.71	1.54
RC4	Rectangular	6.71	2.76	2.94
RC5	Flanged	14.84	5.89	3.43
RC6	Boundary Elements	11.92	5.34	2.07
RM1	Rectangular	7.77	4.31	2.71
RM2	Flanged	11.83	5.18	4.70
RM3	Boundary Elements	12.49	11.43	5.32

Table 5.4: Displacements, normalized periods, and displacement ductility values of the walls

				Measured displacements and Normalized Period						Displacement ductility at 20% strength degradation
				At first yield		At maximum load		At 20% strength degradation		
Wall	Configuration		Direction	Δ_y (mm)	T_y (T_{norm})	Δ_u (mm)	T_u (T_{norm})	$\Delta_{0.8u}$ (mm)	$T_{0.8u}$ (T_{norm})	$\mu_{\Delta 0.8u}^{id}$
RC1	Rectangular	***Phase I***	+(ve)	8.3	1.52	22.7	2.27	36.6	3.19	2.9
			-(ve)			17.1		34.5		3.0
RC2	Flanged		+(ve)	8.7	1.99	20.3	2.67	27.8	5.29	3.0
			-(ve)			19.1		37.8		3.8
RC3	Boundary Elements		+(ve)	8.3	1.94	16.8	2.64	39.3	4.67	4.3
			-(ve)			17.1		35.2		3.8
RC4	Rectangular	***Phase II***	+(ve)	10.9	1.66	28.6	2.18	45.9	2.73	2.8
			-(ve)			34.4		48.4		2.4
RC5	Flanged		+(ve)	9.1	1.63	-	-	-	-	-
			-(ve)			33.8	2.93	52	4.07	4.9
RC6	Boundary Elements		+(ve)	10.5	1.86	31.5	2.65	63	4.03	4.1
			-(ve)			31.5		62.7		4.0
RM1	Rectangular	***RM Walls***	+(ve)	8.5	1.54	25.1	2.06	45.0	3.13	3.0
			-(ve)			25.3		48.0		3.5
RM2	Flanged		+(ve)	10.5	1.84	31.5	2.86	70.0	4.63	5.3
			-(ve)			31.5		68.0		5.2
RM3	Boundary Elements		+(ve)	9.2	1.80	36.0	3.02	93.0	4.27	7.3
			-(ve)			36.1		95.0		7.4

Table 5.5: (a) Ready, mix concrete costs; (b) Concrete forms/ labor costs; (c) Masonry Block walls costs (Including labor and grout); (d) Rebar costs (Including labor)

Ready mix normal-weight concrete	
Compressive strength f'_c (MPa)	Cost ($)/ m^3
28	224.81
36	252.59
41	276.46

(a)

Labor and miscellaneous additional items for *RC* walls	
Item	Costs ($)
Concrete forms (materials only) / m^2	12.70
Concrete forms labor costs (includes stripping and cleaning) / m^2	110.86
Concrete placing and vibrating / m^3	38.08

(b)

Masonry concrete block walls	
Block Dimension (mm) 200×200×400	Costs ($)/ m^2
[1]Hollow block f'_m= 27MPa	75.29
Grout	37.65
Labor (laying blocks, grouting, placing mortar, tooling joints)	73.43

(c)

Rebar used for both wall systems	
Reinforcing Steel A615M, Grade 60	Costs ($)/ metric ton
Reinforcement material cost/metric ton	1720.98
Labor costs (includes laying rebar and bending rebar horizontal, vertical and ties)	793.52

(d)

Note: Prices are based on available data in RS-Means (Gordian Group 2016).

5.9 FIGURES

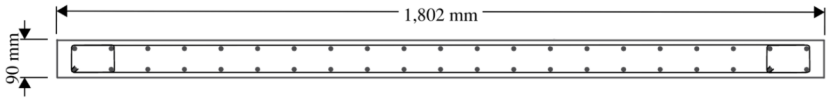

(a) *RC1*

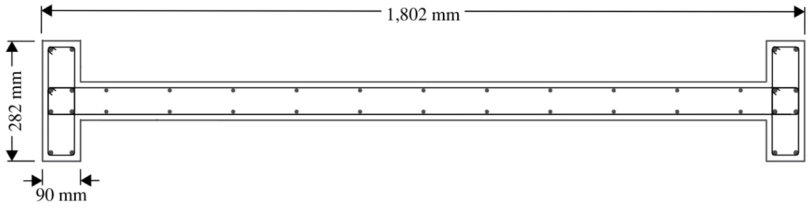

(b) *RC2*

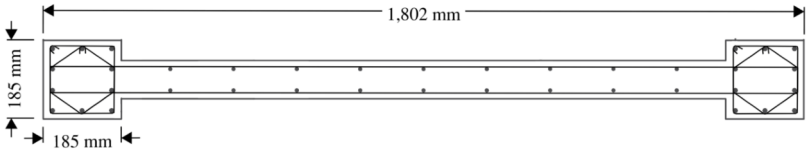

(c) *RC3*

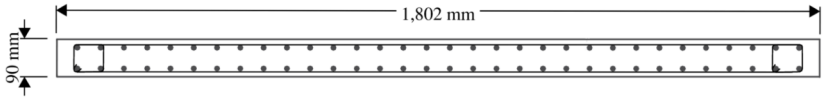

(d) *RC4*

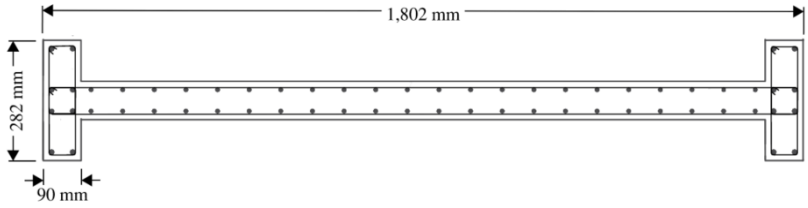

(e) *RC5*

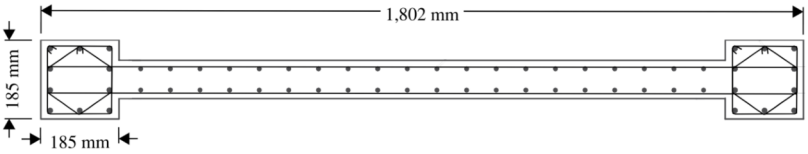

(f) *RC6*

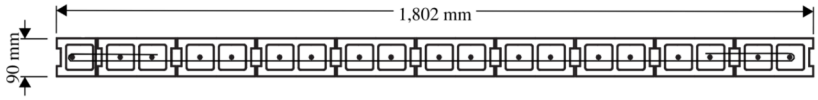

(g) *RM1*

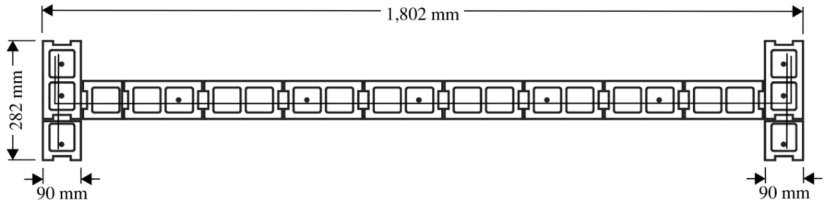

(h) *RM2*

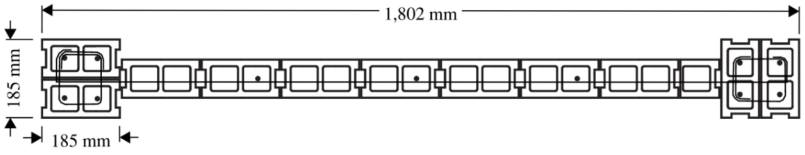

(i) *RM3*

Figure 5.1: Cross-section of *RC* and *RM* shear walls

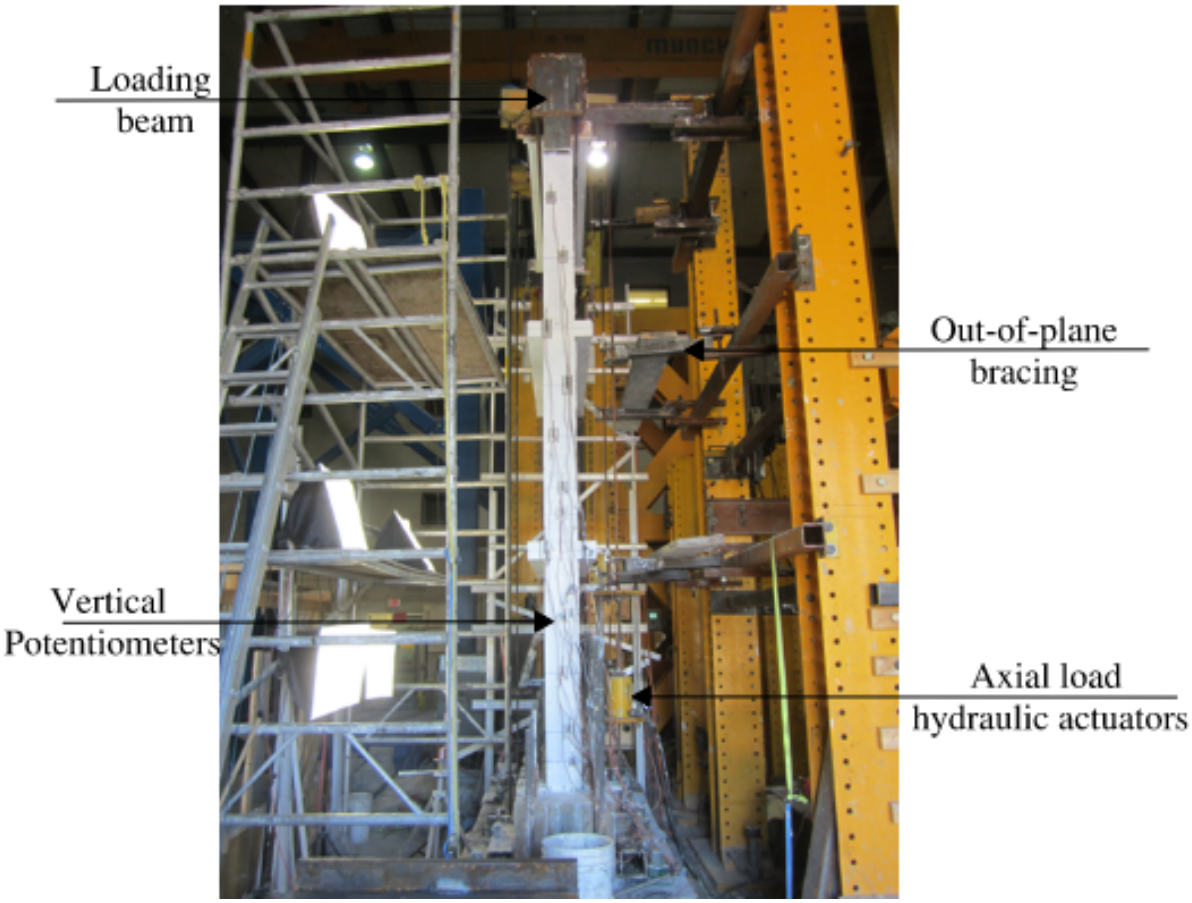

Figure 5.2: Test setup

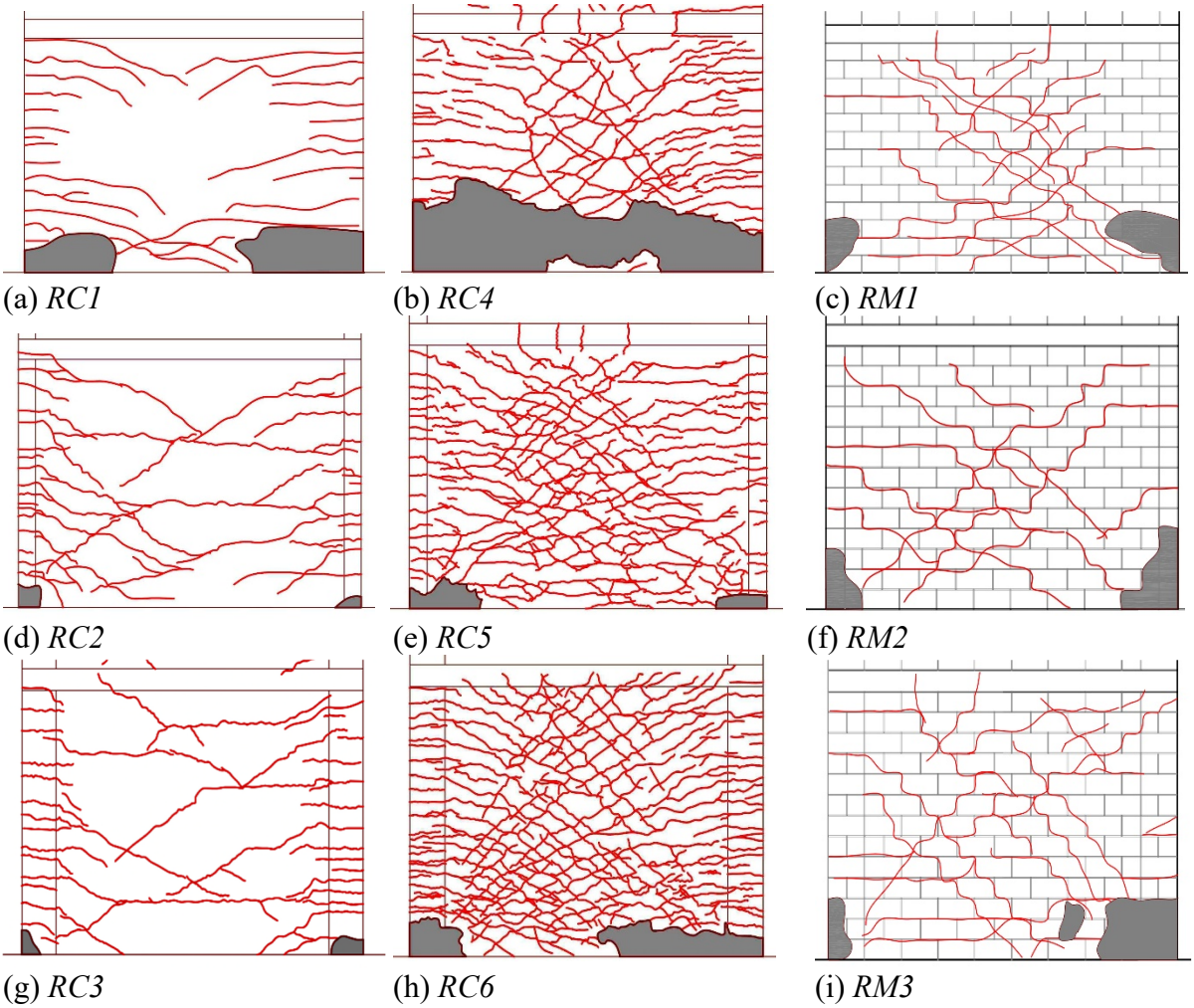

Figure 5.3: Crack patterns of the first story

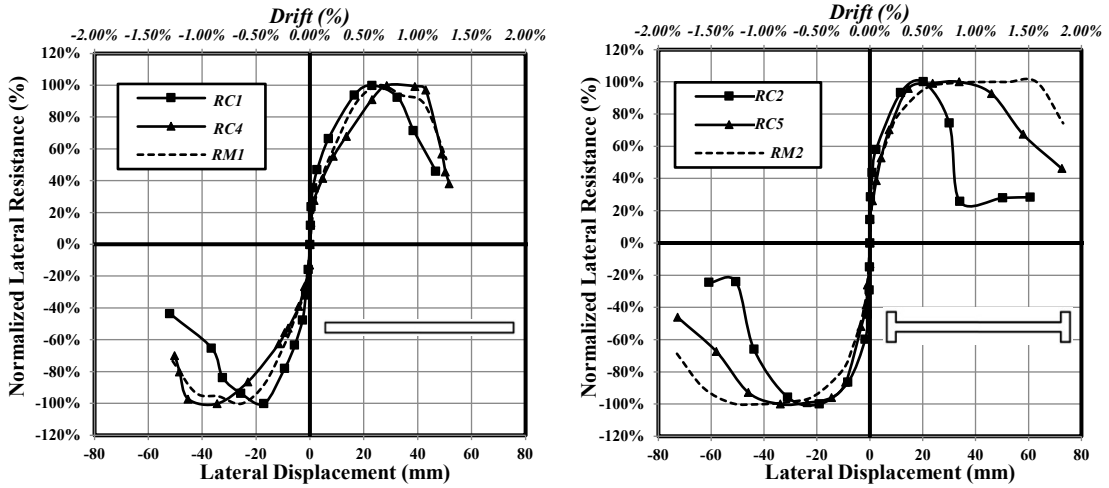

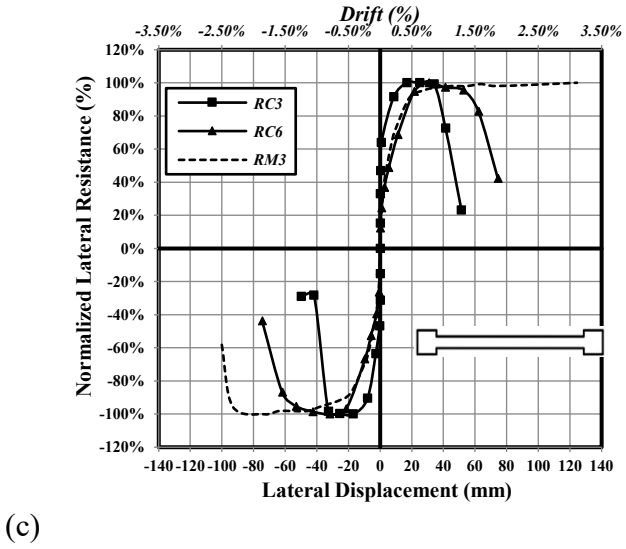

Figure 5.4: Normalized load-displacement envelopes of *RC* and *RM* walls; (a) Rectangular walls; (b) Flanged walls; and (c) Boundary elements walls

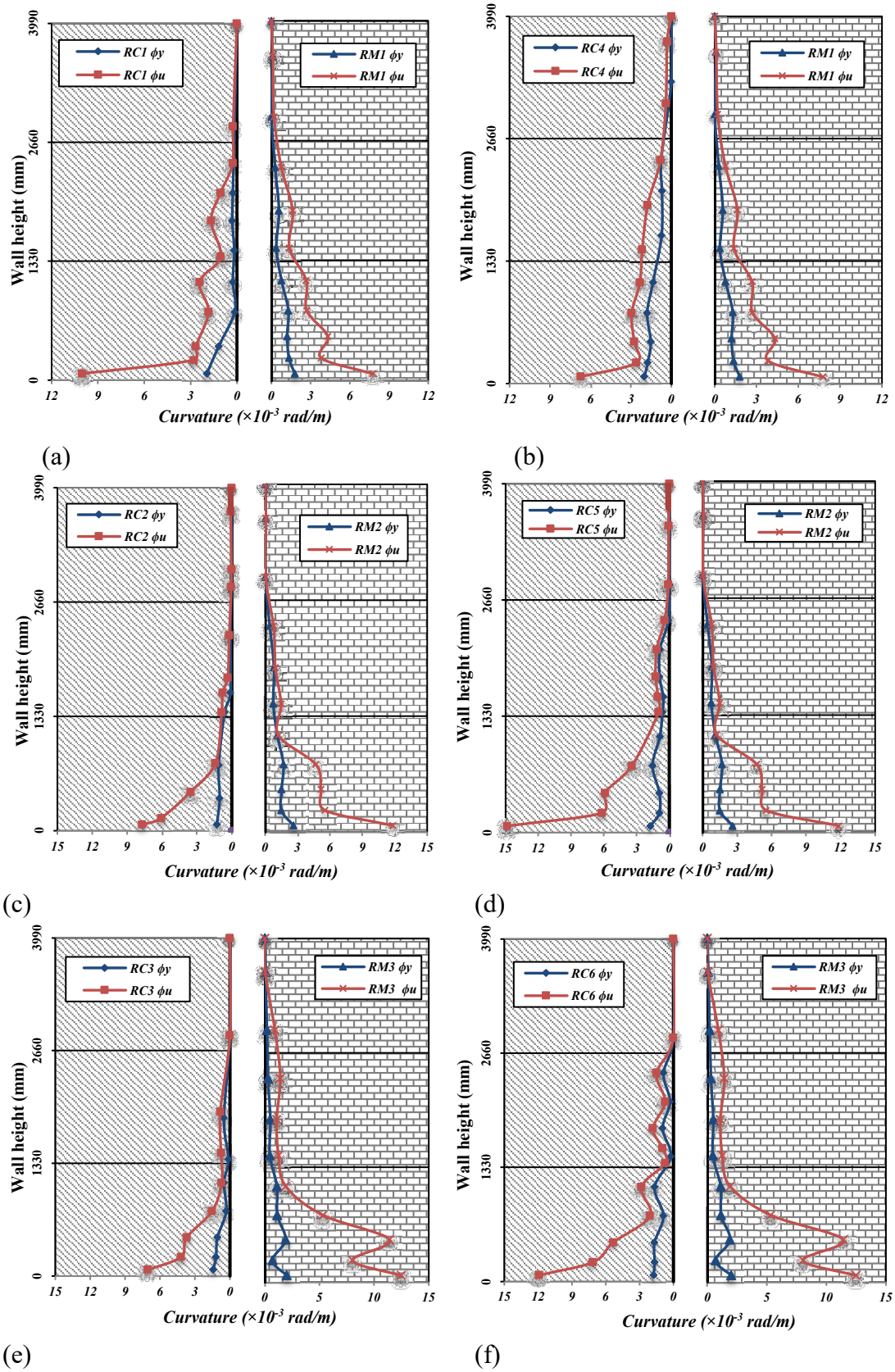

Figure 5.5: Curvature profiles at yield and maximum loads for Rectangular walls; (a) *RC1* vs. *RM1* and (b) *RC4* vs. *RM1*, Flanged walls; (c) *RC2* vs. *RM2* and (d) *RC5* vs. *RM2* and Boundary Element walls; (e) *RC3* vs. *RM3* and (f) *RC6* vs. *RM3*

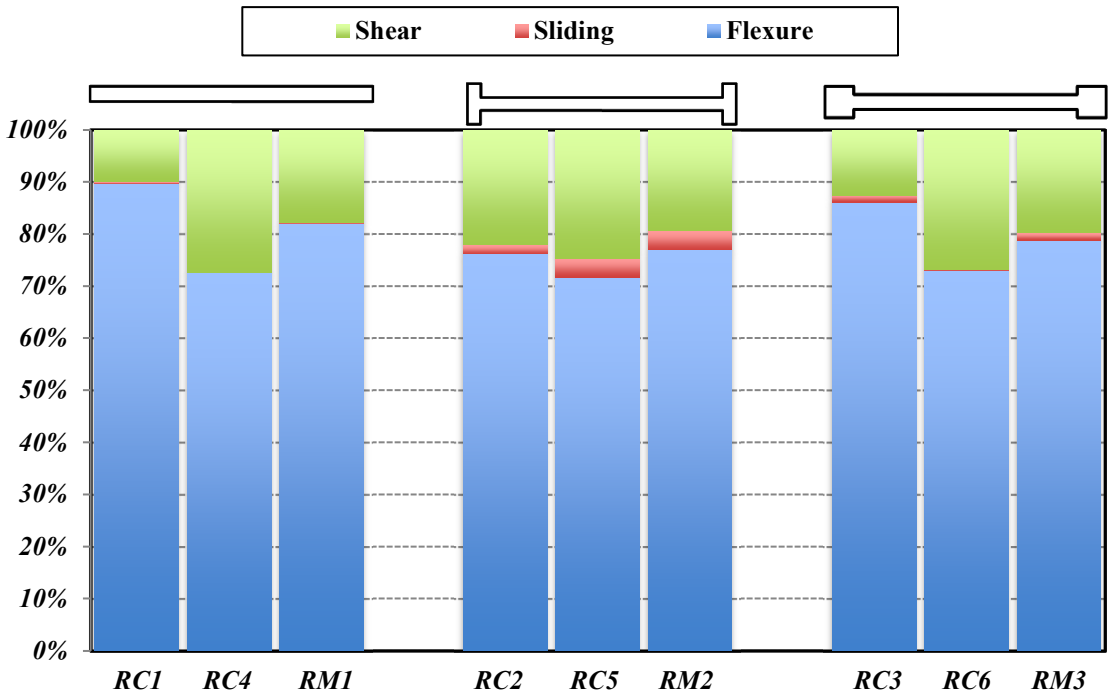

Figure 5.6: Flexure, sliding, and shear contributions to the total wall top displacements at the maximum lateral strength

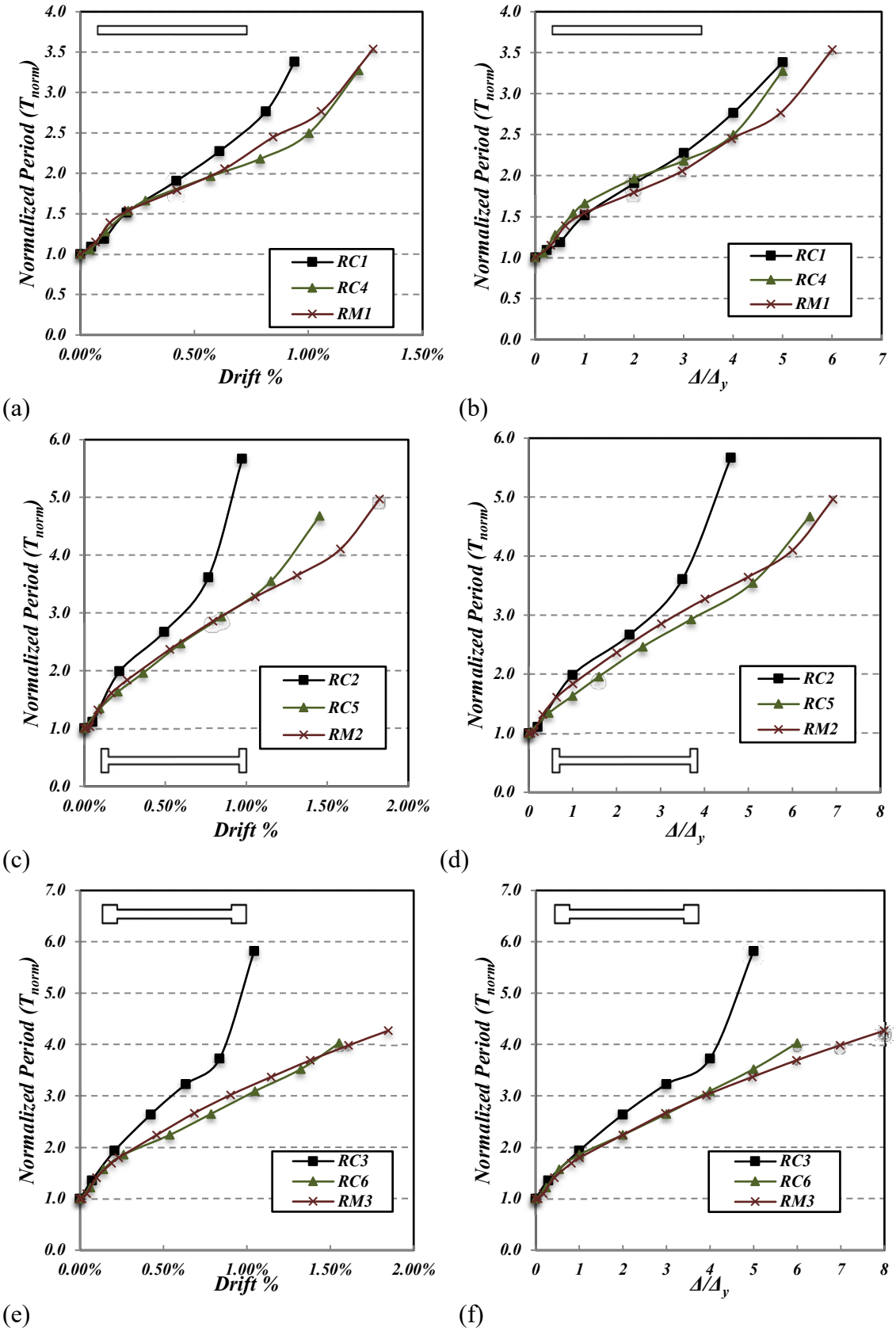

Figure 5.7: Normalized periods versus the drifts and displacement levels; (a &b) Rectangular walls; (c & d) Flanged walls; (e & f) Boundary Elements walls

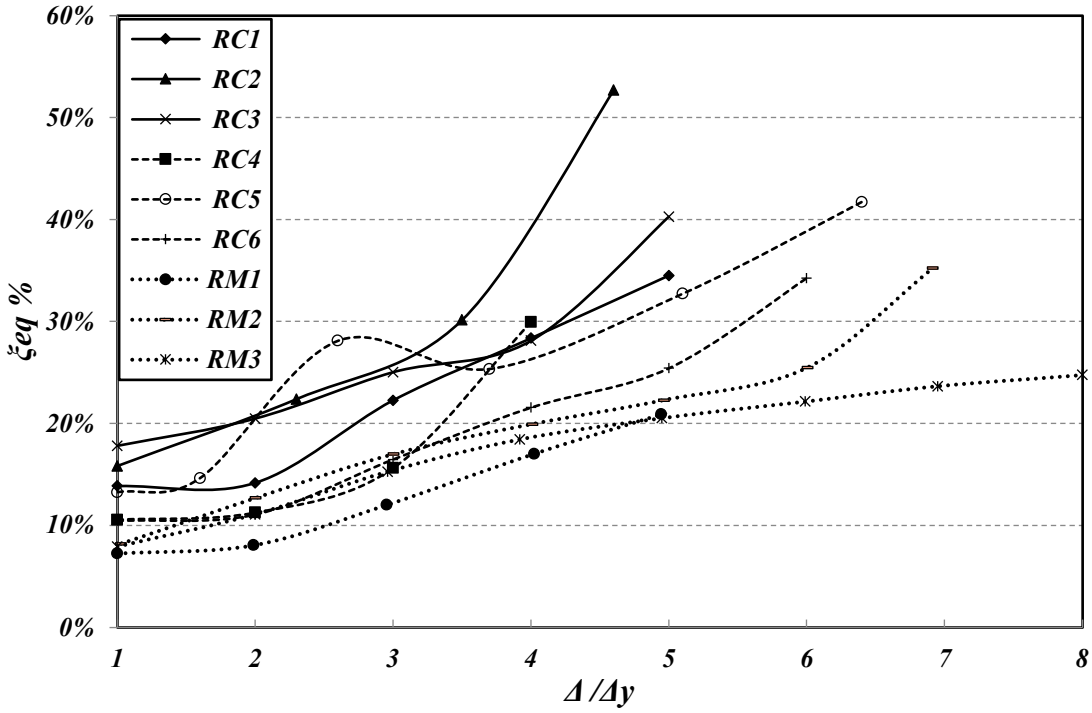

Figure 5.8: Equivalent viscous damping ratios at different displacement levels

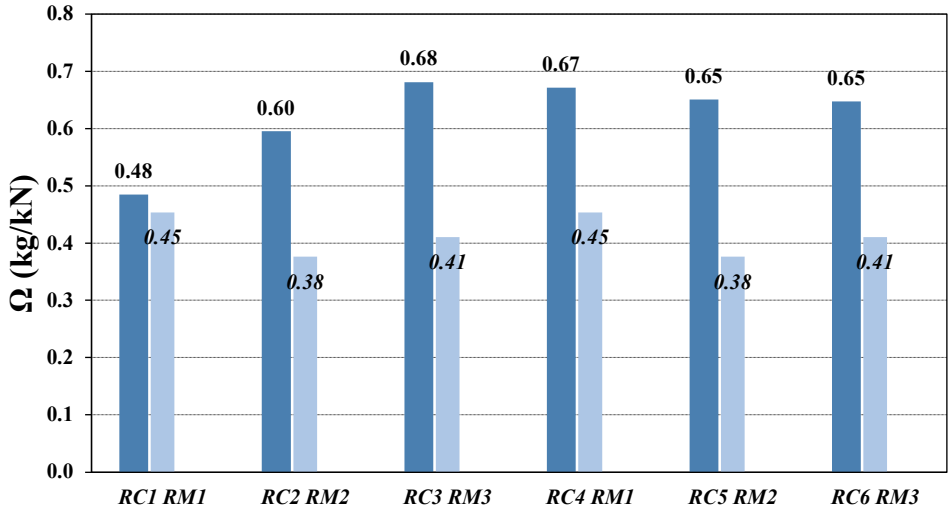

(a)

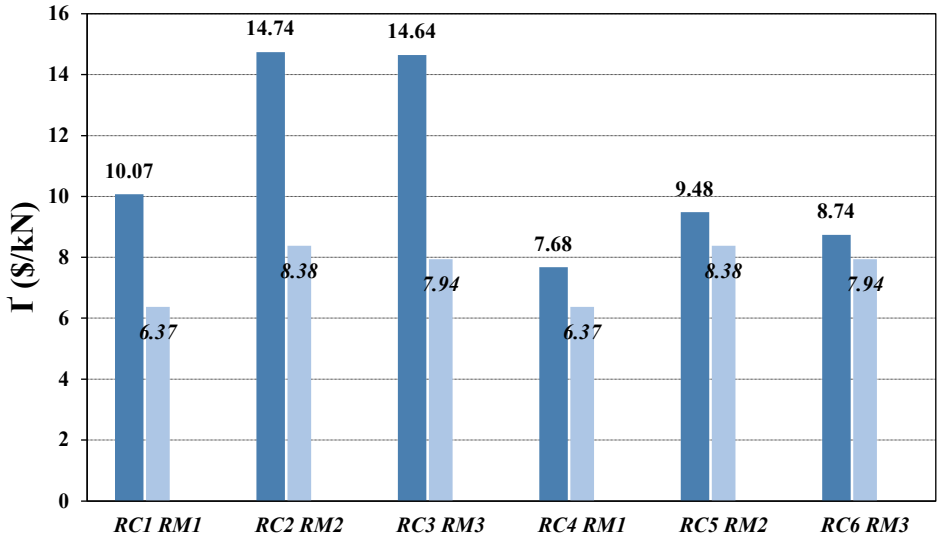

(b)

Figure 5.9: Economic assessment of *RC* and *RM* shear walls
(a) total rebar weight; and (b) overall construction cost

CHAPTER 6
SUMMARY, CONCLUSIONS AND RECOMMENDATIONS

6.1 SUMMARY

This dissertation evaluates the seismic performance of well-detailed *RC* shear walls with different end configurations. In this respect, six half-scale *RC* walls are tested under a quasi-static cyclic fully-reversed loading to represent seismic demands. The experimental program contains two phases, where *Phase II* walls have *2.4* times the vertical reinforcement ratios of their respective *Phase I* counterparts and each phase has rectangular, flanged, and boundary element walls. The experimental and analysis results of the walls are presented in terms of their crack patterns, failure modes, load-displacement envelopes, stiffness degradation trends, end-strains, yield and ultimate curvatures, curvature profiles, extents of plasticity, reinforcement strains, energy dissipation capabilities, and equivalent viscous damping ratios. Using such results, an analytical model is developed and validated to generate a dataset of displacement ductility values for *RC* walls using various design parameters (i.e., cross-sectional properties, aspect ratios, axial loads, concrete compressive strengths, and vertical reinforcement ratios). The dataset is then used to develop and experimentally validate two data-driven expressions (i.e., for rectangular and flanged/boundary element walls) based on an inverse linear regression model. Subsequently, the interpretability of the expressions is analyzed and compared to the known mechanics of *RC* shear walls. Finally, a comparative analysis is performed between the six *RC* walls and three *RM* tested in a previous experimental program. To facilitate this comparison, *Phase I RC* walls are designed to have the same lateral strength

as their respective *RM* shear walls, while *Phase II RC* walls have similar ultimate curvature values as their *RM* counterparts. In addition, an economic assessment is performed to evaluate the total rebar weights and total construction costs of *RC* and *RM* walls.

6.2 CONCLUSIONS

The experimental, analytical, and data-driven results of this dissertation demonstrate the effects of the different end configurations and the vertical reinforcement ratios on the seismic performance of *RC* shear walls. This section presents the overarching conclusions based on the research results presented in the preceding chapters.

The ductility capacities of *RC* walls with relatively high vertical reinforcement ratios exceeded their counterparts with low vertical reinforcement ratios, where these findings agree with those of the Canterbury earthquake royal commission report. *RC* walls with low vertical reinforcement ratios showed low seismic performance due to the concentration of the plastic strains at the primary crack locations, which resulted in limited plastic hinge lengths, rapid strength degradations, and thus low ductility capacities. While by relatively increasing the vertical reinforcement ratio and concentrating the rebar at the outer regions, the walls initiated secondary cracks that distributed the plastic demands on several cracks, resulting in large plastic hinge lengths, high lateral displacement levels with minimum strength degradation, and high ductility capacities.

The end configurations have a major effect on the seismic performance of *RC* shear walls, which agrees with both the recommendations noted in the Canterbury earthquake

royal commission report and the observations of the 2010 Maule earthquake. *Phase II* flanged and boundary element walls showed better seismic performance when compared to their rectangular counterparts, where the larger confined area of the former walls sustained higher compressive stresses, resulting in delayed strength degradation at higher displacement levels. In addition, flanged and boundary element walls showed higher stiffness degradation rates, which would result in lower seismic demands than rectangular walls. Moreover, flanged and boundary element walls showed higher normalized energy dissipation capacities, resulting in an enhanced seismic performance when compared to their rectangular counterparts.

The analytical model results came in good agreement with the experimental results of the walls used in the validation in terms of their curvature profiles, plastic hinge lengths, end strains, load-displacement relationships, and displacement ductility values. The analytical model successfully generated 40 rectangular and 53 flanged/boundary element walls that were used to develop two data-driven expressions to predict the displacement ductility of *RC* walls. The data-driven expressions were in good agreement with a testing dataset of *RC* walls experimentally evaluated in previous research studies. The interpretability analysis demonstrated that the proposed data-driven expressions were in agreement with the known response of mechanics as well as previous research findings. This analysis concluded that the most effective design parameters on the displacement ductility values of the walls are the vertical reinforcement ratio and axial load, followed by the aspect ratio, the thickness-to-length ratio, and flanged/boundary elements area to gross

cross-sectional area. While the least effective parameter is the concrete compressive strength.

The comparative analysis performed between *RC* and *RM* shear walls showed that well-detailed *RM* walls achieved higher ultimate curvatures and higher displacement ductility values when compared to their *RC* counterparts. This is due to the weak mortar joints in *RM* walls where cracks are initiated, resulting in the distribution of plastic strains over several courses and opening up the diagonal shear cracks at the joint locations which contributed to higher ultimate displacements. Conversely, the plastic strains of *RC* shear walls were concentrated at the locations of the primary cracks, resulting in rapid strength degradation and low seismic performance when compared to *RM* shear walls. The economic assessment concluded that *RM* shear walls require lower rebar weights to achieve the same strength as *RC* shear walls. In addition, the total construction costs favored *RM* shear walls when compared to *RC* shear walls. This can be attributed to the more stringent design requirement (e.g., reinforcement spacing, number of reinforcement layers) of CSA A23.3-19 when compared to CSA S304.1-19 for ductile *RC* and *RM* shear walls, respectively.

6.3 Recommendations for Future Research

The research presented in this dissertation comprised experimental, analytical, and data-driven investigation and seismic performance quantifications of *RC* shear walls with different end configurations; however, several items still require further research efforts.

The following points present possible extensions to the research to better expand the knowledge on the seismic performance of shear walls:

1. This dissertation studied *RC* shear walls reinforced with vertical reinforcement ratios ranging from *0.66%-2.80%.* It is recommended to perform further experimental research that includes *RC* shear walls with different vertical reinforcement ratios (i.e., lower and higher ratios than those used in this dissertation).
2. Since the experimental program in this dissertation utilized fully-reversed cyclic loading, future dynamic (e.g., shake table) tests would be beneficial by running major earthquake records on similar *RC* shear walls followed by a comparative analysis between the cyclic and shake-table loading protocols.
3. In this dissertation, individual *RC* walls were evaluated, but testing *RC* buildings and presenting a comparative analysis of the seismic performance of such components and systems are still needed.
4. In this dissertation, the data-driven expressions predict the displacement ductility of *RC* shear walls using minimum and maximum values for the various design parameters. Proposing data-driven expressions outside such values for *RC* walls is needed.
5. This dissertation compared the seismic performance of ductile *RC* and *RM* shear walls. This comparative analysis does not exist in the literature. Future studies can extend the work presented herein by comparing the seismic performance of moderately ductile *RC* and *RM* shear walls.